

OBSERVATIONS OF HIGH ENERGY EMISSION FROM PULSAR WIND
NEBULAE USING VERITAS

A Dissertation

Submitted to the Faculty

of

Purdue University

by

John P. Millis

In Partial Fulfillment of the

Requirements for the Degree

of

Doctor of Philosophy

August 2008

Purdue University

West Lafayette, Indiana

To my wife Melissa, and my parents Flip and Karen

ACKNOWLEDGMENTS

The completion of this dissertation would not have been possible without the love, support and encouragement of many people in my life. I would first like to thank the members of my dissertation committee, Professors Thomas Clark, Wei Cui, and Matthew Lister for helping guide me through this whole process. And of course, I owe a great debt of gratitude to my advisor Professor John Finley, whose tireless efforts in guiding me to this point have gone well beyond the call of duty. Because of his efforts, I feel that I have produced stronger work than I thought I was capable of. Additionally, I will be eternally grateful to the other physics faculty, particularly Professors Nicholas Giordano, Andrew Hirsch and Ephraim Fischbach for their advice and guidance over the years. My experience at Purdue has been much richer because of them.

My work at Purdue has been possible only due to the efforts and support of other researchers, particularly Dr. Alexander Konopelko, Dr. Glenn Sembroski, Ben Zitzer, Filip Pizlo and Daniel Gall among others. I will also be forever grateful for the friendship extended by Daniel Gall, Josh Shive, Mike Skoby, Thomas Dautermann and Deepak Pandey. Over the years, when the work felt overwhelming, their support carried me through in ways only fellow graduate students can provide. I will remember you guys always.

I have also been blessed with an incredibly supportive family. My parents, Flip and Karen, have encouraged me since I was young to pursue my dreams. They gave me the foundation and vision I needed to realize my potential. And they never stopped believing in this day, even when I felt that it was light-years away. And, even though they have only been in my life for the last 6 years, my wife's family has loved and supported me as part of their family. They have been here through it all to help me realize this dream.

And finally, I want to thank my wife Melissa. She has been my love and support through all the tough times, the great times, the victories and defeats. Her constant belief in me at times outweighed my own, and her wisdom and love has given me the strength to face anything. I thank God for her everyday, because without her none of this would have been possible.

TABLE OF CONTENTS

	Page
LIST OF TABLES	ix
LIST OF FIGURES	x
ABSTRACT	xv
1 Introduction	1
1.1 Sources of High Energy Gamma Rays	4
1.1.1 Galactic Sources	4
1.1.2 Extragalactic Sources	7
1.2 Mechanisms for Very High Energy Emission	9
1.2.1 Synchrotron Radiation	9
1.2.2 Inverse Compton Scattering and the Synchrotron Self Compton Process	10
1.2.3 Curvature Radiation	11
1.2.4 Bremsstrahlung Radiation	12
1.2.5 Photon Production Through Pion Decay	12
1.3 Outline of This Work	12
2 Pulsars and Pulsar Wind Nebulae	14
2.1 The Formation of Pulsars	14
2.2 Types of Pulsars	16
2.3 Basic Structure and Properties of Pulsars	16
2.3.1 General Parameters	16
2.3.2 Properties of Pulsars	20
2.3.3 The Electrodynamics of Neutron Stars	21
2.3.4 The Pulsar Death Line	26
2.4 Models of High Energy Emission	27

	Page
2.4.1 Pulsar Emission Models	27
2.5 Pulsar Wind Nebulae	33
2.5.1 PWNe: Standard Theoretical Model	34
2.5.2 PWNe Emission Mechanism and Spectra	36
2.5.3 Comparison of Theoretical Models with Observations	38
3 Observing High Energy Gamma Rays	40
3.1 Cherenkov Emission and High Energy Air Showers	40
3.1.1 Air Showers Resulting from Gamma Ray Interactions	41
3.1.2 The Cosmic Ray Background	42
3.2 VERITAS	43
3.2.1 Technical Specifications	43
3.2.2 Instrument Calibration	47
3.2.3 Array Performance	47
3.2.4 Data Taking Modes	50
4 Data Analysis Techniques	51
4.1 Image Parameterization	51
4.1.1 Shower and Core Reconstruction	53
4.1.2 Scaled Cuts: Utilizing the Stereo Abilities of VERITAS	55
4.2 Standard Analysis Cuts	58
4.3 The VERITAS Standard Analysis Package	58
4.4 Likelihood of Detection	61
4.5 Ring Background Model	64
4.5.1 Source Exclusion Region	65
4.5.2 Source Test Position	66
4.5.3 The Angular Cut	67
4.5.4 The Background Ring	67
4.5.5 The ψ - Parameter	67
4.5.6 Size Cut	68

	Page
4.5.7 Telescope Multiplicity Cut	68
4.6 Extended Source Analysis	69
4.7 Pulsar Analysis	69
5 Results and Discussion	71
5.1 Determination of a PWN Target List	71
5.2 The Crab Nebula and Pulsar	72
5.2.1 The Crab Nebula Data Set	74
5.2.2 Point-Source Analysis of the Crab Nebula	76
5.2.3 Extended Source Analysis of the Crab Nebula	77
5.2.4 Energy Spectrum of the Crab Nebula	78
5.3 The Boomerang Nebula G106.6+2.9 and Pulsar PSR J2229+6114 . .	84
5.3.1 Boomerang Nebula Data	84
5.3.2 Point-Source Analysis of the Boomerang Nebula	87
5.3.3 Extended Source Analysis of the Boomerang Nebula	89
5.3.4 Discussion of the Boomerang Nebula Results	92
5.4 Pulsar Wind Nebula 3C 58	93
5.4.1 Data taken on 3C 58	93
5.4.2 Point-Source Analysis for 3C 58	96
5.4.3 Extended Source Analysis for 3C 58	99
5.4.4 Discussion of the 3C 58 Results	99
5.5 PSR J0631+1036	102
5.5.1 Data taken on PSR J0631+1036	102
5.5.2 Point-Source Analysis of PSR J0631+1036	105
5.5.3 Extended Source Analysis of PSR J0631+1036	105
5.5.4 Discussion of the PSR J0631+1036 Results	105
5.6 PSR J1930+1852	110
5.6.1 Data Taken on PSR J1930+1852	110
5.6.2 Point-Source Analysis of PSR J1930+1852	112

	Page
5.6.3 Extended Source Analysis of PSR J1930+1852	113
5.6.4 Discussion of PSR J1930+1852 Results	117
6 Conclusion	118
LIST OF REFERENCES	120
VITA	125

LIST OF TABLES

Table	Page
1.1 Comparison of Third Generation ACT Experiments	4
4.1 List of image parameters calculated in the analysis and their definitions.	54
4.2 These are the optimized cut values that have been determined to best separate the gamma ray signal from the hadronic background.	59
5.1 Short list of Northern Hemisphere pulsars, sorted by \dot{E}/d^2 . Data courtesy of ATNF [22].	72
5.2 The log of the data acquired from the fall of 2007 through February 2008 on the Crab Nebula. The VERITAS run number is listed in the first column, while the date is in the format yyymmdd. The 3rd column lists the appropriate laser run. The duration lists the canonical observation time while the livetime lists the amount of time the array was able to accept events during the run. The mode lists the offset size and direction for the Wobble observation. The Sky lists the subjective weather quality determined by the observer.	75
5.3 The log of the data acquired during the fall of 2007 on the Boomerang Nebula.	85
5.4 The log of the data acquired during the fall of 2007 on 3C 58.	94
5.5 The log of the data acquired during the fall of 2007 on PSR J0631+1036.	103
5.6 The log of the data acquired during the fall of 2007 on PSR J1930+1852.	111
6.1 Summary of the point-source analysis results for the PWN data taken by the VERITAS array since September of 2007.	119

LIST OF FIGURES

Figure	Page
1.1 Archival picture of the Whipple 10 meter reflector taken near sunset, courtesy of the VERITAS Collaboration.	2
1.2 An aerial view of the VERITAS array at its site at the Fred Lawrence Whipple Observatory. Image is an archival image courtesy of the VERITAS Collaboration.	4
1.3 VERITAS recently detected the microquasar in the system LS I 61+303. The significance map on the left (a) shows the observational results of the object while traveling in the orbital phase range where the jet of the black hole is beamed away from earth. The significance map on the right (b) shows the observational results of the object while traveling in the orbital phase range where the jet of the black hole is beamed toward earth. These are unpublished maps produced by John Millis, however the published results are available [8].	6
1.4 A sky map of the VERITAS data centered on the position of the radio galaxy M87. The y axis is the declination (Dec.) in degrees and the x axis is the Right Ascension (R.A.) in degrees. The color scale is the significance in standard deviations above the background. M87 is clearly detected at the center of the field of view. This map is an unpublished image produced by John Millis, though these data were recently published by the VERITAS collaboration [17].	8
2.1 Plot of the periods (in seconds) of known pulsars against their spin-down periods (in units of $s s^{-1}$). Also shown are the characteristic ages of the pulsars, designated by the turquoise lines, derived from the period and spin down period (see equation 2.15). These quantities can also be used to calculate the magnetic field, $B = 3.2 \times 10^{19} (P\dot{P})^{1/2}$, which are represented by the yellow lines. The pulsar death-line is designated by the black line. Occasionally, pulsars can be spun back up through accretion of material, and appear back on the lower left of the diagram. This plot was created by John Millis using data from the ATNF catalog [22].	17

Figure	Page	
2.2	Diagram, adapted from Goldreich and Julian, showing the physical boundaries and properties of a pulsar. The y-axis is the rotation axis of the pulsar, while the dipole magnetic field axis is subtended by the angle θ_0 . The magnetic field lines are seen streaming through the light cylinder, which encloses the magnetosphere. The null charge surface indicates where the charge density changes sign [26].	25
2.3	The Crab Nebula as seen by the Hubble Space Telescope (HST). The image is composed of 24 individual exposures taken with the HST's Wide Field and Planetary Camera 2 during October 1999, January 2000, and December 2000. As the wind from the central pulsar heats the surrounding gas the surrounding diffuse gas cloud radiates bluish-green. The multicolor filaments are the material from the outer layers of the star that was expelled during the explosion that continue to radiate as they cool. [43]	35
3.1	Comparison of a gamma ray shower (left), a proton shower (middle) and a proton shower containing a muon (right). Simulations courtesy of G. Sembroski.	42
3.2	The image on the left (a) 499 pixel camera from one of the VERITAS telescopes. The image on the right (b) is the camera with light concentrators placed on the PMTs. Archival images courtesy of the VERITAS Collaboration.	44
3.3	A schematic of the VERITAS trigger system which outlines the data flow through the hardware chain.	46
3.4	A plot of the VERITAS sensitivity compared to current and future experiments [54]. The x-axis is the photon energy, while the y-axis is the integral flux sensitivity. The dashed line is the crab nebula spectrum, which is used as the calibration source for ACT systems.	48
4.1	The distribution of pedestal variances during a single run.	52
4.2	The camera image of an event before (left) and after (right) the Picture/Boundary cut is made for a single telescope observation. In the image on the left the color of the pixel represents the level above the noise registered in that pixel. In the image on the right the pixels containing red meet the criteria for Picture pixels, while green pixels meet the Boundary criteria. The red ellipse is based on the moments of the image.	53

Figure	Page
4.3 The images from 4 telescopes projected on the camera focal plane (T1 – blue, T2 – green, T3 – yellow, T4 – red). The lines are the projections of the major axes of the image ellipses and the intersection, designated by the blue star, is the origin of the source on the sky. The data used for this image is from a simulation, and the simulated core position is indicated by the pink star. In this view North is down and East is to the left.	55
4.4 The impact location on the ground of the shower core is found by intersecting the lines created by the major axes of the events seen by each of the telescopes. The axes are in meters from the array center and the circles are the locations of the telescopes. In this image North is up, while East is to the right.	56
4.5 The Mean Scaled Width distribution for a 4 telescope run observing the Crab Nebula. The red histogram is for the on region, while the blue histogram is the distribution of the off region. The two black lines indicate where the standard cuts are made.	57
4.6 The Mean Scaled Length distribution for a 4 telescope run observing the Crab Nebula. The red histogram is for the on region, while the blue histogram is the distribution of the off region. The two black lines indicate where the standard cuts are made.	58
4.7 The theta square distribution for 400 minutes of Crab Nebula observations. The red curve is the on source distribution while the blue curve is the of distribution. The excess of events at the source location ($\theta \leq 0.025^\circ$) is clearly evident.	62
4.8 The distribution of significances from 20 hours of observation of the Crab Nebula (histogram). A Gaussian distribution of mean= 0 and $\sigma = 1$ normalized to the number of entries is plotted for comparison (blue curve). The Crab Nebula signal is clearly evident in the excess beyond $\sigma = 4$	63
4.9 A diagram of the Ring Background Model created by Alexander Konopelko. The various regions are described in the text.	66
5.1 This image is a composite of observations taken in radio (red), optical (green) and X-ray (blue) of the Crab Nebula. The toroidal and polar outflows are evident in the X-ray observations and the synchrotron nebula is clearly visible in the radio and optical observations [62].	74

Figure	Page
5.2 The sky map of the excess events (a) and significances (b) for the Crab Nebula data listed in Table 5.2. In both maps the ordinate is the right ascension (RA) in degrees while the abscissa is the declination (DEC) in degrees. The color scale indicates the excess in each 0.025° by 0.025° bin. The data were smoothed with a Gaussian smoothing algorithm. The white circle in (b) marks the position of a known star, Zeta Tau, that is bright enough that a significant number of pixels are turned off in the analysis. The Crab Nebula is clearly detected at the canonical source position, indicated by the intersection of the two black lines.	79
5.3 The theta squared plot of the Crab Nebula data (a). The red histogram is the on source data and the blue histogram is the off source data. A source appears as an excess above the background at values of $\theta^2 \leq 0.025 \text{ deg}^2$. The Crab nebula is clearly detected. The significance distribution for the Crab Nebula data set (b). An excess of significances is clearly observed in the upper tail of the distribution. The blue curve is a gaussian centered at zero, with a width of $\sigma = 1$, that represents the expected distribution of background events.	80
5.4 Same as Figure 5.2, except for the extended source analysis.	81
5.5 Same as Figure 5.3 except for the extended source analysis.	82
5.6 Spectrum of the Crab Nebula for energies above 500 GeV.	83
5.7 Hubble Space Telescope image of the "Boomerang" nebula, G106.6+2.9 [65]. Though there has been no obvious optical detection of the pulsar, the nebular emission is clearly visible to optical telescopes.	85
5.8 Same as Figure 5.2, except for the Boomerang Nebula.	88
5.9 Same as Figure 5.3, except for the Boomerang Nebula.	89
5.10 Same as Figure 5.7, except for the extended source analysis.	90
5.11 Same as Figure 5.8, except for the extended source analysis. There exists a slight negative excess on the left tail of the excess significances plot (b). The presence of bright stars in the field of view has been shown to cause this effect in some cases.	91
5.12 Chandra Image of the 3C 58 nebula around PSR J0205+6449. The inset image is a close-up image of the toroidal and polar outflows from the pulsar [68].	94

Figure	Page
5.13 Same as Figure 5.2, except for 3C 58. The white circle in the significance map (b), indicates the position of a bright star in the field of view. There is clearly an excess about 2.5 degrees west of the putative source location. This position is not coincident with any known sources of TeV gamma rays. Further study is warranted to establish if this feature is indeed a real source.	97
5.14 Same as Figure 5.3, except for 3C 58. There is an excess of significances on the right tail of the distribution. This excess corresponds to the feature observed in the 3C 58 sky maps (see Figure 5.12).	98
5.15 Same as Figure 5.13, except for the extended source analysis. The same extended feature is present in the sky maps that was indicated in the point source analysis.	100
5.16 Same as Figure 5.14, except for the extended source analysis. The same extended feature is present in the excess significances plot that was indicated in the point source analysis.	101
5.17 Same as Figure 5.2, except for PSR J0631+1031. The white circle in the map indicates the position of a bright star in the field of view.	106
5.18 Same as Figure 5.3, except for PSR J0631+1036. There is clearly an excess of negative significances on the left tail of the distribution in Figure 5.18(b). The sky maps in Figure 5.5.2 indicate a region of negative significance north of the putative source position. A bright star in this location is contributing to this negative excess.	107
5.19 Same as Figure 5.5.2, except for the extended source analysis.	108
5.20 Same as Figure 5.5.2, except for the extended source analysis. The same negative excess is present in Figure 5.20(b), as in the point source analysis. Again, this is likely due to the presence of a bright star in the field of view.	109
5.21 Same as Figure 5.2, except for PSR J1930+1852.	113
5.22 Same as Figure 5.3, except for PSR J1930+1852.	114
5.23 Same as Figure 5.18, except the extended source analysis.	115
5.24 Same as Figure 5.19, except the extended source analysis.	116

ABSTRACT

Millis, John P. Ph.D., Purdue University, August, 2008. Observations of High Energy Emission from Pulsar Wind Nebulae using VERITAS. Major Professor: John P. Finley.

Broadband emission has been detected from several pulsar wind nebulae (PWNe), however the physical processes that govern the dynamics and mechanisms for the emission are not well understood. Theoretical models have been developed to attempt to explain the emission seen from these objects, and they make specific predictions about the spectrum and luminosity that we can expect to see in various wavelengths. Apparently, PWNe are thought to be strong gamma ray emitters, and this is reinforced by the strong emission seen from the Crab nebula. However, observations of other PWNe in high energy gamma rays has only recently been undertaken.

VERITAS (the Very Energetic Radiation Imaging Telescope Array System) recently observed several of these sources in an attempt to detect very high energy gamma rays created in their nebulae. Results of observations of the Crab nebula, the standard source of observation for ground based gamma ray observatories and the most studied of all PWNe, are reported here as a comparison for 4 other northern hemisphere PWNe that were observed.

This work will describe the nature of these objects while outlining the work being done to describe the emission detected from various sources. The technical details of the analysis techniques employed to search for high energy gamma rays using the VERITAS array is also presented. Ultimately only the Crab Nebula was detected at high significance. However the best integral flux upper-limits above 250 GeV to date are determined for 3C 58 (1.6% Crab Nebula flux), the Boomerang Nebula (1.5%

Crab Nebula flux), PSR J0631+1036 (2.1% Crab Nebula flux) and PSR J1930+1852 (3.7 % Crab Nebula flux).

1. INTRODUCTION

Although gamma ray emitting sources have been studied for decades, mostly by space based detectors, detection of very high energy gamma rays, photons above 100 GeV, is a relatively recent accomplishment. In 1953 Galbraith and Jelley reported the results of the first air Cherenkov experiments designed to detect extended air showers from cosmic rays [1]. This was accomplished by searching for Cherenkov light, the indirect indication of cosmic rays and gamma rays interacting in the atmosphere, with a detector sensitive to Cherenkov wavelengths. Subsequently, in 1968 the Whipple collaboration employed a 10 meter reflector, Figure 1.1, focused on a single photomultiplier tube. A difficulty arose in that a single phototube is not able to discriminate gamma ray signals from the much larger cosmic ray background. In 1989, thanks to the development of a pixelated camera and a more sophisticated image parameterization method, the Whipple Collaboration utilizing its 10 meter instrument achieved the first detection of a very high energy gamma ray source – the Crab Nebula – with data accumulated over the period from 1986 - 1988 [2].

Since that first detection of the Crab nebula, the number of very high energy (VHE) gamma ray sources has increased to ≈ 60 as of spring 2008. Most of the sources for which a classification can be determined are blazars and pulsar wind nebulae. The vast majority of the detected sources of emission are unidentified sources (sources with no known counterpart at any other wavelength). The dramatic increase in the number of detections can be attributed to the development of more sensitive techniques and hardware, as well as an increased number of high sensitivity instruments in operation since 1989.

The most recent advancement in ground based gamma ray astronomy was the development of stereoscopic observations. This is a technique that utilizes multiple telescopes in an array system, which improves flux sensitivity and background dis-



Fig. 1.1. Archival picture of the Whipple 10 meter reflector taken near sunset, courtesy of the VERITAS Collaboration.

crimination. The first such stereoscopic system was the High Energy Gamma Ray Astronomy (HEGRA) experiment that was operated at Rocque de los Muchachos on La Palma. The array consisted of five 3.4 meter dishes, each with a 271 pixel hexagonal camera. Each pixel has a 0.25° angular size that gives the array a 4.75° field of view [3].

During the 1990's the stereoscopic array technique developed rapidly, leading to several new experiments being designed with steadily increasing sensitivity. Similar to the design of the Whipple 10 meter reflector, an array of four telescopes was built in the Australian outback to provide stereoscopic imaging of the gamma-ray showers by the Collaboration of Australia and Nippon for a Gamma Ray Observatory in the Outback (CANGAROO) collaboration. The observatory uses a low level array trigger to reconstruct stereoscopic events. The CANGAROO observatory is part of what is known as the third generation of Air Cherenkov Telescope (ACT) experiments. However, unlike more sophisticated triggering systems on the other third generation systems, the CANGAROO experiment uses the recorded event GPS times from the

various telescopes to match the events for reconstruction. The first telescope in the array possesses a 3° field of view camera comprised of 552 0.115° pixels, while the three subsequent telescopes have 4.2° field of view cameras with 427 0.168° pixels [4].

The Major Atmospheric Gamma Imaging Cherenkov (MAGIC) telescope, located at Rocque de los Muchachos on La Palma, consists of a single 17 meter diameter dish with a 3.8° field of view camera. Having a larger diameter dish allows for a lower energy threshold. The inner elements of the MAGIC camera consists of 397 0.1° pixels, with an outer ring of 180 0.2° pixels. A second telescope is currently under construction and should be fully operational in late 2008.

The High Energy Stereoscopic System (H.E.S.S.) is a southern hemisphere observatory located in Khomas Highland Namibia. However, unlike CANGAROO, the H.E.S.S. array is comprised of four 12 meter aperture telescopes with more sophisticated electronics, which enables them to have more accurate event reconstruction and achieve a better gamma ray sensitivity. The telescopes are arranged on the four corners of a square with sides of 120 meters. Each telescope contains 960 pixels of 0.15° diameter in a closely packed hexagonal array, providing a 5° field of view [5].

The latest of these facilities was recently completed in southern Arizona. An array of four ACTs, the Very Energetic Radiation Imaging Telescope Array System (VERITAS) array, pictured in Figure 1.2, is similar in design and concept to the H.E.S.S. experiment. Each VERITAS camera consists of 499 PMTs, each with a 0.15° field of view, giving the instrument a total field of view of 3.5° . A comparison of these four experiments is outlined in Table 1.1 below.

Using facilities such as VERITAS to study the very high energy gamma ray emissions from astrophysical objects provides insight into their nature and dynamics. Theoretical physicists construct models to explain the processes that produce the emission; and the more information that is gathered, the more these models can be constrained. But perhaps the most interesting science comes when unexpected results are documented, allowing for new areas of astrophysics to be explored.

Table 1.1
Comparison of Third Generation ACT Experiments

Characteristic	CANGAROO	MAGIC	HESS	VERITAS
Aperture (m)	10	17	12	12
# of Telescopes	4	1	4	4
# of Pixels	427	397 (180)	960	499
Pixel Size ($^{\circ}$)	0.168	0.10 (0.20)	0.15	0.15
FOV ($^{\circ}$)	4.2	3.8	5	3.5
f-number	1.1	1.03	1.25	1.0



Fig. 1.2. An aerial view of the VERITAS array at its site at the Fred Lawrence Whipple Observatory. Image is an archival image courtesy of the VERITAS Collaboration.

1.1 Sources of High Energy Gamma Rays

1.1.1 Galactic Sources

Sources of high energy gamma rays can be divided into two general categories: Galactic and extragalactic. Most of the Galactic sources that have been detected are

the result of supernovae, the explosion of high mass stars that accompanies the formation of compact objects; either neutron stars or black holes. The remnant is created when much of the progenitor star's mass is ejected into the interstellar medium (ISM) during the supernova. As the material interacts with the ISM and the interstellar magnetic field, electromagnetic radiation is generated through various processes that will be discussed in section 1.2. Neutron stars typically spin at frequencies ranging from 100's of Hz to Hz, and inject material into the interstellar medium in the form of a magnetized wind. The observed broadband emission from these rapidly rotating neutron stars is typically periodic, and it is for this reason that they are commonly referred to as pulsars (a misnomer which is short for PULSating StAR). The wind from the pulsar interacts with the interstellar medium, creating emission up through the gamma ray band. Very high energy photons result from the scattering of photons via the synchrotron self-compton process. These sources, known as pulsar wind nebulae (PWNe) have been found to have significant fluxes of high energy gamma rays [6]. These objects will be discussed in more detail in Chapter 2.

Another class of Galactic VHE gamma ray emitters are microquasars, dense stars, most likely black holes, orbiting another star, typically a massive main sequence star. The compact star accretes matter from its companion and, in the process, creates relativistic jets and toroidal outflows, leading to high energy particles emitting photons mostly via the synchrotron process. While this process generally explains the radio emission, the very high energy gamma rays are likely produced through inverse Compton scattering of thermal photons by relativistic electrons. A second interaction that may contribute to the very high energy flux is the decay of neutral pions created by the interactions of hadrons with charged ions in the neutron star/black hole wind. Detection of very high energy gamma rays from the object LS 5039 is thought to be the first detection of a microquasar [7]. A second microquasar, LS I 61+303, has been recently reported by both the VERITAS [8] (see Figure 1.3) and MAGIC [9] collaborations. The emission is characterized by a periodic flux correlated with the orbital phase. The most commonly accepted theory is that this is an indication that

the emission is beamed toward the observer only during a particular range of the compact object's motion around the center of mass of the binary system.

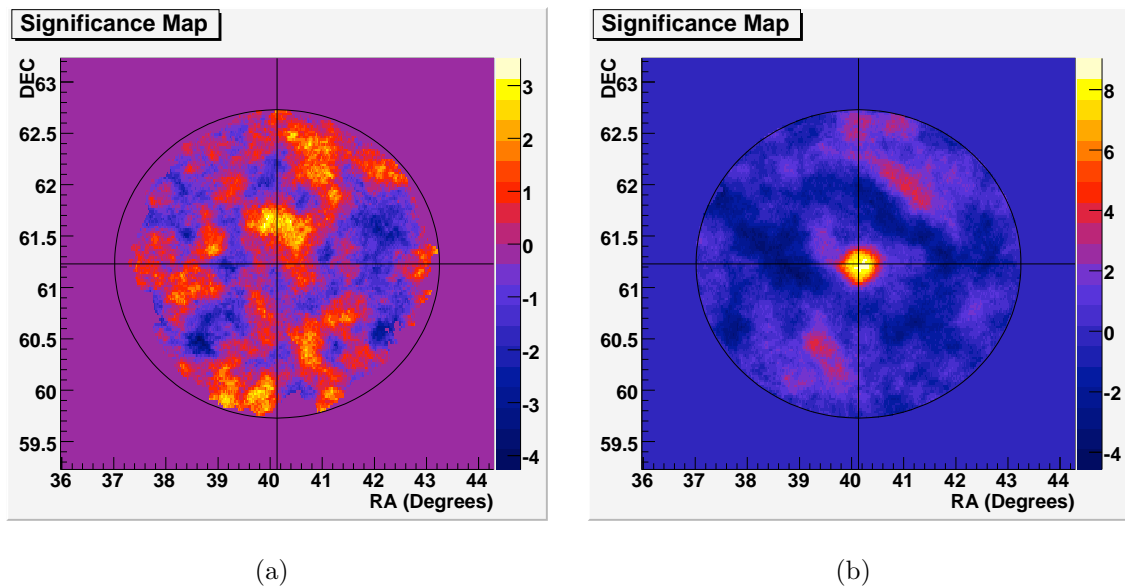


Fig. 1.3. VERITAS recently detected the microquasar in the system LS I 61+303. The significance map on the left (a) shows the observational results of the object while traveling in the orbital phase range where the jet of the black hole is beamed away from earth. The significance map on the right (b) shows the observational results of the object while traveling in the orbital phase range where the jet of the black hole is beamed toward earth. These are unpublished maps produced by John Millis, however the published results are available [8].

The center of our Galaxy, which contains a super-massive black hole believed to be associated with the object Sgr A*, is also known to be a source of high energy gamma rays [10, 11]. Detections of the Galactic Center are source confused as the experiments have an angular resolution that is insufficient to identify the exact source of the emission. Theories abound about possible physical mechanisms that would lead to gamma ray emission, from particles generating photons via curvature radiation, to exotic mechanisms such as dark matter annihilation. The continued observation of the Galactic center will constrain these theories as they predict very specific and unique spectral signatures [12].

Currently there are many detections of very high energy gamma rays that do not correspond with any known sources at other wavelengths [13]. Although follow up observations, primarily by the H.E.S.S. collaboration [13], have begun to identify the nature of these sources, many still remain. One such object, TeV 2032+4130, has been detected in VHE gamma rays but does not appear at any other wavelength [14]. Study of these sources with better spatial resolution will allow the identification of the source of the emission, and the morphology may provide some insight into the nature of the emitter.

1.1.2 Extragalactic Sources

The extragalactic VHE gamma ray source list is dominated by Blazars, which are a subclass of Active Galactic Nuclei (AGN). An AGN is a compact region at the center of a galaxy that is highly luminous across most or all of the electromagnetic spectrum. Generally, AGN are characterized by bright emission from the central region of a large elliptical galaxy, where it is theorized a super massive black hole ($M \geq 10^8 M_{\odot}$) resides, and are usually observed to have collimated particle outflows, called jets, emanating from their cores. The emission from the central region easily outshines the rest of the galaxy. This emission is believed to arise as matter in a surrounding disk is accreted onto the black hole. The emission seen in very high energy gamma rays is likely intimately linked to the base of the jets at the center of the galaxy. There are various theoretical models attempting to explain the creation of the jets, such as the magnetic fields from the black hole collimating the accreting material into a structured outflow (see [15] and references therein). Blazars are different than other AGN in that their highly beamed relativistic jets are aligned at a small angle along the observers line of sight. In 1992, the first of these objects to be detected at very high energy was Mrk 421 by the Whipple Collaboration [16]. It has been found that blazars, like all AGN, are highly variable and go into low and high states

of emission. When blazars enter a high state they can reach flux levels in the VHE an order of magnitude larger than the Crab nebula.

Radio galaxies are thought to be blazars with jets that deviate more than 20 degrees from the observer's line of sight. Since the jets are viewed off-axis, the highly relativistic beaming appears less prominent though the particles still have the potential of producing high energy gamma rays. Recently the VERITAS experiment reported a detection of one such radio galaxy, M87 [17], at high significance. Figure 1.4 shows a sky map of the VERITAS detection of this source.

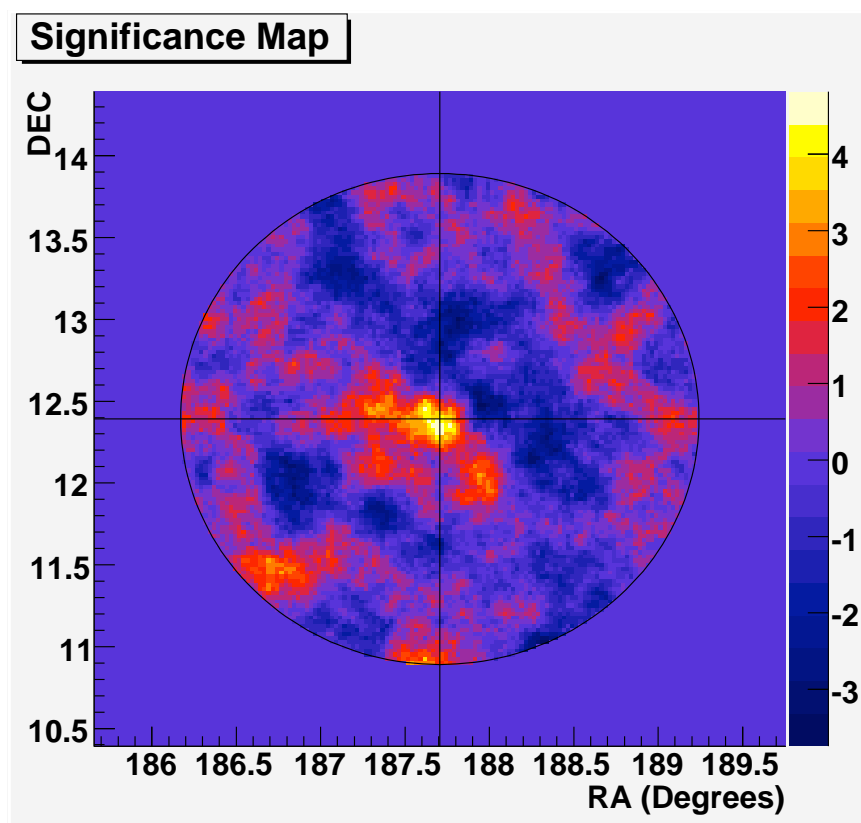


Fig. 1.4. A sky map of the VERITAS data centered on the position of the radio galaxy M87. The y axis is the declination (Dec.) in degrees and the x axis is the Right Ascension (R.A.) in degrees. The color scale is the significance in standard deviations above the background. M87 is clearly detected at the center of the field of view. This map is an unpublished image produced by John Millis, though these data were recently published by the VERITAS collaboration [17].

Although it is procedurally difficult, ground based gamma ray facilities are also involved in the study of events known as gamma ray bursts. There are many models that have been postulated to explain the emission from this class of objects, such as certain types of very energetic supernova or the coalescence of compact objects, specifically neutron stars or black holes (see [18] and references therein). These events are distinctive in that they are extremely bright in gamma rays (photons with $E \geq 200$ keV) and produce a very high flux over a short period of time. Several satellite-based experiments carry burst alert monitors to monitor the sky for these sudden bursts. However, the emission is brief and ground based gamma ray observatories have not observed the prompt component. It is usually still worthwhile to monitor the region where the burst occurred, as a distinct, but much dimmer, afterglow can possibly be detected for hours or even days after the event [19].

1.2 Mechanisms for Very High Energy Emission

Thermal radiation processes can not produce detectable levels of gamma rays, as the temperature of a blackbody radiator would need to exceed $10^{18}K$ in order to produce a reasonable flux of such emission. Rather, gamma ray photons (above $E \geq 200$ keV) are produced when charged particles interact with interstellar material or magnetic fields. These interactions are described by processes such as synchrotron radiation, inverse Compton scattering, curvature radiation, Bremsstrahlung radiation and photon production through pion decay [20].

1.2.1 Synchrotron Radiation

Charged particles (of charge q) in the presence of a magnetic field will experience a force (\mathbf{F}), and undergo circular motion via the equation

$$\mathbf{F} = q\mathbf{V} \times \mathbf{B}, \quad (1.1)$$

where \mathbf{V} is the particle velocity and \mathbf{B} is the magnetic field strength. If the particles are non-relativistic, they will radiate at the frequency of gyration and are said to emit cyclotron radiation. However, in the case of particles traveling at a significant fraction of the speed of light, they can emit at frequencies several times larger than the gyration frequency. This type of emission is known as synchrotron radiation, and is more complex than simple cyclotron radiation. In fact, the emission will have a broad spectral distribution with a characteristic frequency

$$\nu_{synchrotron} \approx 4 \times 10^{10} \gamma^2 B \sin\theta \frac{m_e}{m} \text{ Hz.} \quad (1.2)$$

Here γ is the Lorentz factor $\left(\gamma = \frac{1}{\sqrt{1 - \frac{v^2}{c^2}}}\right)$, m_e is the mass of the electron, B is the magnetic field strength, θ is the angle between the emitting particles velocity vector and the resulting direction of the synchrotron photon, and m is the mass of the emitting particle.

Given typical values of the ISM magnetic field on the order of 10^{-6} Gauss, a photon with a frequency on the order of 10^{26} Hz is needed to meet the minimum threshold for triggering a ground based ACT. Given the large Lorentz factor that would be necessary to produce photons of gamma-ray energy from electrons ($\gamma \sim 10^{11}$), it is not likely that the synchrotron process is responsible for very high energy gamma rays, except perhaps in environments where high Lorentz factors or strong magnetic fields are readily present [21].

1.2.2 Inverse Compton Scattering and the Synchrotron Self Compton Process

Inverse Compton scattering is the process by which a low energy photon is boosted to high energy. This occurs when a high energy electron transfers some of its energy and momentum to the photon. It is possible that when a population of electrons interacts with a population of photons that were the result of the synchrotron radiation process, the electrons can boost the photons to very high energies. Such a process

is known as the synchrotron self Compton (SSC) mechanism. Inverse Compton processes are far more likely to produce very high energy photons given that they arise due to relativistic energy and momentum transfer [21]. This is most readily evidenced by comparing the power produced by a particle via the synchrotron and the inverse Compton processes. If P_{IC} is the power produced by the inverse Compton process and P_{SSC} is the power produced by the SSC process, then their ratio is given by

$$\frac{P_{IC}}{P_{SSC}} = \frac{U_{rad}}{U_B} \quad (1.3)$$

where U_{rad} and U_B are the energy densities of the radiation fields and magnetic fields respectively. In typical environments around stars, the radiation energy density is likely to be several orders of magnitude greater than the magnetic field energy density.

1.2.3 Curvature Radiation

Curvature radiation is similar to synchrotron radiation in that the emission is a result of ultra-relativistic particles emitting photons due to acceleration along a curved path. However, in contrast to synchrotron emission produced as the particle circles the magnetic field lines, curvature radiation occurs as the particles stream along the trajectory of the magnetic field lines. The photon emission frequency is directly related to the curvature radius of the magnetic field

$$\nu_{curvature} = \frac{3c\gamma^3}{4\pi R_c} Hz, \quad (1.4)$$

where c is the speed of light, γ is the Lorentz factor, and R_c is the radius of curvature.

Evaluation of equation (1.4) for typical values of neutron stars would indicate that emission of gamma rays by curvature radiation is completely reasonable. However, photons created in this energy regime in powerful magnetic fields, like $B \sim 10^{12}G$ which is typical for a young neutron star, is likely to lead to attenuation as a result of interactions with the quanta of the magnetic field. For this reason it is not expected that any gamma ray flux originates near the neutron star surface, but rather at several

stellar radii where the magnetic field strength is several orders of magnitude lower, reducing the probability of photon attenuation.

1.2.4 Bremsstrahlung Radiation

Bremsstrahlung radiation is simply the process by which charged particles are decelerated by the electromagnetic field produced by surrounding ions, leading to emission of a photon with energy proportional to the energy loss of the charged particle. For this reason, charged particles with TeV energies are capable of producing very high energy gamma rays, with the flux of photons from a given region proportional to the surrounding ion density [21].

1.2.5 Photon Production Through Pion Decay

Cosmic rays are primarily composed of Hydrogen nuclei, i.e. protons, though a small percentage is made up of heavier nuclei. The proton component of the cosmic rays can lead to pion production through inelastic collisions with other protons and nuclei ($p + p \rightarrow p + p + \pi^0$), as well as pion photo-production ($p + \gamma \rightarrow p + \pi^0$). The neutral pions then quickly decay into two photons. These photons can achieve gamma ray energies when the pion is produced through the photo-production mechanism. In contrast, the steep cosmic ray spectrum and proton-proton cross section in the ISM can be prohibitive in producing more than a negligible gamma ray flux through inelastic collisions.

1.3 Outline of This Work

The subject of this dissertation is the search for gamma ray emission from pulsar wind nebulae and the pulsars that power them. The nature of pulsar wind nebulae, their structure and emission mechanisms is not well understood. Efforts to model these objects lead to specific predictions about emission at high energies. VERI-

TAS recently undertook the task of surveying northern hemisphere PWNe in very high energy gamma rays. Chapter 2 focuses on the characteristics of pulsars, and the theoretical models thought to govern the dynamics of these objects. Pulsars are generally believed to be the central engines that power the emission in the nebular region. As pulsars evolve they inject material into the surrounding interstellar medium creating broadband emission. A general discussion of PWNe and some of the work in the literature to model the emission from these objects is also presented in Chapter 2. The VERITAS experiment, the telescope array used to acquire the very high energy gamma ray data used in this thesis, is discussed in Chapter 3. The data analysis methodology is discussed in Chapter 4, and describes both point source and extended source analyses. Additionally, the pulsar analysis is discussed, which was a significant work done by the author for this dissertation. Chapter 5 reports on results from the Crab nebula, the Boomerang nebula associated with the pulsar PSR J2229+6114, 3C58, as well as the regions around the pulsars PSR J0631+1036 and PSR J1930+1852. Two different analyses are conducted for each source and the results are discussed and compared to previous measurements. Finally, Chapter 6 summarizes the results herein, and outlines the conclusions that can be drawn from the data.

2. PULSARS AND PULSAR WIND NEBULAE

2.1 The Formation of Pulsars

When a region of an interstellar molecular cloud becomes sufficiently dense, that region is overcome by its own gravity and collapses into a protostar, a star-like object that has not yet entered a nuclear burning phase. If a protostar is massive enough, its collapse continues until the core temperature becomes high enough that it begins to burn its nuclear fuel. Once nuclear fusion begins a star is said to be in the main sequence phase of its life. During this phase, stars, in a state of hydrostatic equilibrium, fuse hydrogen into helium in their cores, mostly through the PP I and II chains. Once the star has depleted the hydrogen in its core however, the core begins to collapse, as there is no longer a source of energy to counteract gravity, and the star enters the next phase of its life. If the star has a mass less than one solar mass, electron degeneracy pressure in the core will eventually balance the gravitational pull and the stellar core becomes a white dwarf.

Stars with masses of approximately one solar mass possess a core massive enough to sustain the nuclear fusion of heavier elements. Depending on the specific mass of the star, it will oscillate between what are known as the Red Giant and Blue Giant branches as the core fuses increasingly heavier elements. Stars in excess of three solar masses will produce what are referred to as Supernova events as the energy from fusion in the outer layer of the core pushes the stellar material into the surrounding medium.

When a star's mass exceeds \sim eight solar masses, the core can convert to a neutron star or black hole. The core continues to fuse increasingly heavier elements until the fusion of silicon leads to an iron-dominated core. At this point the energy required to fuse the iron in the core (an endothermic process) is not available and the core

contracts due to the large gravitational potential. The temperature of the core ($T \sim 10^{10}\text{K}$) creates photons of such high energy that heavier nuclei are destroyed through photodisintegration. As the density and temperature of the core increase during the continued collapse, energy from the surrounding gas is extracted to feed the photodisintegration of the remainder of the core. The removal of this energy, however, means that the pressure in the core is no longer high enough to keep the core from collapsing. At the same time the electrons, whose degeneracy pressure was also stabilizing the star, are absorbed through capture by the protons left behind by photodisintegration and the heavy nuclei that still remain.

The gravitational force is no longer balanced by the electron degeneracy pressure, and the core of the star collapses at a velocity proportional to the radius from the center of the core. When the velocity of the collapse equals the speed of sound, there is a decoupling from the inner part of the core. The inner part of the core continues to collapse until the density surpasses $8 \times 10^{14} \text{ g cm}^{-3}$, with most of the remaining electrons colliding with protons at such high kinetic energy that they undergo inverse beta decay, leaving a mostly neutron core (a process known as neutronization). The strong force causes the core to stiffen due to the Pauli exclusion principle. Once the inner core reaches this point, it rebounds slightly, sending shock waves back through the outer core that is still in freefall. The energy of the shock wave is absorbed in the falling material, producing more photodisintegration. If the mass of the core is between 1.4 and 3.0 solar masses, the shock wave, assisted by the outflow of neutrinos expelled during the neutronization of the core, will penetrate into the outer shells of the star, causing the material that was in freefall to be driven into the interstellar medium. This outflow of material is referred to as a Type II Supernova.

The inner core is eventually stabilized by the pressure of the degenerate neutron gas and becomes a neutron star. However, if the mass of the core exceeds about three solar masses, the neutron degeneracy pressure will no longer be able to balance the gravitational force and the star collapses into a black hole.

2.2 Types of Pulsars

Observational evidence suggests that some, if not most, neutron stars spin with high angular velocity, completing as many as 650 revolutions per second. These neutron stars are known as pulsars, when a beam of electromagnetic radiation is evident. There are several types of pulsars that are cataloged. The most commonly observed pulsars, and by far the most numerous, are known as radio pulsars because of their discovery in the radio band. According to The Australia Telescope National Facility's pulsar catalogue [22] there are over fifteen hundred known radio pulsars, while only about fifty are detected in the X-ray band (X-ray Pulsars) and only about seven to ten are detected in the gamma ray energy band (gamma ray pulsars). Crucial characteristics of pulsars are the spin period and the period spin down rate. Figure 2.1 shows the correlation for known pulsars of their spin period and period spin down rate.

Also of interest are pulsars at the center of an associated nebula, known as a pulsar wind nebula (PWN), the main subject of this thesis. In these systems, a young pulsar injects highly energetic electrons into the surrounding medium. These electrons lose energy due to synchrotron radiation, which is observed in the radio, X-ray, and TeV energy bands.

2.3 Basic Structure and Properties of Pulsars

2.3.1 General Parameters

As mentioned in the previous section, a pulsar is a rapidly rotating neutron star. By making some naive assumptions about the structure of neutron stars, an equation for the radius can be derived. Assuming hydrostatic equilibrium and a constant density, the gravitational force per unit volume must be balanced by the radial pressure gradient as

$$\frac{\mathbf{F}}{V} = \frac{d\mathbf{P}(r)}{dr} = -\frac{4}{3}\pi G\rho^2 r. \quad (2.1)$$

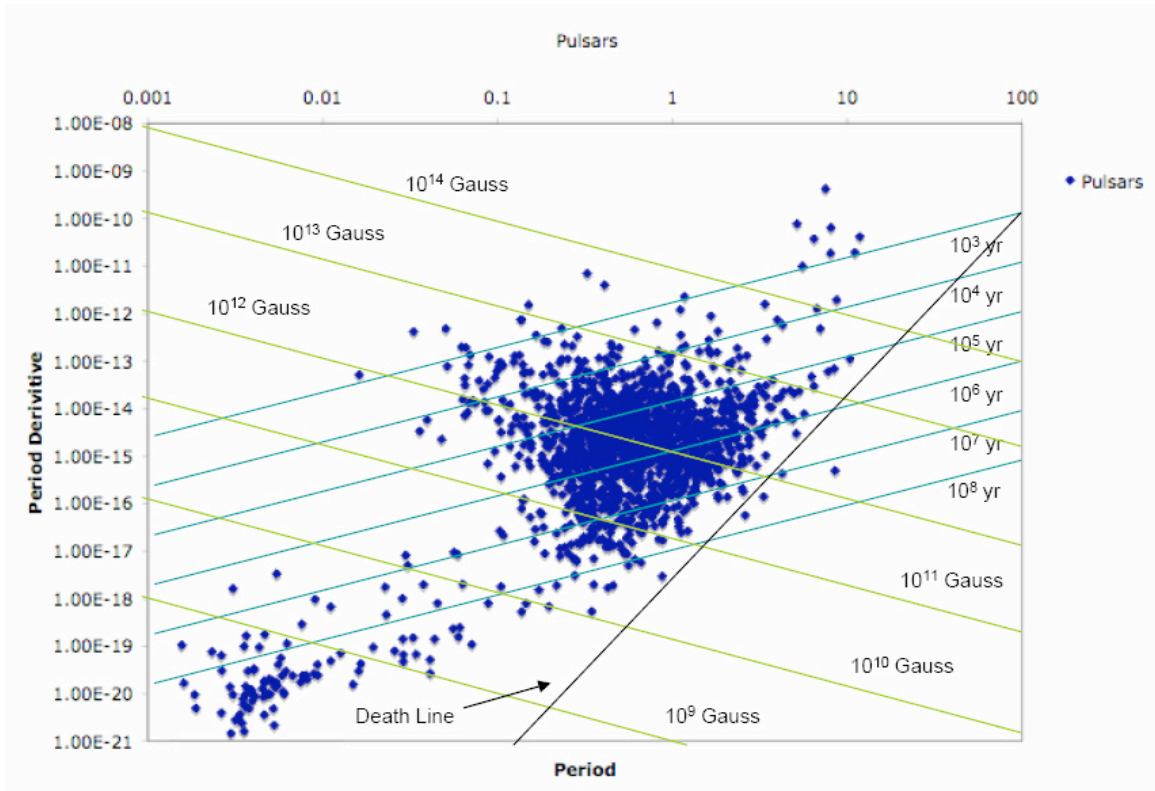


Fig. 2.1. Plot of the periods (in seconds) of known pulsars against their spin-down periods (in units of s^{-1}). Also shown are the characteristic ages of the pulsars, designated by the turquoise lines, derived from the period and spin down period (see equation 2.15). These quantities can also be used to calculate the magnetic field, $B = 3.2 \times 10^{19} (P\dot{P})^{1/2}$, which are represented by the yellow lines. The pulsar death-line is designated by the black line. Occasionally, pulsars can be spun back up through accretion of material, and appear back on the lower left of the diagram. This plot was created by John Millis using data from the ATNF catalog [22].

Where V is the volume, $\mathbf{P}(r)$ is the pressure, G is the universal gravitational constant ($6.67 \times 10^{-11} \text{ m}^3 \text{ kg}^{-1} \text{ s}^{-2}$), ρ is the density and r is the radius. So the pressure due to the gravitational force, as a function of radius, becomes

$$\mathbf{P}(r) = -\frac{4}{3}\pi G\rho^2 \int_R^r r dr = \frac{2}{3}\pi G\rho^2(R^2 - r^2). \quad (2.2)$$

Now, using the basic pressure integral where ν_p is the particle momentum density, the neutron degeneracy pressure can be obtained assuming all the neutrons have the same momentum

$$P = \frac{1}{3} \int_0^\infty \nu_p p v dp = \frac{1}{3} \nu_n p v \quad (2.3)$$

where ν_n is the number density. To obtain the particle momentum the Heisenburg uncertainty principle along with $\Delta x \approx (\frac{1}{\nu_n})^{\frac{1}{3}}$ yields

$$p \approx \Delta p \approx \frac{\hbar}{\Delta x} \approx \hbar \nu_n^{\frac{1}{3}}. \quad (2.4)$$

Here p is the momentum, $\hbar = \frac{h}{2\pi}$ is Planck's constant divided by 2π , and x is the particle's position. Assuming non-relativistic neutrons, the velocity is inversely proportional to the neutron mass m_n and represented by

$$v = \frac{\hbar \nu_n^{\frac{1}{3}}}{m_n}. \quad (2.5)$$

By combining equations (2.3), (2.4) and (2.5), the neutron degeneracy becomes

$$P = \frac{\hbar^2 \nu_n^{\frac{5}{3}}}{m_n}. \quad (2.6)$$

The particle number density is a function of the nucleon number (A), proton number (Z) and hydrogen mass m_H

$$\nu_n = \frac{N_n}{V} = \frac{(\frac{A-Z}{A})}{(\frac{m_H}{\rho})} = \left(1 - \frac{Z}{A}\right) \left(\frac{\rho}{m_H}\right) \quad (2.7)$$

so the pressure can be written

$$P = \frac{\hbar^2}{3m_n} \left[\left(1 - \frac{Z}{A}\right) \left(\frac{\rho}{m_H}\right) \right]^{\frac{5}{3}}. \quad (2.8)$$

Now setting the pressure due to gravity (2.2) equal to the neutron degeneracy pressure (2.8)

$$\frac{2}{3} \pi G \rho^2 R_{ns}^2 = \frac{\hbar^2}{3m_n} \left[\left(1 - \frac{Z}{A}\right) \left(\frac{\rho}{m_H}\right) \right]^{\frac{5}{3}} \quad (2.9)$$

and solving for the neutron star radius gives

$$R_{ns} = \frac{\hbar^2 (6\pi^2)^{\frac{1}{3}}}{G m_n M_{ns}^{\frac{1}{3}}} \left[\left(1 - \frac{Z}{A}\right) \left(\frac{\rho}{m_H}\right) \right]^{\frac{5}{3}} \quad (2.10)$$

where M_{ns} is the neutron star mass. But, since $m_H \approx m_n$ and $(1 - \frac{Z}{A}) \approx 1$,

$$R_{ns} \approx \frac{\hbar^2(6\pi^2)^{\frac{1}{3}}}{GM_{ns}^{\frac{1}{3}}} \left(\frac{1}{m_H}\right)^{\frac{8}{3}} \quad (2.11)$$

which, for a star of 1.4 solar masses (the canonical neutron star mass) yields a radius of about 44 km. Inferred radii are much closer to about 15 km [20, 23] and the difference is attributed to the simplicity of the argument above and uncertainties regarding the stellar structure [24]. Neutron stars have a density profile with an average value of $6.65 \times 10^{14} \text{ g cm}^{-3}$. This density is greater than nuclear density and the behavior of matter at these densities is unclear. Attempts have been made to model the equation of state for various possible internal structures and equations of state of neutron stars [24]. Numerical integration of the equations of state leads to a common structure for neutron stars [20, 23].

The outer crust of a neutron star, roughly 300 meters thick, is mainly heavy nuclei and relativistic degenerate electrons and may exist as a fluid of atoms or as a structural lattice [20]. The top-most layer of the crust is likely composed of iron, but the density rapidly increases beneath the surface, leading to more neutron-rich nuclei. Once the bottom of the outer crust is reached, the atoms become so neutron-rich (the density reaches about $4 \times 10^{11} \text{ g cm}^{-3}$) that the minimum energy arrangement of the atoms will find some of the neutrons sitting outside the nuclei, a phenomenon known as neutron drip. Here, the inner crust is comprised of a lattice of nuclei, like ${}_{36}^{118}Kr$, along with a super fluid of free neutrons and relativistic degenerate electrons. This structure continues downward roughly 600 meters, where the density reaches nuclear density ($2.3 \times 10^{14} \text{ g cm}^{-3}$). Beneath the crust, the composition is believed to be predominantly super fluid neutrons [24], however, there is still a small number of superfluid, superconducting protons and relativistic degenerate electrons in a layer extending roughly 9.5 km to the core of the star. The structure of the core of the neutron star has been conjectured to have a density on the order of $10^{15} \text{ g cm}^{-3}$. At this density there is no clear idea of the composition of the core, but some possibilities

include free quarks, a solid core of some other elementary particle, or a core of some other type of exotic particle such as kaons or pions [24].

2.3.2 Properties of Pulsars

The iron dominated core of a large star just before its collapse will likely have some angular momentum, even if it is very small. Conservation of angular momentum during the ensuing collapse results in the core spinning with a high angular velocity, potentially on the order of milliseconds (the upper left region of Figure 2.1). Observationally, the average period of pulsars is on the order of one second. A pulsar generally has a shorter period (higher angular velocity) at the beginning of its life and a longer period as it ages, with most of its energy dissipated due to magnetic dipole losses [25], which leads to the equation

$$\dot{E} = \frac{dE}{dt} = -\frac{16\pi^4 B^2 R^6 \sin^2 \theta}{6c^3 P^4} \text{ ergs s}^{-1} \quad (2.12)$$

where R is the neutron star radius, B is the magnetic field strength, c is the speed of light, θ is the angle between the rotation and magnetic dipole axes, and P is the spin period. Also, if the star is assumed to be a solid rotator, an equation for the rotational energy can be found in the familiar equation

$$E = \frac{1}{2} I \left(\frac{2\pi}{P} \right)^2 \text{ ergs} \quad (2.13)$$

where I is the moment of inertia. The spin down energy can be found by taking the derivative of equation (2.13), leading to

$$\dot{E} = -4\pi^2 I \frac{\dot{P}}{P^3} \text{ ergs s}^{-1} \quad (2.14)$$

where \dot{P} is the spin down period. The characteristic lifetime (τ) of the pulsar can be determined from equations (2.13) and (2.14)

$$\tau \equiv \frac{E}{\dot{E}} = \frac{P}{2\dot{P}} \text{ s.} \quad (2.15)$$

Evaluation of equation (2.15) at the typical spin down period $\dot{P} \approx 10^{-15} \text{ s s}^{-1}$ for pulsars gives a characteristic lifetime of about 10^7 years.

In the basic model, a pulsar has a strong intrinsic dipole field. The large field is accounted for by the fact that stars are observed to have at least a minimal magnetic field during the main sequence phase of their existence. During the collapse of the stellar core, conservation of flux of an ideal conductor leads to a dramatic increase in the magnetic field strength. As an example, assume the Sun is an ideal conductor. The Sun's magnetic field would increase from its nominal value of 1 G to $\approx 4.8 \times 10^{10}$ G if the radius were to collapse to the canonical 15 km value of neutron stars. This dipole is, by necessity, misaligned with the rotation axis since the magnetic field must be time dependent to allow radiation. Setting equations (2.12) and (2.14) equal to each other leads to an equation for the magnetic field strength

$$B = \left[\frac{3c^3 I}{2\pi^2 R^6 \sin^2 \theta} \right]^{1/2} (P\dot{P})^{1/2} \text{ Gauss} \quad (2.16)$$

The region around the pulsar that contains this massive magnetic field, typically on the order of 10^{12} Gauss or more [25], is known as the magnetosphere. The magnetic field lines co-rotate with the star. Consequently, as the field lines radiate from the stellar surface, the tangential velocity of the field lines increase. At the radius where the tangential velocity of the magnetic field lines reach the speed of light (see equation (2.17) below), a boundary called the light cylinder radius, R_{LC} , is reached

$$R_{LC} = \frac{cP}{2\pi}. \quad (2.17)$$

2.3.3 The Electrodynamics of Neutron Stars

In their seminal paper Peter Goldreich and William Julian described the electrodynamics of pulsars and derived the properties of pulsar magnetospheres [26]. Originally, it was thought that pulsars must be surrounded by a vacuum. To test this, the Lorentz invariant $\mathbf{E} \cdot \mathbf{B}$ above and below the surface, along with the surface charge density, is calculated.

In the co-rotating frame, the electric field must satisfy

$$\mathbf{E} = -\frac{1}{c}(\boldsymbol{\omega} \times \mathbf{r}) \times \mathbf{B}. \quad (2.18)$$

However, the external field must be found using $\mathbf{E} = -\nabla\Phi$, where Φ is the electrostatic potential. The electric field is subject to several boundary conditions. Namely there is an absence of a charge density outside the stellar surface, and both \mathbf{B}_r and \mathbf{E}_θ must be continuous at the stellar surface. The external electrostatic potential near the surface of the star can be derived beginning with the dipole moment

$$\mathbf{m} = m\hat{z} = m(\cos\theta\hat{r} - \sin\theta\hat{\theta}) \quad (2.19)$$

which yields a magnetic dipole field, B_{dip} , of

$$\mathbf{B}_{dip} = \frac{1}{r^3} [3(\mathbf{m} \cdot \hat{r})\hat{r} - \mathbf{m}] = \frac{m}{r^3} [2\cos\theta\hat{r} + \sin\theta\hat{\theta}]. \quad (2.20)$$

When the radius (r) being considered is less than the stellar radius (R)

$$\mathbf{E} = -\frac{1}{c} [\boldsymbol{\omega}(\mathbf{B} \cdot \mathbf{r}) - \mathbf{r}(\mathbf{B} \cdot \boldsymbol{\omega})]. \quad (2.21)$$

Utilizing the magnetic dipole field of equation (2.20), equation (2.21) becomes

$$\mathbf{E} = \frac{m\boldsymbol{\omega}}{cr^2} [\sin^2\theta\hat{r} - \sin 2\theta\hat{\theta}] \quad (2.22)$$

which is a function of the angular velocity $\boldsymbol{\omega}$. To find the electrostatic potential for $r > R$, Laplace's equation $\nabla^2\Phi = 0$ in spherical coordinates is used. The solution to Laplace's equation is of the form

$$\Phi(r, \theta) = \sum_l (B_l r^l + \frac{A_l}{r^{l+1}}) P_l(\cos\theta) \quad (2.23)$$

where $P_l(\cos\theta)$ is the Legendre polynomial of order l . However, since the potential must vanish as $r \rightarrow \infty$, then $B_l = 0$ for all $l > 0$. Evaluation of the equation at $l = 0$ leads to a constant which can be absorbed in the definition of the zero point of the potential. So, the electrostatic potential is given by

$$\Phi(r, \theta) = \sum_l (\frac{A_l}{r^{l+1}}) P_l(\cos\theta). \quad (2.24)$$

Applying the boundary condition that E_θ must be continuous at the surface yields

$$E_\theta = -\frac{1}{r} \frac{\partial \Phi}{\partial \theta} = \frac{A_1}{r^3} \sin \theta + \frac{3A_2}{r^4} \sin \theta \cos \theta + \dots \quad (2.25)$$

Matching equation (2.25) with the $\hat{\theta}$ component of equation (2.22) at $r = R$ gives

$$-\frac{2m\omega}{cR^2} \sin \theta \cos \theta = \frac{A_1}{R^3} \sin \theta + \frac{3A_2}{R^4} \sin \theta \cos \theta + \dots \quad (2.26)$$

Clearly $A_1 = 0$ and $A_l = 0$ for all $l > 2$, so $A_2 = -\frac{2m\omega R^2}{3c}$. In order to apply the other boundary condition, that the potential must be continuous at the surface, the potential just below the surface must be determined.

$$\Phi(r) = -\int \mathbf{E}(\mathbf{r}) \times d\mathbf{r} = -\int \left[\frac{m\omega}{cr^2} \sin^2 \theta \right] \hat{r} \times d\mathbf{r} = \frac{m\omega}{cr} \sin^2 \theta. \quad (2.27)$$

Comparing this to equation (2.24)

$$\frac{A_0}{R} - \frac{2m\omega}{3cR} \left(\frac{3}{2} \cos^2 \theta - \frac{1}{2} \right) = \frac{m\omega}{cr} \sin^2 \theta, \quad (2.28)$$

and solving for A_0 yields

$$A_0 = \frac{2m\omega}{3c}. \quad (2.29)$$

So the total potential must be,

$$\Phi(r, \theta) = \frac{2m\omega}{3c} \left[\frac{1}{r} - \frac{R^2}{r^3} P_2(\cos \theta) \right]. \quad (2.30)$$

But using the fact that $B_r = \frac{2m}{r^3} \cos \theta$ the polar magnetic field (at $\theta = 0$) is $B_0 = \frac{2m}{R^3}$. So, $2m = R^3 B_0$, which allows the potential to be written in terms of the magnetic field,

$$\Phi(r, \theta) = \frac{B_0 \omega R^3}{3c} \left[\frac{1}{r} - \frac{R^2}{r^3} P_2(\cos \theta) \right]. \quad (2.31)$$

In order to calculate the surface charge density the radial component of the electric field just above of the surface of the star must be found,

$$E_r = -\frac{\partial \Phi(r, \theta)}{\partial r} \Big|_{r=R} = \frac{B_0 \omega R}{3c} [1 - 3P_2(\cos \theta)]. \quad (2.32)$$

Taking the difference of equation (2.32) and the radial component of equation (2.22) gives,

$$\Delta E_r \Big|_{r=R} = \frac{B_0 \omega R}{3c} [1 - 3P_2(\cos \theta)] - \frac{m\omega}{cR^2} \sin^2 \theta = -\frac{2B_0 \omega R}{3c} P_2(\cos \theta). \quad (2.33)$$

So the surface charge density is found to be

$$\sigma = -\frac{2B_0\omega R}{4\pi 3c}P_2(\cos\theta). \quad (2.34)$$

Now, the Lorentz invariant $\mathbf{E} \cdot \mathbf{B}$ for both below and above the stellar surface can be calculated. For $r < R$ equations (2.22) and (2.20) provide

$$\mathbf{E} \cdot \mathbf{B} = \frac{m\omega}{cr^2}(\sin^2\theta\hat{r} - 2\sin\theta\cos\theta\hat{\theta}) \cdot \frac{m}{r^3}(2\cos\theta\hat{r} + \sin\theta\hat{\theta}) = 0. \quad (2.35)$$

The Lorentz invariant, therefore vanishes in the stellar interior. In order to calculate the invariant above the stellar surface the angular component of the electric field must be found from $E_\theta = -\frac{1}{r}\frac{\partial\Phi}{\partial\theta} = -\frac{B_0\omega R^5}{cr^4}\sin\theta\cos\theta$. So above the stellar surface the Lorentz invariant is,

$$\mathbf{E} \cdot \mathbf{B} = \frac{B_0^2\omega R^6}{cr^5}\cos\theta\left[\frac{1}{3} - \frac{R^2}{r^2}\cos^2\theta\right]. \quad (2.36)$$

The Lorentz invariant $\mathbf{E} \cdot \mathbf{B}$ must be continuous from the interior to the surface charge layer. A discontinuity at the surface, can only be reconciled by the presence of a surface electric field. This field results in an electric force that would greatly exceed the gravitational force, causing the star to become unstable. Since this is not the case, the conclusion must be made that the plasma density above the stellar surface must be non-zero and fills the magnetosphere [26]. This becomes important when discussing pulsar emission models in the next chapter, as it is thought that interactions of charged particles with the star's electromagnetic field several radii away from the stellar surface powers the broadband emission detected from these objects.

The charge density in the magnetosphere can be determined from

$$\rho = \frac{\nabla \cdot \mathbf{E}}{4\pi} = \frac{\boldsymbol{\Omega} \cdot \mathbf{B}}{2\pi c} \quad (2.37)$$

$\boldsymbol{\Omega} = \omega[\cos\theta\hat{r} - \sin\theta\hat{\theta}]$ is the angular velocity of the pulsar and the magnetic field is the dipole field from equation (2.20). This leads to the equation of the magnetosphere charge density

$$\rho = \frac{m\omega}{2\pi cr^3}[2\cos^2\theta - \sin^2\theta]. \quad (2.38)$$

Evaluation of the magnetosphere charge density equation at zero, known as the null surface, will determine the point at which the charge value changes sign. The null surface as well as the rest of the pulsar boundaries and parameters are displayed in Figure 2.2.

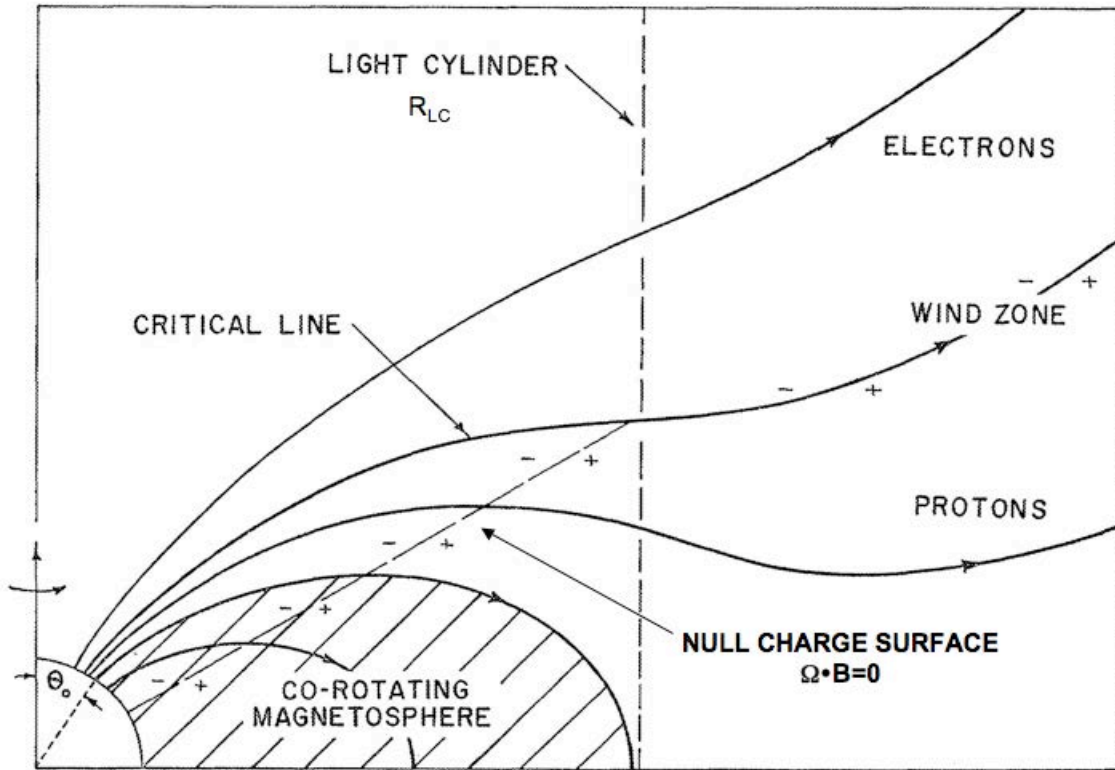


Fig. 2.2. Diagram, adapted from Goldreich and Julian, showing the physical boundaries and properties of a pulsar. The y-axis is the rotation axis of the pulsar, while the dipole magnetic field axis is subtended by the angle θ_0 . The magnetic field lines are seen streaming through the light cylinder, which encloses the magnetosphere. The null charge surface indicates where the charge density changes sign [26].

2.3.4 The Pulsar Death Line

Examination of Figure 2.1 reveals that there exists a theoretical line wherein pulsars appear to no longer radiate. Historically, this "death-line" is found by comparing the maximum work done on an electron as it is accelerated across the polar cap

$$W = \frac{2\pi e}{c} P^{-1} R_P^2 B_P \quad (2.39)$$

to the minimum energy ($E = \gamma_{ec} m_e c^2$) required to initiate pair production in the magnetic field from curvature radiation photons, where P is the pulsar spin period, e is the electron charge and R_P and B_P are the polar cap radius and magnetic field strength respectively [27]. The energy imparted to the electron by the work done by the polar cap potential can be expressed as

$$E_{ew} = \gamma_{ew} m_e c^2 \quad (2.40)$$

where γ_{ew} is the resulting Lorentz factor of the electron, and m_e is the electron mass. Comparison of equations (2.39) and (2.40) yield an equation for the Lorentz factor

$$\gamma_{ew} = \frac{2\pi e}{m_e c^3} P^{-1} R_P^2 B_P. \quad (2.41)$$

However, the polar cap radius can be expressed in terms of the period ($R_P \sim 10^2 P^{-1/2}$ meters) [28]. So equation (2.41) becomes

$$\gamma_{ew} \sim 0.24 B_P P^{-2}. \quad (2.42)$$

Now, the electron must achieve a characteristic curvature photon energy determined by

$$\epsilon_{cr} = \frac{9\hbar c}{8R_{LC}\theta_P} \gamma_{ec}^3 \quad (2.43)$$

where θ_P is the opening angle of the polar cap magnetic field and γ_{ec} is the Lorentz factor of the electron that emits curvature radiation. Using this information it is possible to make analytical approximations of the behavior of photons produced at various heights above the polar cap. Doing so leads to an equation for γ_{ec} of

$$\gamma_{ec} = 2.28 \times 10^{11} B_P^{-1/3} P^{1/3}. \quad (2.44)$$

equating of equations (2.42) and (2.44) leads to the relation

$$P^{7/2} = 1.08 \times 10^{-20} B_P^2. \quad (2.45)$$

Using the magnetic field derived in equation 2.16, $B_P = 3.2 \times 10^{19} (P\dot{P})^{1/2}$, a relation between the spin period and period derivative is found in

$$P^{5/2} = 1.11 \times 10^{19} \dot{P}. \quad (2.46)$$

This equation represents a limit for which a pulsar will no longer be able to radiate [27].

2.4 Models of High Energy Emission

2.4.1 Pulsar Emission Models

As described in the previous chapter, a pulsar will have a magnetosphere coupled to its large surface charge density. As charges stream from the surface of the star into the magnetosphere (due to the huge component of the induced vacuum electric field parallel to the magnetic field at the surface of the star), a charge density builds up in the magnetosphere [29]. Should this charge density reach the Goldreich-Julian limit, $\rho_{GJ} \approx -\omega \cdot \frac{\mathbf{B}}{2\pi c}$, the component of the electric field parallel to the magnetic field is shorted out and the magnetosphere will co-rotate with the star. Due to particle inertia, the corotation must be broken at some large distance from the star. The exact point at which it is broken is not known, however, it must happen before the light-cylinder. Beyond this point, the particle outflows and magnetic field carry away the spin-down energy of the pulsar into the surrounding environment [29].

The pulsed emission is thought to originate from inside the pulsar magnetosphere, where, in order to accelerate particles to high enough energies, a strong parallel electric field must develop. There are two possible sites inside the magnetosphere where $\mathbf{E} \cdot \mathbf{B} \neq 0$ where these fields may originate: near the magnetic poles of the inner magnetosphere or in the outer magnetosphere. These locations are the origins of the two competing emission models discussed below.

The Polar Cap Model

The polar cap model [30] depends upon the huge parallel electric field, $E_{\parallel} \equiv \vec{E} \cdot \vec{B}/B$, generated by the internal frame dragging of the rotating dipole in the open field region near the magnetic poles. Electron-positron pairs are formed above the neutron star surface by two significant processes [31]. First, these pairs are created as a result of curvature radiation along with inverse-Compton scattering of soft thermal X-rays from the surface of the neutron star off primary electrons. Second, electrons accelerated from the stellar surface radiate gamma rays that pair-produce in the strong magnetic field. These pairs screen the electric field beyond the first pair formation front (PFF). In some cases this interaction can cause some of the positrons to be accelerated back toward the stellar surface, producing another wave of gamma rays and subsequent pairs, creating a second PFF above the surface [30].

Creation of the PFFs near the surface is dominated by the inverse-Compton scattered photons, which due to their various scattering angles, screen the electric field near the surface. This process virtually excludes the possibility of electron-positron cascades escaping much beyond the surface of the neutron star [29]. However, there are regions far above the stellar surface where the electron-positron energy loss is dominated by curvature radiation, creating an up-down symmetry between the electron and positron PFFs. This curvature radiation pair front is the limiting factor of the particle acceleration voltage, and is responsible for producing the cascades needed for high energy emission [32].

Some of the curvature radiation photons will pair-produce near the stellar surface due to the strong magnetic field. These pairs are in highly excited states and will produce photons, through synchrotron radiation, of high enough energy to themselves pair produce. These combined processes have been shown to reproduce the X-ray and gamma ray spectra seen in Vela-like pulsars [30], pulsars with a spin-down age of about 10,000 years old. The emission is formed in a cone around the magnetic pole, with the opening angle determined by the polar-cap half angle at the radius of emission.

The opening angle is typically very small, unless the emission originates more than several stellar radii above the stellar surface which is unlikely given that most of the emission is thought to occur below this limit [33]. This causes a problem in that some of the most studied pulsars, like the Crab and Vela pulsars, have wide, double-peaked pulses requiring that the beam opening angles are similar to the magnetic inclination angles. So, in order for this model to accurately predict the behavior seen in these pulsars, the axes would have to be nearly aligned [29].

Recent work to account for this near alignment has revealed that the emission altitudes are not uniform across the entire cap. The curvature radiation pair front is created within a couple stellar radii of the stellar surface, except near the edges of the polar caps where the parallel electric field approaches zero. The low electric potential means that the particles will take longer to accelerate to a high enough Lorentz factor to pair produce, so the PFFs will be created at a much higher altitude. A slot gap is then formed as the PFF approaches the last open field line. The resulting high altitude cascades form a wide hollow cone of high energy emission [33]. This extension of the polar cap model allows for the inclination angles to differ by up to 20 degrees, but is still far from the 60 degree inclination angle that is inferred by the Chandra images of the Crab [29]. It is possible, however, that this same mechanism could be extended to even higher altitudes, causing even wider opening angles due to flaring field lines [33].

There is a super-exponential cut-off in the high energy gamma ray regime due to pair production attenuation. This cut-off indicates the energy at which photons can escape the magnetosphere without pair producing. At several stellar radii, where most of the radiation occurs, the photon escape energy for pair production is on the order of 10 GeV, which is where the spectral cut-off is observed to be for the pulsed emission detected by gamma ray experiments [29].

The Outer Gap Model

The outer gap model, originally proposed in 1986 by Cheng, Ho & Ruderman [34], relies on vacuum gaps, the charge depleted regions extending from the null surface, $\boldsymbol{\Omega} \cdot \mathbf{B} = 0$ (see equation (2.38)), to beyond the light cylinder in the outer magnetosphere to produce extremely relativistic electron-positron pairs. The vacuum gaps result from charges streaming along open field lines above the null charge surface out past the light cylinder. There is a lack of free charges below the null surface to replace the flux of particles escaping the region.

In these regions there is a large electric field component parallel to the magnetic field lines. Photon-photon interactions producing electron-positron pairs in these gaps provide the current in the vacuum gaps. The ensuing particle cascades, as a result of the acceleration along these field lines, are the catalyst for creating the observed high energy emission, and perhaps the pulsed emission, from these objects [34]. The specific cascade responsible for the emission, however, depends on the pulsar type. In the case of Vela type pulsars (young neutron stars with a characteristic age $\tau = \frac{P}{2\dot{P}} \approx 10,000$ years), the primary electron-positron pairs are accelerated in opposite directions. These pairs Compton scatter off the IR photons in the gap creating a primary gamma ray flux. Secondary electron-positron pair production, from inverse-Compton scattering off the IR photons, produce crossed fan beams of gamma rays and weak X-rays through synchrotron radiation. Through the interaction of these gamma ray and X-ray beams, low energy electron-positron pairs are produced which subsequently emit IR photons. This emission is responsible for the IR flux needed to sustain the cascade [35].

Similarly, in younger Crab-like pulsars (young neutron stars with a characteristic age $\tau = \frac{P}{2\dot{P}} \approx 1,000$ years), the primary gamma ray emission is produced from curvature radiation as the electron-positron pairs are accelerated along the large electric field lines through the gap. Synchrotron X-rays, created outside the gap through a similar process, interact with the primary gamma rays to produce secondary electron-

positron pairs. These secondary pairs inverse-Compton scatter off synchrotron X-rays, causing them to be boosted to gamma ray energies [35, 36].

While it seems that there is some consensus on the outer gap radiation process, there is still much debate and research being conducted on the gap geometry, which will directly effect the expected emission profile [37]. Gap geometries that are long and narrow, determined from computing the one dimensional solution to the Poisson equation perpendicular to the magnetic field lines bounded by the last open field line and null charge surface, are successful in producing double-peaked pulse profiles for pulsars with large inclination angles, like the Crab. The problem is that there is no outward emission from below the null surface, so the emission profile falls off very sharply at the outer edges, with no leading, trailing or off-pulse emission evident. This is in stark contrast to the high-energy pulsar profiles, where trailing and off-pulse emission is present [37, 38].

Alternatively, the solution to the one dimensional Poisson equation along the magnetic field lines shows that the gap is limited parallel to the field by creation of electron-positron pairs [39]. The fact that this model allows for external currents to flow through the outer gaps suggests that the emission region can extend to below the null surface. In principle, this could allow for the creation of off-pulse emission. However, it is likely that the contribution to the emission from below the null surface would be very small for pulsars like the Crab [40]. This model is not currently able to produce the double-peaked pulse profile because the emission would have to originate near the light cylinder where the structure of the magnetic field is not well understood [39, 40].

These two gap models represent the extremes of the gap geometry, and it is thought that the actual geometry may lie somewhere in between. Determination of a self-consistent gap model, that is able to produce the profiles seen in Crab and Vela-like pulsars, is the focus of work now underway on the outer gap emission model.

Model Comparison

The outer gap model uses a combination of synchrotron and curvature radiation from pairs inside and outside the gap, as well as inverse Compton scattering of the synchrotron emission by the pairs to derive the pulsar spectrum. The model relies on the creation of electron-positron pairs to produce the high-energy component of the emission profile. The pair production allows for particle acceleration to take place in the gap. Consequently, there will exist a death line in period-magnetic field space, occurring much earlier than the generally accepted radio-pulsar death line (see section 2.3.4), where high energy emission is not possible [29]. Observations suggest that older Vela-like pulsars are still emitting high energy photons in the region near the death line. The polar-cap model is, however, able to account for high energy photons from older, low magnetic field pulsars, though the accuracy of the predicted photon flux is not known. As a result, high-energy pulsed emission may provide the key for constraining the two emission models. Both models indicate a spectral cut-off in the pulsed emission spectra of pulsars around or above 10 GeV, though the exact value of the cut-off is a point of contention between the two models. Observations in this energy regime by the Gamma ray Large Area Space Telescope (GLAST; a new space based observatory scheduled for launch in 2008) and other experiments may provide a clearer picture of the geometry necessary to produce the observed broadband pulsar emission.

There is a commonality in the above mentioned models that both were created by formulating their acceleration mechanisms from basic electrodynamic principles. The models were then modified to predict emission profiles by current experiments. Though the resulting models have had some success, there are some obvious flaws that seem to indicate that neither model will ultimately succeed. As evidenced by the previous discussions, the geometry of the emission region is the determining factor in producing a particular emission profile. Once more data is gathered, particularly high-energy photon data, limitations will be able to be placed on possible geometries

of the emission regions. Early attempts to model geometries that can simultaneously reproduce narrow double-peaked profiles up to 10 GeV all indicate that the high-energy component of the emission originate along the last open field lines. Though the polar-cap model already takes this into account with the slot-gap aspect of the model, it is decidedly more difficult for the outer-gap model to reproduce the non-thermal off-pulse emission seen in typical pulsar gamma ray profiles [29].

2.5 Pulsar Wind Nebulae

Most ($\sim 90\%$) of a pulsar's spin-down power escapes from the magnetosphere in the form of a highly relativistic magnetized wind with Lorentz factor γ_w , while less than ten percent of the spin-down power appears as pulsed emission [29]. Charged particles escape with the wind and are eventually accelerated to extremely high energies. As the wind interacts with the surrounding medium, synchrotron radiation produces an emission spectrum from radio to gamma ray wavelengths. This emission is what characterizes the so-called pulsar wind nebula (PWN), however, it is sometimes difficult to distinguish the outer edges of the nebula emission and emission from the supernova remnant. Since the PWN is powered by the magnetized wind, the luminosity and profile are intrinsically linked to the pulsar's spin-down power and the density of the surrounding medium. As expected, there is a direct correlation between the PWN brightness and the pulsar spin-down power [41]. In fact, observational evidence suggests that PWN efficiency drops off dramatically for pulsars with spin-down power $\dot{E} \leq 10^{36}$ ergs s $^{-1}$, with only young energetic pulsars observed to have PWNe, with high spin-down power millisecond pulsars possibly being the only exception.

Initially, the medium that the wind interacts with will be the ejecta from the supernova remnant (SNR) left over from the creation of the pulsar. However, depending on the wind velocity, the PWN will likely expand past the SNR within the first sev-

eral millennia. After that, the medium of interaction will simply be the interstellar medium (ISM) [29].

2.5.1 PWNe: Standard Theoretical Model

The model of a PWN is that of a spherical bubble expanding from a central point (the pulsar), with the main emission process coming from synchrotron radiation [29]. However, there would be an expected forward shock, which is not observed in pulsars like the Crab pulsar and nebula (pictured in Figure 2.3). It may simply be the case that the shell brightness is very low. Generally, PWNe are aspherical and may contain thick torii and narrow, jet-like features. Since some pulsars are observed to have high proper velocity through the ISM, it is conceivable that a pulsar would quickly (within tens of thousands of years) overtake the SNR and could re-energize the shell as it is swept up in the magnetized wind, creating a source of high energy emission [29].

If the fraction of spin-down energy dissipated through pulsed emission is small, it is then reasonable to assume that the outflow of energy into the nebula, in the form of magnetic field energy and kinetic energy of charged particles, is approximately equal to the spin-down energy [42]. Soon after the wind escapes the magnetosphere, the electron-positron component of the wind becomes randomized. This causes the nebula to have a power-law energy distribution. There are several possibilities for the cause of this transition. Shock theory contends that flow energetics dominated by the particle component of the shock accelerates the particles [42]. However, efforts to model these shocks in the Crab nebula lead to a ratio of the magnetic to particle energy flux (σ) in the un-shocked wind to be $\sigma = 0.003$. This is the source of the so-called "sigma problem", where σ is generally required to exceed 1 in the magnetosphere in order to accelerate the particles. To reconcile this, the acceleration must be taking place somewhere outside the magnetosphere in the pulsar wind zone, were no well accepted acceleration model currently exists. These shock models require that σ just outside the shock, beyond the shock radius (r_s), be small but allow for the magnetic flux

to grow further out. In fact, throughout the bulk of the nebula it is expected that the magnetic energy density (ϵ_B) and particle energy densities (ϵ_e) will be roughly equal [29].

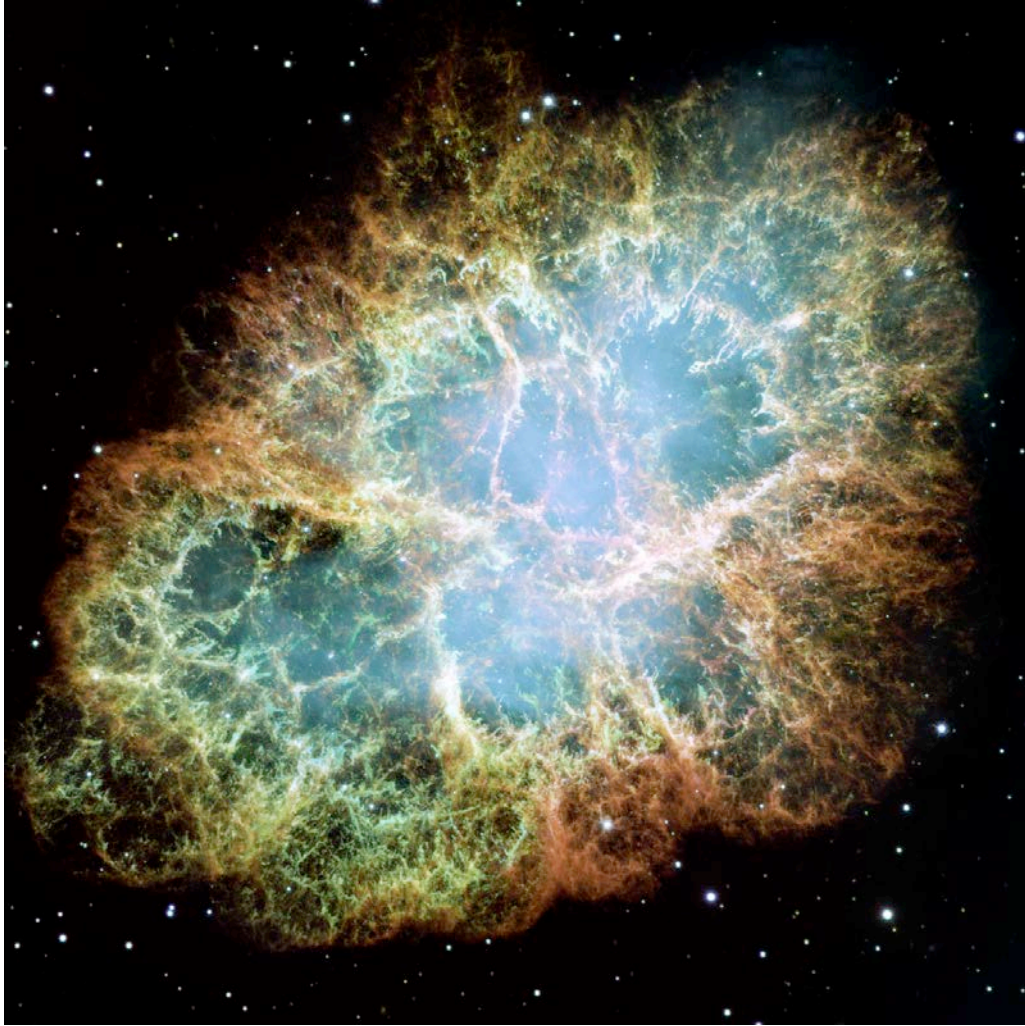


Fig. 2.3. The Crab Nebula as seen by the Hubble Space Telescope (HST). The image is composed of 24 individual exposures taken with the HST's Wide Field and Planetary Camera 2 during October 1999, January 2000, and December 2000. As the wind from the central pulsar heats the surrounding gas the surrounding diffuse gas cloud radiates bluish-green. The multicolor filaments are the material from the outer layers of the star that was expelled during the explosion that continue to radiate as they cool. [43]

2.5.2 PWNe Emission Mechanism and Spectra

As energetic particles from the magnetized wind fill the nebula, they lose energy through synchrotron radiation and as a result of the adiabatic expansion of the PWN "bubble". Observational evidence, particularly of the Crab nebula, indicates that nebular spectra are described by a power law, $N(E) \propto E^{-\Gamma}$, where the particle spectral index Γ is related to the radiation spectral index α by $\Gamma = 2\alpha + 1$ [29, 42]. Assuming a uniformly magnetized nebula populated by electrons characterized by a single spectral index (S) and a high energy cut-off E_c [29, 44], a balance is reached between the injection of charged particles from the shock front and energy losses from synchrotron radiation, leading to a relatively constant number of radiating particles. Modeling the emission from a single electron population, however, implies that there would be a steepening of the spectrum of $\Delta\alpha < 0.5$, which can not simultaneously fit both radio and X-ray observations [44].

Modeling the spectrum with more than one particle population, however, can reproduce both the radio and X-ray spectra. This is supported by the fact that most, if not all, PWNe have both equatorial and polar outflows, with the polar outflows forming collimated jets. Since the outflows have very different origins, it is expected that the particle injections may produce different spectral slopes. This arrangement, however, results in an X-ray luminosity that should be smaller than what is observed, and the observed flat radio spectrum is unexpected [44]. To account for these discrepancies, a model was developed based on the vast amount of data on the Crab, which yields a steepening of the X-ray spectrum, likely due to synchrotron cooling during the early phase of PWN evolution. However, in order to adequately replicate the spectrum, there must be constraints on the magnetic field evolution as well as a spin-down evolution that deviates from the standard pulsar model. Such constraints would eliminate the possibility that the observed radio spectrum is due to the termination shock. This led to the development of two zone models wherein the

radio emission is produced by particles accelerated in regions outside the termination shock [42, 44].

Here, only the particles accelerated near the termination shock, which are ultimately responsible for the high energy X-ray and gamma ray emission, will be discussed. Following the model outlined by Chevalier [44] of the nebula as a single emission zone provides a straight forward method for producing the features and spectrum of the nebula. Although this model does not attempt to duplicate all the observational features, it does capture the essential characteristics of the nebula. The magnetic field in the emission zone can be expressed as

$$B = \left(\frac{6\epsilon_B \dot{E}}{r_s^2 c} \right)^{1/2} \text{ Gauss} \quad (2.47)$$

where ϵ_B is the magnetic field energy density and r_s is the shock wave radius.

The number of particles which will contribute to the synchrotron power will be determined by the particle distribution function,

$$N(\gamma) = 3(\Gamma - 1)\gamma_w \gamma_m^{\Gamma-1} n \gamma^{-\Gamma} \text{ particles}, \quad (2.48)$$

where γ_w is the Lorentz factor of the pulsar wind, γ_m is the minimum particle Lorentz factor and n is the proper density in the wind just before the shock front. So, the total synchrotron power at Lorentz factor γ is

$$P(\gamma) = \frac{4}{3} \sigma_T c \gamma^2 \frac{B^2}{8\pi} \equiv \beta B^2 \gamma^2 \text{ ergs s}^{-1} \quad (2.49)$$

where σ_T is the Thompson cross section, and $\beta = 1.06 \times 10^{-15} \text{ cm}^3 \text{ s}^{-1}$ is a constant including the speed of light and scattering cross section. From the particle distribution function, the rate of injection is determined to be

$$\dot{N}(\gamma) = (\Gamma - 1)(\gamma_w m c^2)^{-1} \gamma_m^{\Gamma-1} \gamma^{-\Gamma} \dot{E} \text{ particles s}^{-1}. \quad (2.50)$$

Since the injection of particles must balance the synchrotron energy losses,

$$\dot{N}(\gamma) = \frac{1}{m c^2} \frac{\partial(N \beta B^2 \gamma^2)}{\partial \gamma} \text{ particles s}^{-1}, \quad (2.51)$$

the solution to the particle distribution function, determined by setting equations (2.50) and (2.51) equal to one another and solving the partial differential equation, becomes

$$N(\gamma) = (\gamma_w \beta B^2)^{-1} \gamma_m^{\Gamma-1} \gamma^{-(\Gamma+1)} \dot{E} \text{ particles.} \quad (2.52)$$

If the electron energy is radiated at the critical frequency, given by

$$\nu(\gamma) = \gamma^2 \frac{q_e B}{2\pi m c} \equiv z \gamma^2 B \text{ Hz,} \quad (2.53)$$

where $z = 2.80 \times 10^6$ in cgs units, the luminosity per unit frequency is

$$L_\nu = \frac{1}{2} \left(\frac{\Gamma - 2}{\Gamma - 1} \right)^{\Gamma-1} \left(\frac{6z^2 \epsilon_B}{c r_s^2} \right)^{(\Gamma-2)/4} \epsilon_e^{\Gamma-1} \gamma_w^{\Gamma-2} \dot{E}^{(\Gamma+2)/4} \nu^{-\Gamma/2} \text{ ergs s}^{-1} \text{ Hz}^{-1} \quad (2.54)$$

where ϵ_e is the electron energy density. However, using observations of the Crab and Vela nebulae to constrain the critical frequencies, the luminosity becomes

$$L_\nu = \frac{1}{2} \frac{(\Gamma - 2)^{\Gamma-1}}{(\Gamma - 1)^{\Gamma-2}} \frac{6^{(\Gamma+1)/4}}{m c^{(\Gamma+9)/4}} \beta \psi v_p^{-1} \text{ ergs s}^{-1} \text{ Hz}^{-1} \quad (2.55)$$

where

$$\psi = z^{(\Gamma-3)/2} \gamma_w^{\Gamma-2} \epsilon_e^{\Gamma-1} \epsilon_B^{(\Gamma+1)/4} r_s^{-(\Gamma-1)/2} \dot{E}^{(\Gamma+5)/4} \nu^{-(\Gamma-1)/2} \quad (2.56)$$

and v_p is the transverse pulsar velocity. The luminosity given by (2.55) is lower than that of equation (2.54) due to the smaller number of radiating electrons [44].

2.5.3 Comparison of Theoretical Models with Observations

The Crab nebula has a photon index of 2.1, corresponding to $\Gamma = 2.2$, based on X-ray observations [45]. Based on this observation, (2.54) becomes

$$L_\nu = 0.084 \epsilon_e^{1.2} \epsilon_B^{0.05} \gamma_w^{0.2} r_s^{-0.1} \dot{E}^{1.05} \nu^{-1.1} \text{ ergs s}^{-1} \text{ Hz}^{-1}. \quad (2.57)$$

The Lorentz factor of the magnetized wind (γ_w) can not be determined from observations, but $\gamma_w = 3 \times 10^6$, used by Kennel and Corontini, is a reasonable value [42]. Calculating the luminosity from (2.57) assuming $\epsilon_B = \epsilon_e = 0.5$, based on earlier

arguments, as well as the values $r_s = 3 \times 10^{37}$ cm and $\dot{E} = 5 \times 10^{38}$ ergs s^{-1} from observations of the nebula and pulsar, and using $\nu = 10^{18}$ Hz gives a value of

$$\nu L_\nu = 1.0 \times 10^{37} \text{ ergs } s^{-1}. \quad (2.58)$$

This model reasonably approximates the spectrum seen in the Crab nebula [44]. More advanced models, like those presented by Kennel and Coroniti [42, 46] and others that use Magnetohydrodynamics, improve the correlation of the observed Crab spectral distribution from the optical to gamma ray. The results not only match the synchrotron continuum, but also match the observed spatial distribution to a reasonable degree. This is something the simpler model does not even attempt.

A model proposed by Bednarek and Bartosik [47] fits the observed high energy spectra from several PWNe, including the Crab and Vela Nebulae, by first constructing the time-dependent evolution of the pulsar. Their model claims that as the pulsar evolves, the spectra of the relativistic particles injected inside the nebula varies. Then, by taking into account energy losses by different particles through various radiation processes, an equilibrium spectra of the leptons and nuclei inside the nebula can be determined.

Bednarek and Bartosik modeled the Crab Nebula photon spectrum from radio up through TeV γ -rays as synchrotron emission produced by the leptons injected into the nebula by the pulsar. These same leptons are responsible for the spectrum produced from MeV through roughly 50 TeV γ -rays, as soft photons inside the nebula inverse Compton scatter off of them. There is also an added component of γ -rays produced from the decay of pions produced from the collisions of nuclei with the matter of the nebula. Application of this model fits data from the Crab Nebula well and indicates that the gamma ray photons are created through synchrotron radiation at the lower energies, but gain an inverse Compton component in the TeV range.

3. OBSERVING HIGH ENERGY GAMMA RAYS

3.1 Cherenkov Emission and High Energy Air Showers

In order to observe photons in the energy regime above 10 GeV, the atmospheric Cherenkov imaging technique is used. As charged particles traverse a given medium, they polarize the nearby atoms. In the case of sub-luminal motion, the atoms radiate as they return to their original state. However, the polarization is symmetrical around the charged particle and the incoherent radiation has no net intensity. In the case of super-luminal motion the polarization is asymmetrical about the path of the particle. This asymmetry creates a forward intensity due to constructive interference. This light is known as Cherenkov radiation. The morphology of this emission can be derived from geometric considerations of the particle motion. The phase velocity (v_p) of light in air is expressed inversely with the index of refraction (n) by

$$v_p = c/n \quad (3.1)$$

and serves as the minimum particle velocity needed to generate Cherenkov emission. The emission angle, θ , is

$$\cos\theta = \frac{c}{nv_p}. \quad (3.2)$$

Using equation 3.2 for the minimum angle, $\theta = 0$, yields the minimum particle velocity, $v_t = c/n$, to produce Cherenkov emission. By solving the relativistic energy equation, using the minimum particle velocity, the equation for the minimum energy required to induce this process is found to be

$$E_{min} = \frac{m_0c^2}{\sqrt{1 - (\frac{v_t}{c})^2}} \quad (3.3)$$

where m_0 is the rest mass of the charged particle. Assuming a small index of refraction, like that of air ($n \sim 1.0003$ at sea level), the energy threshold lies in the GeV

range. Therefore, charged particles entering the atmosphere with these energies (or charged particles produced in the atmosphere due to high energy gamma rays) can interact with the molecular gas to create Cherenkov radiation.

3.1.1 Air Showers Resulting from Gamma Ray Interactions

The inevitable result of a gamma ray photon interacting in the atmosphere is the creation of an electron-positron pair, as this process dominates photon interactions above 20 MeV. The electron and positron follow nearly the same path as the initial photon with super-luminal speed, due to the very high energy of the primary gamma ray. The charged particles continue to produce gamma rays via Bremsstrahlung radiation, which will themselves pair-produce. This sequence continues until the charged particles and photons can no longer sustain the prescribed reactions, but rather the dominant energy loss mechanism of the charged particles is ionization of atmospheric atoms at lower energies, while the Coulomb scattering of photons becomes the dominant photon interaction.

While the cascade is occurring, the charged particles are emitting Cherenkov radiation. Since the opening angle of the pairs is small, and mostly along the direction of the primary photon, the Cherenkov emission has a locus that coincides with the initial direction of the primary photon. The Cherenkov emission opening angle, defined in equation (3.2), is going to be narrow for electromagnetic showers in the energy range detectable by ground based observatories, allowing for their detection.

Shower maximum is defined as the height above observing altitude where the greatest number of particle pairs are present. It is at this height where most of the Cherenkov light is emitted and it is a function of the energy of the primary photon. This fact will be important later when reconstructing the energy of the shower is performed in the analysis. Images from simulated particle cascades, for both gamma rays and cosmic ray showers, are shown in Figure 3.1.

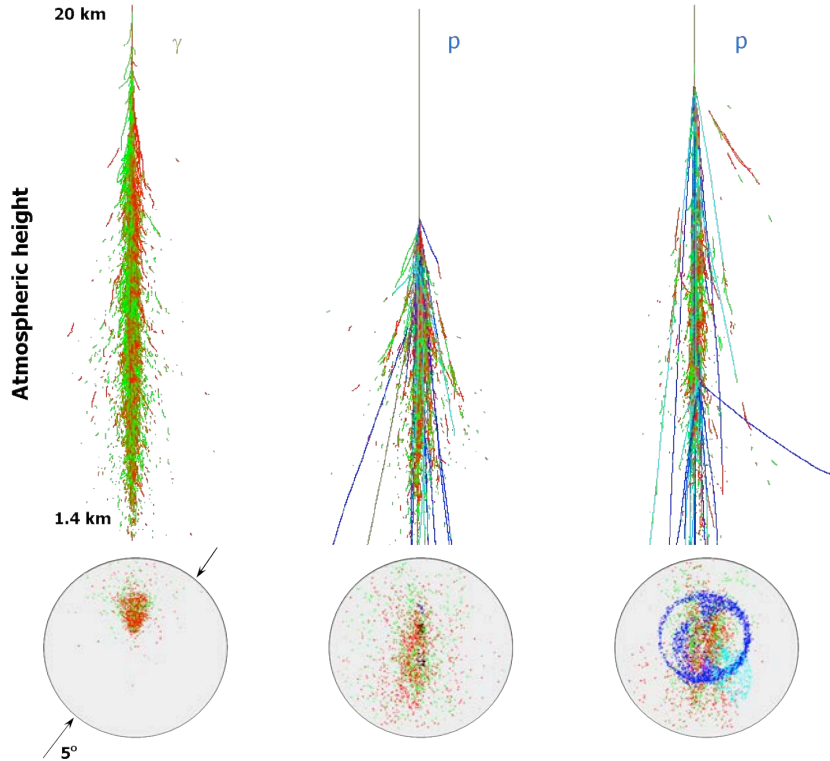


Fig. 3.1. Comparison of a gamma ray shower (left), a proton shower (middle) and a proton shower containing a muon (right). Simulations courtesy of G. Sembroski.

3.1.2 The Cosmic Ray Background

Cosmic Hadrons, the nuclei of elements, can induce air showers like those described above for photon primaries. Though, for the case of ground based observatories, proton and Helium showers are the most abundant elements of the observed background [48]. In the simplest case of a single proton, the initial interaction in the atmosphere with an atmospheric molecule, leads to the creation of either a charged or neutral pion. The nuclear core of the cosmic ray, or in this case a single proton, continues approximately along the original path of the cosmic ray. The transverse momentum that is imparted to the pion is greater than the transverse momentum that is imparted to the electron-positron pair created during gamma ray showers. As a result, the lateral spread of cosmic ray showers is much greater than that of gamma

ray showers. Additionally, the asymmetry of the cascade, due to the fact that the pion and nuclear core are of different masses, will result in the shape of the shower being less contained. This makes the cosmic rays easier to identify in the analysis (see Figure 3.1).

The neutral pion will decay into gamma rays, which will produce the familiar cascade described in the previous subsection. This will be the primary source of Cherenkov light from cosmic rays. While the charged pions will decay into neutrinos and muons. Should the muons have sufficient energy, they may reach the altitude of the observatory. It is when this occurs that an arc or a ring appears in the telescope camera. Typically, muon events only trigger a single telescope, assuming the telescopes are not too close to each other. This makes them easy to discriminate, when the telescopes are arranged in an array, by requiring that multiple telescopes observe an event. This is one of the reasons that using telescope arrays was a major advancement as it essentially eliminates the muon background at lower energies.

3.2 VERITAS

3.2.1 Technical Specifications

The VERITAS collaboration has developed an array of four atmospheric Cherenkov telescopes in southern Arizona at the Fred Lawrence Whipple Observatory (longitude 111° W, latitude 32° N, Altitude 1270 m above sea level) to observe sources of high energy gamma rays. The optical reflectors of the telescopes are dishes with a spherical figure 12 meters in diameter, and are comprised of 350 aluminized and anodized hexagonal mirrors affixed to the optical support structure. The mirrors focus onto a 499 pixel camera, Figure 3.2(a), of individual close packed 0.15° photomultiplier tubes (PMTs) creating a total instrument field of view of 3.5 degrees. Each PMT operates at a gain of 2.5×10^5 , with a quantum efficiency of roughly 25% at Cherenkov wavelengths [49].

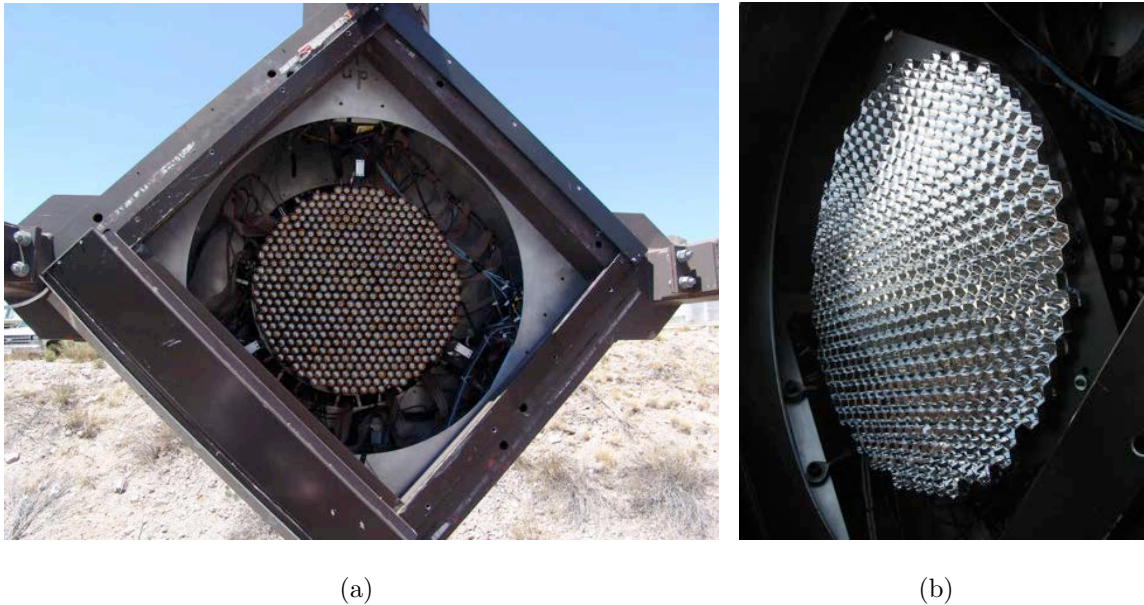


Fig. 3.2. The image on the left (a) 499 pixel camera from one of the VERITAS telescopes. The image on the right (b) is the camera with light concentrators placed on the PMTs. Archival images courtesy of the VERITAS Collaboration.

Trigger System

Because of the night sky fluctuations and cosmic ray background it is necessary to develop a system to reduce the number of false triggers, especially at the lowest energies. To this end, the VERITAS collaboration developed a three-tier trigger system (a schematic of this system is outlined in Figure 3.3) designed to eliminate triggers due to fluctuations of the Night Sky Background (NSB), as well as single muon events.

The first tier of the system, the L1 trigger, is performed at the single PMT level. The signals received by the PMTs are amplified and sent to an electronics room near the base of each telescope. Here the PMT signals are split, with the first branch sent to a Constant Fraction Discriminator (CFD) to determine if the voltage exceeds a minimum threshold to pass the L1 trigger, typically 5 photoelectrons, set by the observer [50]. The second branch is sent to a Flash Analog to Digital Converter

(FADC). The signal fed into the CFD is split into two and read into a Zero Crossing Discriminator (ZCD) to determine the zero crossing point at which time the CFD will trigger. One of the signal components is inverted and delayed, while the other component is attenuated before input into the ZCD. The ZCD then selects the time for which the signals cancel, indicating the zero crossing point. After this point is determined, and if the event passed the L1 selection criteria, an output pulse is sent to the second tier of the system, or L2 trigger, which is the Pattern Selection Trigger (PST) [50].

It is possible for the signal of a PMT to be above the minimum threshold simply due to fluctuations of the NSB, the ambient light of the night sky. In order to determine if a trigger is due to this type of fluctuation, or due to the detection of an air shower, the PMT information is sent from the CFDs to the PST which maps which PMTs fired within a 6 nanosecond coincidence window. Specifically, the PST determines if multiple, typically 3 or more, adjacent PMTs were above the L1 threshold, thereby reducing triggers due to fluctuations of the NSB which are randomly distributed across the face of the camera [50]. This is important, because it allows the telescopes to operate with a lower CFD threshold, which makes the telescopes more sensitive to low energy Cherenkov light images [51].

As mentioned in the previous chapter, at energies near the VERITAS low energy threshold the triggers will mostly consist of low energy gamma ray events and muons. In order to discriminate against the muon background, an array trigger, the third tier of the system (L3), is implemented that forces the system to only read out data if multiple (specified by the observer) telescopes contain an L2 trigger over a short temporal window, typically 50 nanoseconds [50]. When the L3 triggers, a logic signal is sent to each telescope instructing the read out of a portion of the digital buffers in the FADCs for each channel. While the FADCs are readout, the array trigger coincidence logic is inhibited by the data acquisition system via a BUSY level [52]. A consequence of this is that there exists about a 10% “dead-time” during which,

under normal operating conditions, the array is not able to trigger events. However, the benefits afforded by the array trigger outweigh this cost [50].

The array trigger is also responsible for tagging the data with information such as event number and GPS timestamp. The event information is sent to an eventbuilder program, which combines all the event information and sends it to the Harvester. The Harvester combines the event builder information from all four telescopes as well as the L3 trigger information and prepares the complete events. At the end of the run, the Harvester then prepares the run and compresses it for storage before sending it to archive. Operation of the array utilizing the L3 trigger is effective in suppressing more than 90% of local muons, and significantly suppresses triggers due to fluctuations in the NSB [50].

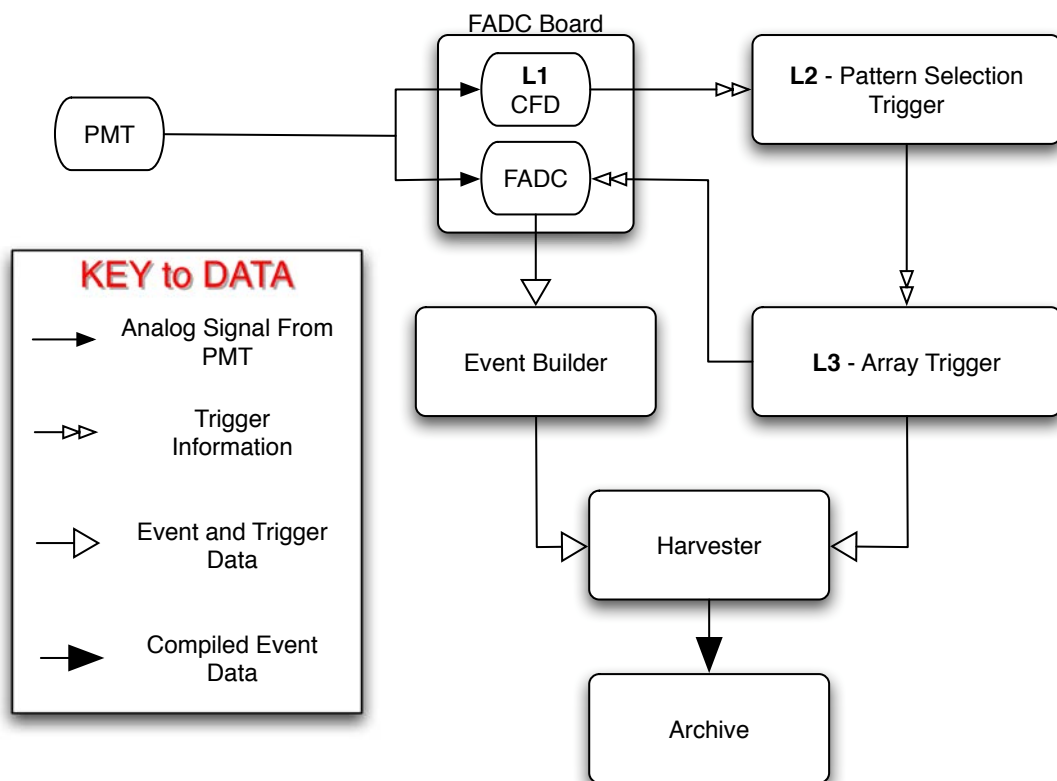


Fig. 3.3. A schematic of the VERITAS trigger system which outlines the data flow through the hardware chain.

3.2.2 Instrument Calibration

The operational parameters and overall health of the instrument varies over time, even on a nightly basis. In order to correctly interpret the information from the FADCs it is necessary to perform calibration tests during each night of observation. For purposes of flat-fielding the camera, the process by which all the PMTs are gain calibrated, a 337 nm laser is used with a 300 μJ pulse energy and 4 ns pulse length [53].

During each night of observation a five-minute, 10 Hz laser run is taken at nominal intensity. The laser run information is used to monitor the evolution of the gains, and check the integrity of the PMTs. An opal diffuser is used by the laser to spread the light uniformly across the camera face. The PMT high voltages can then be adjusted so each pixel registers the same average laser pulse size. The average pulse size is a function of the PMT quantum efficiency and the efficiency for photoelectrons to be collected along the dynode chain. Additionally, the gain in the electron multiplier stage effects the reconstructed pulse size [53]. It is also possible that the detected pulse size can be effected by the efficiency of the light concentrators that are affixed to the front the camera, see Figure 3.2(b). The purpose of these light concentrators, which are molded plastic cones with an 85% reflective evaporated aluminum coating glued onto a machined Delrin plate, is to increase the signal light collection that is normally lost due to the dead space between the PMTs. The light concentrators also limit the acceptance angle of the pixels to the solid angle subtended by the telescope, which is effective in reducing terrestrial background light [49].

3.2.3 Array Performance

The VERITAS array is designed to have maximum sensitivity to point sources in the 100 GeV - 10 TeV range (see Figure 3.4). To a lesser extent, the array is also sensitive to sources in the 50 GeV - 100 GeV and 10 TeV - 50 TeV ranges. However, significant work is done to increase sensitivity to energies below the 100 GeV threshold.

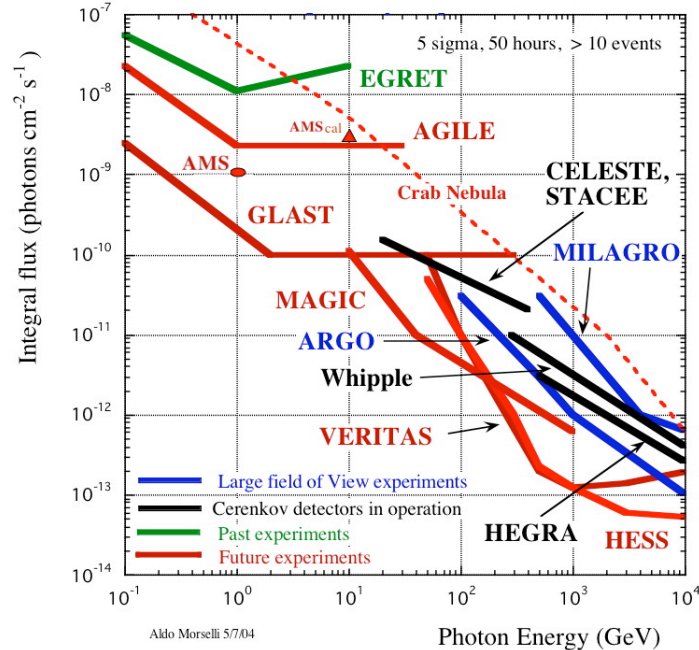


Fig. 3.4. A plot of the VERITAS sensitivity compared to current and future experiments [54]. The x-axis is the photon energy, while the y-axis is the integral flux sensitivity. The dashed line is the crab nebula spectrum, which is used as the calibration source for ACT systems.

As previously mentioned, the VERITAS field of view is 3.5 degrees, but more important than the field of view is the angular resolution of the system. The angular resolution is defined as the width of a two-dimensional Gaussian fit to the distribution of reconstructed directions for individual photons from a point source. Since VERITAS is an array, the ability to take stereo data allows for an angular resolution far superior to any single telescope system or satellite. Thus, it is possible to more accurately reconstruct the impact parameters and directional axes of the incoming photons.

An array also has a larger collection area than a single telescope. The collection area is the effective area on the ground over which the instrument is sensitive to Cherenkov emission. Since the characteristics of the air Cherenkov showers vary with energy, the collection area is also a function of the photon energy. At lower energies

there are fewer Cherenkov photons, which makes the event difficult to detect because of the low photon density in the shower.

It is important to be able to obtain the energy of the Cherenkov shower detected by the array. However, it is difficult to accurately derive this information from the event reconstruction. So attempts are made to understand how accurately the instrument is determining the shower energy. This is done by analysis of simulated events for which the energy is known. Look-up tables are created that yield values for the photon energy as a function of the event parameters. Then the energy of the real events can be approximated based on their specific parameters. The energy resolution of the instrument, how well the analysis reconstructs the actual energy of the events, can be determined by passing the analysis simulated events and seeing how well the energy is estimated. The energy resolution, $\Delta E/E$, is on the order of about 10 - 15 percent of the photon energy [51]. At lower energies the resolution degrades slightly, but improves at higher energies. The energy resolution can be improved by optimizing data cuts, the methods used to discriminate the gamma ray shows from cosmic ray background events, applied during the analysis.

Ultimately, the performance of the system is evaluated by the flux sensitivity of the array. That is, the minimum detectable flux of gamma rays that can be detected above a predetermined confidence level. In calculating the flux sensitivity, a 5 standard deviation (see section 4.4) significance above the background is required, with 50 hours of on-source observation from a source with a Crab-like spectrum of $dN/dE \propto E^{-2.5}$. Cuts are applied to eliminate background events (the methodology for analyzing the data will be presented in detail in the next chapter). The resulting sensitivity is a function of energy due to the fact that different backgrounds dominate at different energies.

3.2.4 Data Taking Modes

In the standard mode of operation, known as Wobble mode, the source is not tracked in the center of the camera, rather it is tracked at a fixed offset from the center of the field of view (typically 0.5 degrees) . It is common practice to wobble in different directions for each source (North, South, East and West) so that the on-source and off-source data would minimize systematic effects in the camera. Operation of the telescopes in this fashion allows for the simultaneous measurement of the source location as well as the background, thus allowing for efficient use of telescope time.

4. DATA ANALYSIS TECHNIQUES

In order to extract the gamma ray signal from the data, a methodical approach to discriminating against the cosmic ray background must be performed. The first step in the analysis is to take the raw camera images, what the camera registered in each PMT for each event, and determine which pixels registered a signal significantly above the level of the noise. For each pixel a statistical confidence level is determined in terms of standard deviations above the noise level, which is derived from the variance of the pedestal distribution (or pedvar), and example of which is in Figure 4.1. The analysis then suppresses pixels for which a minimum threshold, set by the user, is not reached. An initial threshold is set for the main image pixels, referred to as picture pixels. The picture threshold usually exceeds 4 or 5 standard deviations in order to insure that fluctuations in the night sky background are not contributing to the image. A second threshold, known as the boundary threshold, is set to include those pixels that are part of the image but did not surpass the picture threshold. The criteria for inclusion of these boundary pixels in the image are that they exceed a minimum threshold, usually around 2 standard deviations, but also border a picture pixel. These combined pixels will comprise the image for a particular event, while all other pixels in the event are then set to zero [55]. Figure 4.2 shows a camera image before and after picture and boundary cuts were made.

4.1 Image Parameterization

Once the image pixels have been determined, several moments of the light distribution or image parameters are determined. Two of these parameters, the length and width, define the major and minor axes of an ellipse that is fit to each image. These, and the other parameters used, are outlined in Table 4.1. It can be determined

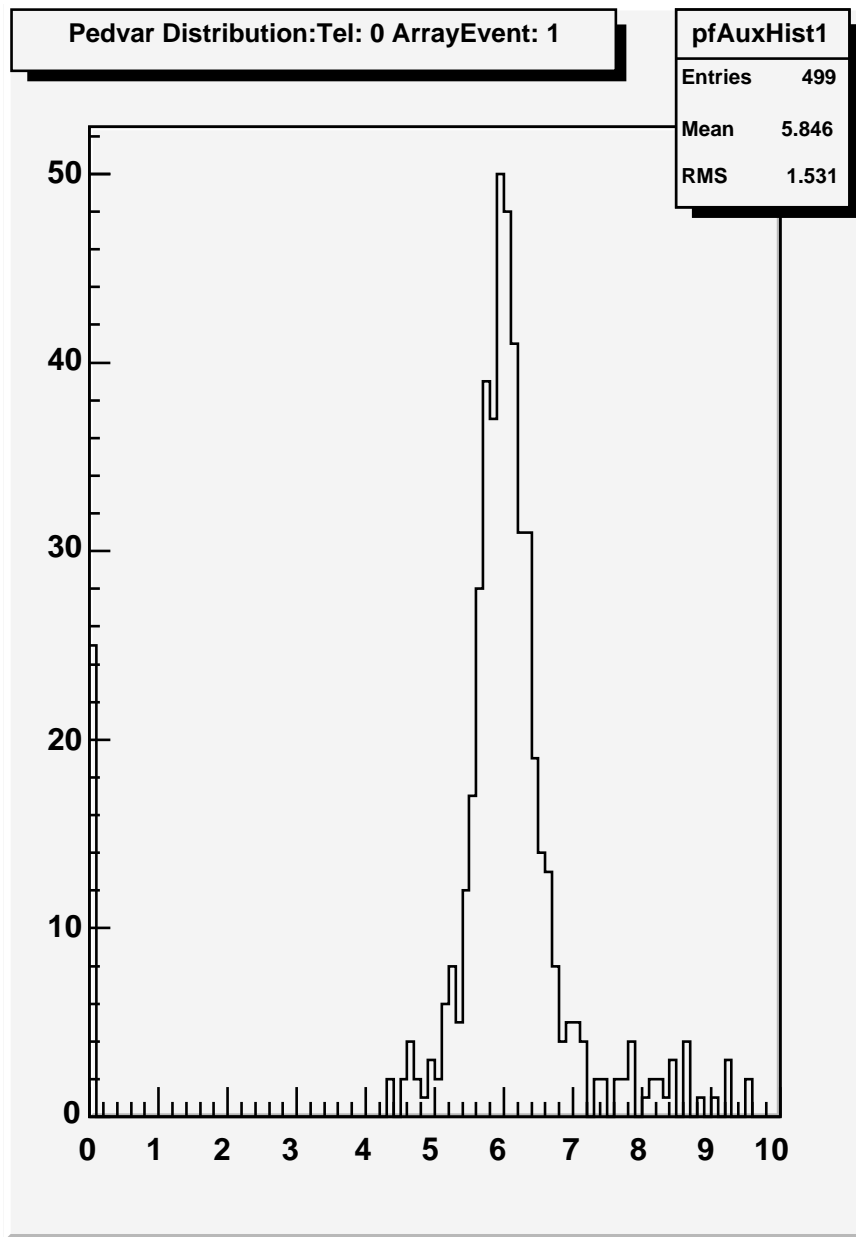


Fig. 4.1. The distribution of pedestal variances during a single run.

using data simulations what the typical values of these parameters are for gamma ray events. It is possible to obtain a clean set of data to work with by selecting events based on the image parameters outlined in Table 4.1, but new parameters, known as scaled cuts, can be developed that are more efficient when the telescopes are operated

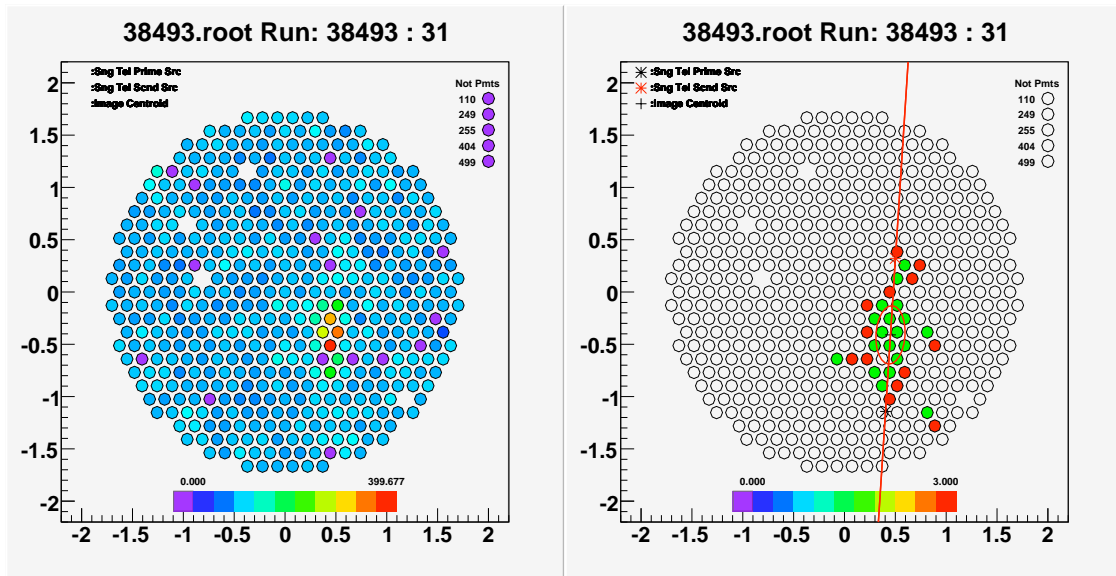


Fig. 4.2. The camera image of an event before (left) and after (right) the Picture/Boundary cut is made for a single telescope observation. In the image on the left the color of the pixel represents the level above the noise registered in that pixel. In the image on the right the pixels containing red meet the criteria for Picture pixels, while green pixels meet the Boundary criteria. The red ellipse is based on the moments of the image.

stereoscopically [55]. However, understanding these parameters requires knowledge and understanding of the electromagnetic shower reconstruction.

4.1.1 Shower and Core Reconstruction

The analysis computes a shower direction, the point in the sky where the shower (gamma ray or cosmic ray) originated, as well as the impact location on the ground. It is also possible to reconstruct the energy of the shower using simulations of gamma ray events. Having all of this information will allow for the creation of a two-dimensional sky map that indicates the origins of the putative gamma ray signal as well as compute an energy spectrum.

Table 4.1
List of image parameters calculated in the analysis and their definitions.

Image Parameter	Definition
<i>Length</i>	The RMS distribution of light along the major axis of the ellipsoid.
<i>Width</i>	The RMS distribution of light along the minor axis of the ellipsoid.
<i>Distance</i>	Distance from the center of the camera to the center of the ellipsoid.
<i>Size</i>	Sum of the digital counts in all the image pixels.
<i>Length/Size</i>	The ratio of the Length and Size parameters.
<i>Alpha</i>	The angle subtended by the axis joining the center of the camera and the image centroid and the line that lies along the ellipsoid's major axis.
<i>Asymmetry</i>	Measure of the image asymmetry.
<i>Phi</i>	Azimuthal angle of the main axis of the ellipse.

It is assumed that the source location lies along the major axis of the elliptical image. Determination of the source location can then be derived by finding the intersection of the lines determined by the major axis of each camera image superimposed onto a single camera layout (see Figure 4.3). Later in the analysis, the value θ will designate the distance from this reconstructed source location, to the canonical location of a putative source under study. Locating the shower impact position is accomplished by intersecting the lines of the primary axes produced in each telescope image location. In the case of two telescope events, a separation angle is calculated between the major axes of the images. The separation angle can also be used as a good discriminator between the gamma ray and hadron signals. Figure 4.4 is a screen shot of a program called VADisplay, which has the ability to look at images and show the reconstructed core location of the shower on the ground.

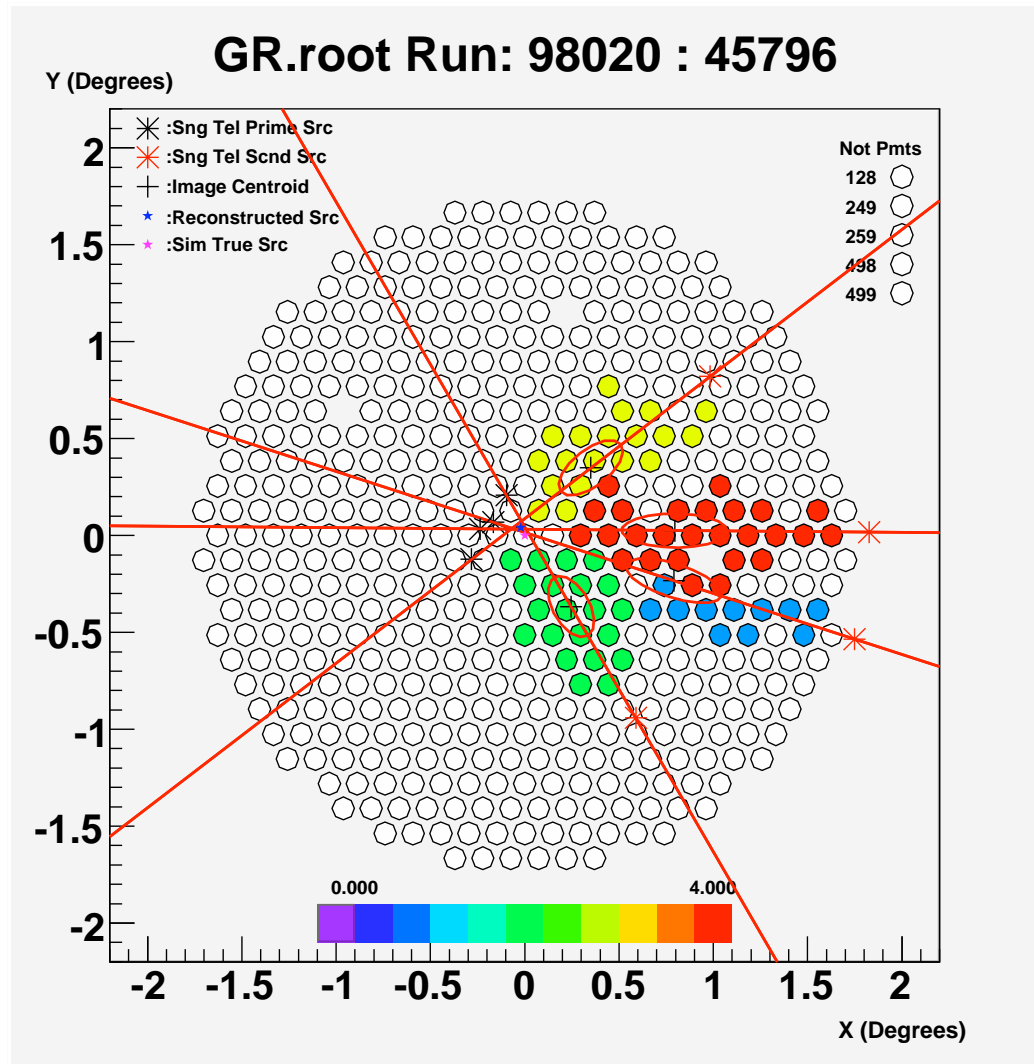


Fig. 4.3. The images from 4 telescopes projected on the camera focal plane (T1 – blue, T2 – green, T3 – yellow, T4 – red). The lines are the projections of the major axes of the image ellipses and the intersection, designated by the blue star, is the origin of the source on the sky. The data used for this image is from a simulation, and the simulated core position is indicated by the pink star. In this view North is down and East is to the left.

4.1.2 Scaled Cuts: Utilizing the Stereo Abilities of VERITAS

The brightness of shower images, which is measured as the image size, are directly dependent on the energy of the shower and the impact distance from the telescope(s).

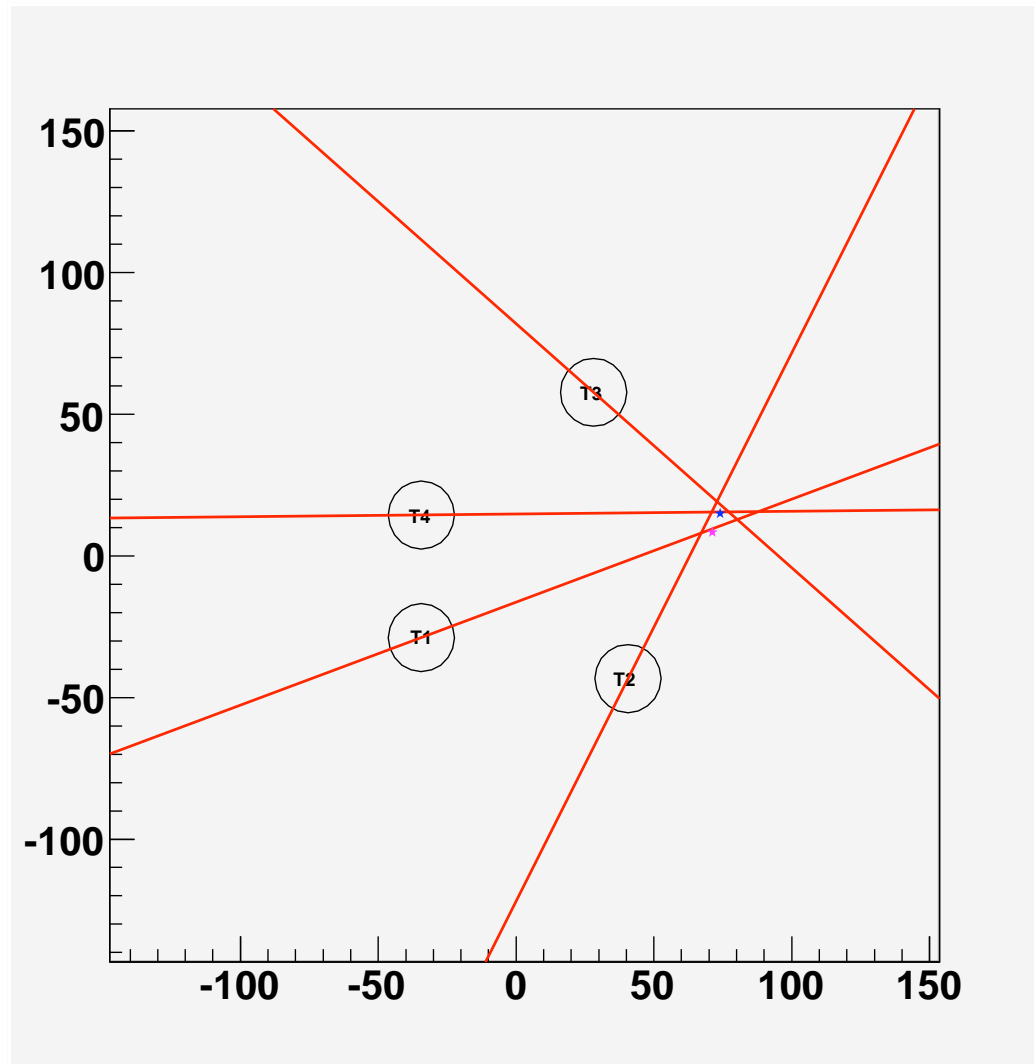


Fig. 4.4. The impact location on the ground of the shower core is found by intersecting the lines created by the major axes of the events seen by each of the telescopes. The axes are in meters from the array center and the circles are the locations of the telescopes. In this image North is up, while East is to the right.

Using Monte-Carlo simulations, it is possible to determine the expected parameters, specifically width and length, for a shower of a given size and impact distance. Scaled-width values can then be calculated for each image by taking the width of the particular image and dividing it by the average width for simulated images with the same size and impact distance. The same calculation is performed for the length values of

the image. However, since multiple telescopes are being used, it makes sense to average all the scaled-widths (and scaled-lengths) weighted by the image sizes. Doing so produces the mean-scaled-width (MSW) and mean-scaled-length (MSL) parameters for each event. These values are then stored in look-up tables that can be used in the analysis of the data. A different table must be used, however, for each zenith angle [55]. The MSW and MSL distributions are pictured in Figures 4.5 and 4.6 for a 4 telescope run.

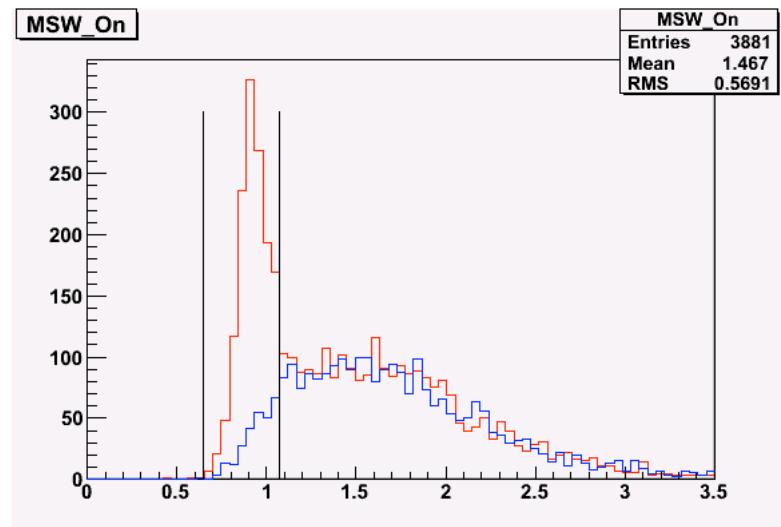


Fig. 4.5. The Mean Scaled Width distribution for a 4 telescope run observing the Crab Nebula. The red histogram is for the on region, while the blue histogram is the distribution of the off region. The two black lines indicate where the standard cuts are made.

Since VERITAS is able to reconstruct the impact location (and hence the impact distance to the showers) due to the stereoscopic trigger employed by the instrument, the MSW and MSL parameters can be used as a very powerful discrimination tool against the background.

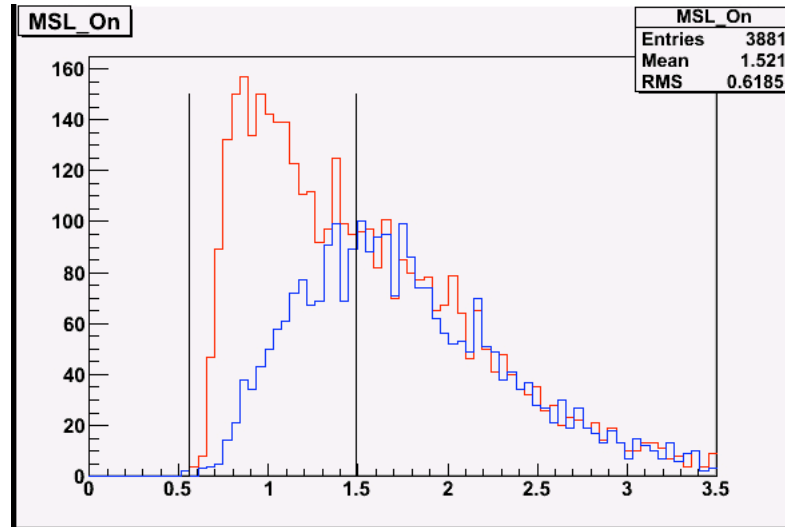


Fig. 4.6. The Mean Scaled Length distribution for a 4 telescope run observing the Crab Nebula. The red histogram is for the on region, while the blue histogram is the distribution of the off region. The two black lines indicate where the standard cuts are made.

4.2 Standard Analysis Cuts

In order to produce a clean set of data to work with, the data is cut on the parameters discussed above. The values used to eliminate the background, and hence isolate the gamma ray showers, are determined by a methodical system by which each parameter is isolated one at a time as to maximize the significance calculated for the source being used for calibration (typically the Crab). Table 4.2 shows the values that have been found to produce the greatest significance, and thus sensitivity (see section 6.4 below), for gamma ray sources.

4.3 The VERITAS Standard Analysis Package

The VERITAS collaboration has developed a standard analysis, known by the moniker VEGAS (VERITAS Gammay-ray Analysis Suite), which has six main stages. The purpose of Stage 1 is to determine the calibration constants needed to properly reconstruct the signals detected by the PMTs [56]. The signal output from the PMTs

Table 4.2

These are the optimized cut values that have been determined to best separate the gamma ray signal from the hadronic background.

Cut Parameter	Cut Value
Distance (degrees)	$0.04 \leq D \leq 1.53$
Size (d.c.)	≥ 410
Ntubes	≥ 3
Separation Angle (degrees)	≥ 16
MSW	$0.65 \leq MSW \leq 1.07$
MSL	$0.56 \leq MSL \leq 1.49$
Theta Squared (degrees ²)	≤ 0.025

are AC coupled, which does allow for the digitization of positive voltage fluctuations. In order to get around this problem a base voltage, or pedestal, of about 16 digital counts (d.c.) is injected into the FADC electronics, allowing for the resolution of both positive and negative fluctuations. However, the response of each PMT is different due to age, and other uncontrollable environmental variables. In order to quantify this response, the camera is triggered with a laser and the charge is measured in each PMT. The gain is measured in each PMT by integrating the pulse detected. This value is then compared to the average gain across the entire camera, giving a value of the relative gain that will be used to scale the output from that particular PMT. It is also necessary to determine the exact arrival time of the pulses in the PMTs which will be read out of the FADCs. However, since each of the FADCs are different, it is necessary to find the relative timing offset (T_{offset}) for each channel.

The VERITAS database, located at the University of Massachusetts, is queried by Stage 1 to retrieve information for each run such as high voltage, PMT current, telescope tracking and source data. Results of the Stage 1 analysis, including the

information retrieved from the database, are saved in a file that will then be accessed by the subsequent stages of the analysis [56].

Stage 2 of the analysis takes the calibration constants calculated in Stage 1 and combines them with the raw data, and the FADC traces are analyzed. This analysis is accomplished by subtracting the pedestal from the PMT signal, and applying gain and timing corrections. The value of the integrated charge, in addition to the integration and channel parameters are then stored in a data file [56]. Broken pixels are also identified so that they can be removed from the rest of the analysis. An interpolation between the measured telescope pointing positions is made so that the correct tracking data will be available for each event. In Stage 3 the images are cleaned using the Picture/Boundary cleaning method described earlier. Once the images have been cleaned, the moments of the images are calculated [56]. Recently, Stages 2 and 3 were combined, as doing this streamlined the analysis process, significantly reducing the analysis time.

In Stage 4 the primary image axes are used to reconstruct the shower core location on the ground and the source location on the sky. The width and length parameters are compared to Monte Carlo simulations of gamma-ray air showers, provided by the KASCADE simulation package, to calculate the mean-scaled length and mean-scaled width parameters using lookup tables. Quality cuts, such as image size and minimum number of pixels in an image, are then applied in order to remove data that can not be properly reconstructed. Those events that are properly reconstructed are then parameterized [56].

Stage 5 cuts the remaining events on the mean-scaled width and mean-scaled length parameters, as well as others that the user may choose to experiment with, to yield a clean set of data to work with [56]. This stage also has the ability to implement more sophisticated analysis methods as well as make changes to the run header information, where critical information for the analysis is stored.

Stage 6 calculates the number of events from the source location, and in the selected background regions, such that the number of excess events can be calculated.

The statistical significance of any source excess can then be calculated using the Li & Ma method (Equation 4.3 in the next section) [56]. Should a definitive detection not be made, it is possible to calculate an upper limit for the source flux [57], which will be discussed at the end of the next section.

4.4 Likelihood of Detection

Since ACT systems detect a significant amount of background in addition to the desired gamma ray signal, a statistical analysis will need to be done using the estimated background events (N_{OFF}) and the events corresponding to the source region (N_{ON}) to calculate the significance of the gamma-ray signal. A simple estimation of the number of excess events in the source region can be found

$$N_{excess} = N_{ON} - \alpha * N_{OFF}, \quad (4.1)$$

where the α parameter is a normalization factor that takes into account differences in observation time, camera acceptance and area between the signal and background regions. The excess events can be quantified graphically by plotting the theta squared distribution of the events for both the ON and OFF regions. The quantity theta is the angular distance that the reconstructed event location is from the anticipated source position. Figure 4.7 is the theta squared distribution (surface brightness plot) for 400 minutes of Crab Nebula observations. An excess of events in the ON region, indicated by the red line in the plot, is clearly observed at the reconstructed source position. Additionally, the distribution indicates that the excess of gamma-ray like events in the field of view around the nebula is consistent with a constant background rate of about 2.078 ± 0.021 events per minute during the observation.

While it may be possible to resolve a source from a simple excess calculation like equation (4.1), a proper statistical analysis is needed to determine if an observed gamma ray signal is likely due to the presence of a source, or simply a statistical

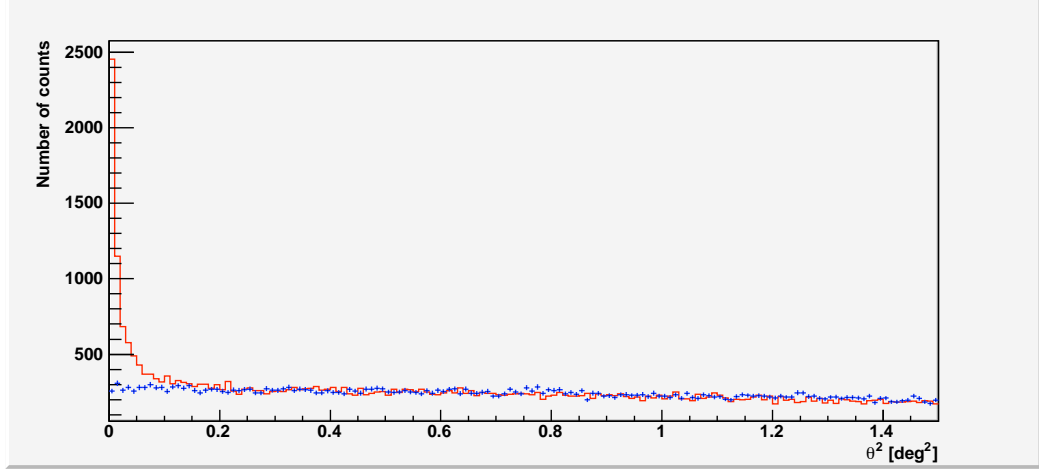


Fig. 4.7. The theta square distribution for 400 minutes of Crab Nebula observations. The red curve is the on source distribution while the blue curve is the of distribution. The excess of events at the source location ($\theta \leq 0.025^\circ$) is clearly evident.

fluctuation in the background. A formula was derived to calculate the confidence level (in gaussian sigma) for low statistics systems by Li & Ma [58]

$$\sigma = \frac{N_{ON} - \alpha * N_{OFF}}{\sqrt{N_{ON} + \alpha^2 * N_{OFF}}}. \quad (4.2)$$

However, this formulation relies heavily on the α parameter described above. By doing a more complete evaluation of this parameter, and exploring where error may exist in the background estimation, an equation that better estimates the background is

$$\sigma = \sqrt{2} \left(N_{ON} * \ln \left[\frac{1 + \Gamma}{\Gamma} \left(\frac{N_{ON}}{N_{OFF}^{Eff}} \right) \right] + N_{OFF}^{Eff} * \ln \left[(1 + \Gamma) \left(\frac{N_{OFF}^{Eff}}{N_{ON} + N_{OFF}} \right) \right] \right)^{1/2}. \quad (4.3)$$

Here the α parameter has been expanded to include fluctuations in the N_{OFF} parameter and its error ΔN_{OFF} , and is now encapsulated by the values

$$\Gamma = \alpha * \left(\frac{\Delta N_{OFF}^2}{N_{OFF}} \right) \quad (4.4)$$

and

$$N_{OFF}^{Eff} = \left(\frac{N_{OFF}}{\Delta N_{OFF}} \right)^2. \quad (4.5)$$

The region of observation is finely binned in the analysis, and a statistical significance is calculated for each bin. Should no signal be present, the distribution should be well fit by a gaussian curve of mean= 0 and $\sigma = 1$; whereas a signal will appear as a deviation in the upper tail of the gaussian distribution.

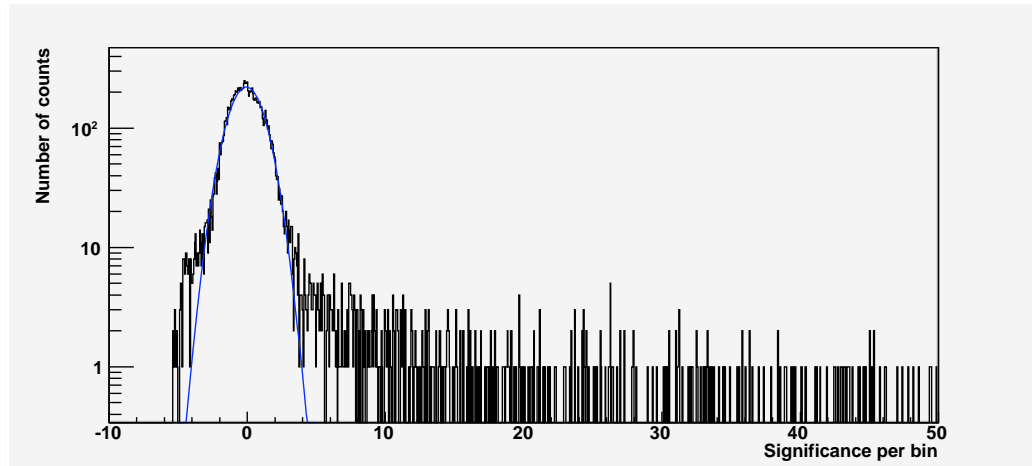


Fig. 4.8. The distribution of significances from 20 hours of observation of the Crab Nebula (histogram). A Gaussian distribution of mean= 0 and $\sigma = 1$ normalized to the number of entries is plotted for comparison (blue curve). The Crab Nebula signal is clearly evident in the excess beyond $\sigma = 4$.

Figure 4.8 displays the distribution of significances for the Crab nebula with many high significance bins appearing in the upper tail of the gaussian curve. This distribution gives a good indication whether the reconstructed sky map does in fact contain a source of high energy gamma rays, or is simply due to statistical fluctuations in the background noise.

Historically the VERITAS Collaboration has required a signal above 5 standard deviations (5σ) in order to claim a detection. However, In the case that no signal is present above this level, a flux upper limit (A) can be calculated using the number of counts from the source region (C) and the number of events from the background region (B). A desired significance level must be chosen to evaluate the upper limit based on the value of $(1 - \epsilon) \times 100\%$, where ϵ is the acceptable background statistical

fluctuation. The upper limit will be determined by integration of the probability density function, hereafter referred to as $g(a)$, above a predetermined threshold (A).

The probability for obtaining C counts above the threshold is determined from

$$P(C) = \frac{\exp^{-(a+B)}(a+B)^C}{C!}, \quad (4.6)$$

which is a Poisson distribution with mean $(a+B)$. According to Bayes theorem [59], this probability can be extended to the probability density function

$$g(a) = N_1 \frac{\exp^{-(a+B)}(a+B)^C}{C!} \quad (4.7)$$

where N_1 is a normalization constant determined by the condition

$$\int_0^\infty g(a) da = 1. \quad (4.8)$$

Assuming a gaussian approximation for equation (4.7) yields the expression

$$g(a) \approx N_3 \frac{\exp^{-(a-C+B)^2/(2\sigma^2)}}{\sqrt{2\pi}\sigma} \quad (4.9)$$

where $\sigma^2 = \sigma_B^2 + C$, σ_B is the background standard deviation and N_3 is a normalization constant. Once $g(a)$ is determined, the probability of a statistical fluctuation of the background greater than A is

$$\int_A^\infty g(a) da = \epsilon. \quad (4.10)$$

Once the value for ϵ is determined by equation (4.10), the probability of having a signal flux above A is $1 - \epsilon$. It can finally be determined that the putative signal flux exceeds A with a significance of $(1 - \epsilon) \times 100\%$. So, even though it may not be possible to report a definitive detection above the 5σ level, it is still possible to make a scientific statement about the maximum source flux [57].

4.5 Ring Background Model

In order to calculate a significance for a given position in the field of view, an estimation of the background must be made. For this purpose, the Ring Background

Model (RBM) is used to estimate the background and calculate the significance distribution on a 2-dimensional map of the sky around the source location. Figure 4.9 displays the parameters that are used to create the sky map.

The circle that appears around the source location identifies the source exclusion region. The exclusion region is necessary so as to not include on-source gamma rays in the background estimation. A second such region is placed around a known bright star in the field of view. This is required to eliminate any adverse effects that the star may have on the estimation of the background. The point (B1,B2) is the test position that the analysis chooses as the probable source position. The reason that this point is off-center is due to the fact that the data was taken in Wobble mode. The circle defined by B5 in the image displays the field of view considered by the analysis, while the circle described by B6 indicates the maximum angular distance, ψ , for the lower wobble position in particular.

The RBM calculates a significance for each bin by placing a ring around the position, A1 in the Figure, to find the number of ON counts. The radius of this ring is known as the angular cut parameter. The area enclosed by the radii A2 and A3 supply the OFF counts. Once the ON and OFF counts are obtained the significance can be calculated for that bin by using equation (4.3). These parameters will be discussed in greater detail in the following subsections.

4.5.1 Source Exclusion Region

To avoid capturing any of the source photons in the calculation of the background, an exclusion region is placed around the source location (region marked exclusion region in Figure 4.9. This naturally will depend on the extension of the source, but by default photons that fall within a 0.3° radius around an assumed point source are excluded. This default value was chosen because it is more than sufficient to exclude point-like sources, which are the primary type of source observed by VERITAS. For extended sources, like PWN, it will be necessary to expand this region depending on

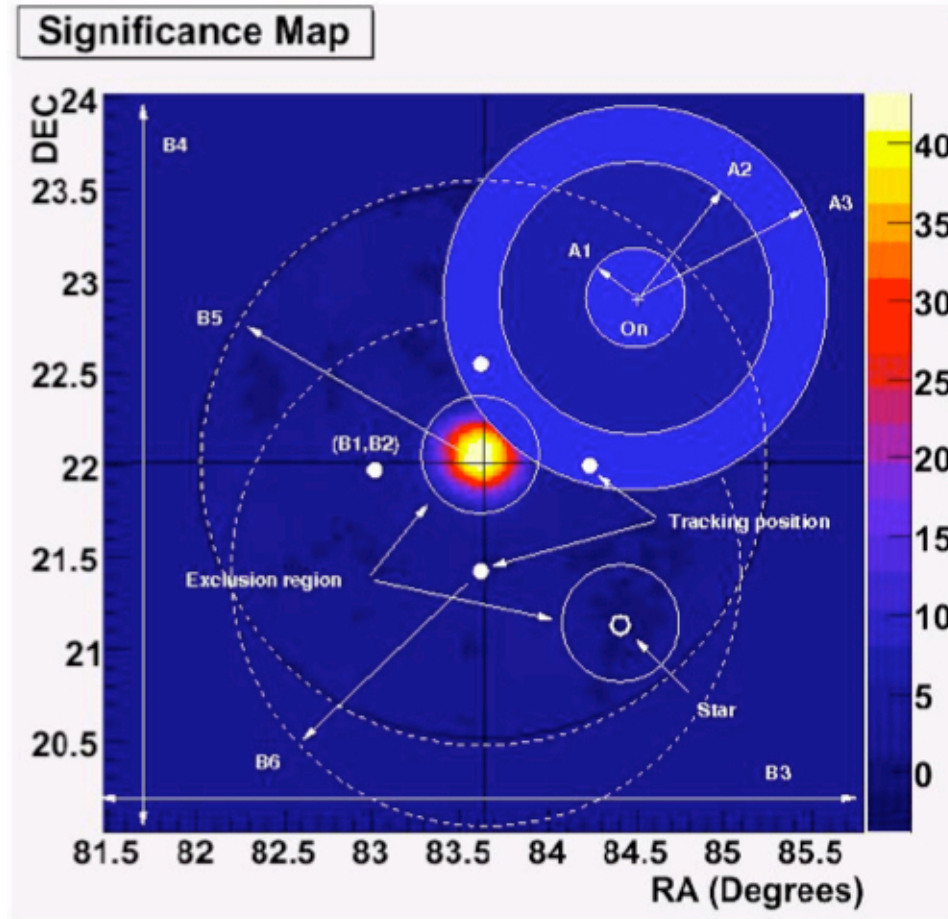


Fig. 4.9. A diagram of the Ring Background Model created by Alexander Konopelko. The various regions are described in the text.

the angular size of the source. Source exclusion regions can be placed around known bright stars in the field of view that would otherwise interfere with the calculation of background events by causing spurious triggers or elevating pixel currents.

4.5.2 Source Test Position

Unless otherwise specified, the position of the source is assumed by the analysis to be in the center of the sky map. From the run header, the analysis picks up the source coordinates and assigns these coordinates to the central pixel of the image. After the RBM calculates the significance of each bin, the analysis may move the source position

slightly to the "center of gravity" of the significance distribution around the source location.

4.5.3 The Angular Cut

The angular cut is used to refine the extent of the expected source region. Based on simulations, an angular cut of 0.158° is optimized for detection of point-like sources. Again, this cut will ultimately be determined by the extent of the source, and must be determined for each individual non-point-like source. In Figure 4.9 the circle labeled "On" will have a radius (A1) determined from the angular cut parameter.

4.5.4 The Background Ring

A background ring is created to determine background events. This ring is determined from two bounds specified by the user. The first bound must be set outside of the exclusion region (appearing as A2 in Figure 4.9), exceeding the angular size of the source. The second bound (A3 in Figure 4.9) is constrained only by the size of the image. However, the values should be chosen so as to optimize the Li & Ma alpha parameter, which relies on the relative areas of the on-source and off-source regions.

4.5.5 The ψ - Parameter

For each event, a source position is reconstructed from the telescope pointing information. Events with particularly large deviations from the expected source region are excluded from the analysis. The ψ -parameter is used to define a circular region outside of which events are excluded (see B6 in Figure 4.9), providing a clean data set. Unless the extent of the source approaches the limit of the camera field of view, this parameter is fixed to exclude only the events near the edges of the field of view.

4.5.6 Size Cut

The size cut is used to set a lower bound for the acceptable event energy. Although, it is desirable to have a lower energy threshold to better understand gamma-ray sources, the associated events can be unreliable due to the lower signal to noise ratio. Standard selection criteria in VEGAS translate to a low energy threshold of between 250 and 400 GeV. However, when it is known that a source has a particularly hard spectrum, it makes sense to increase the minimum size cut to maximize the signal to noise ratio. Although fewer low energy gamma ray events will contribute to the signal, the overall significance of the signal will increase.

4.5.7 Telescope Multiplicity Cut

The VERITAS array currently employs a level three trigger which requires the coincident trigger by two or more of the telescopes. Consequently, the shower reconstruction is far more accurate than using the reconstructed position of a single telescope. It is also possible in the analysis to require a higher level of coincidence in order for an event to be accepted. Doing so further increases the accuracy of the shower reconstruction, but may also increase the energy threshold of the data set. This is because the photon density on the ground from Cherenkov showers is a function of the distance from the shower's core location. Therefore a telescope must be relatively close to the core location to collect enough photons to trigger the telescope for a low energy event, which is not likely to simultaneously occur in three or four telescope multiplicity configurations. However, for sources with a particularly hard spectrum, the loss in low energy events is outweighed by the benefit of increased reconstruction accuracy.

4.6 Extended Source Analysis

In the case where a source is extended, it is necessary to optimize the parameters by which the RBM, described in the previous section, calculates the sky map. Different sets of cuts will need to be developed in order to properly analyze sources with different extensions. For the purposes of this thesis the possible extent of the objects is unknown, though it is not expected to be large. As such, basic modifications to the standard analysis were made to search for only slight extensions of the sources. To accomplish this, the theta squared cut was relaxed from 0.025° to 0.10° . Also, the size cut was increased from 410 digital counts to 650 digital counts which is expected to produce a cleaner data set for sources with hard spectra. There are additional changes that could be made to the cuts to improve sensitivity to an extended source, however optimization of the parameters on a known extended source would be necessary to determine the appropriate values.

4.7 Pulsar Analysis

As discussed earlier, pulsars have distinct periodic emission. However, calculation of the pulse profile requires that corrections be made to the arrival times of the collected events. Naturally, the periodic emission profile is emitted in the rest frame of the star. The phase information of the pulsar will be doppler shifted due to the motion of the solar system and the proper motion of the earth around the center of the solar system. To compensate, the event arrival times at the observatory are transformed from Universal Time (UTC), represented as a Modified Julian Date (MJD), into the Barycentric Dynamical Time (TDB), the arrival time of the event at the center of mass of the solar system, also known as the barycenter. Since the TDB is independent of any motion, the emission profile from the pulsar is preserved.

An additional correction must be made, however, to compensate for the flight time difference from the solar system barycenter to the observatory location on earth. This requires knowing the exact motion of the earth around the solar system barycenter.

Data from the Jet Propulsion Laboratory (JPL) are used to determine the earth's position and velocity at the time of the event, and then the correction can be calculated. This data is extracted from a library file, accessed by the VEGAS analysis, that is maintained by the Science & Technology Facilities Council [60]. Once these values are known, a vector can be constructed from the solar system barycenter to the observatory. Since the data from JPL give the position from the solar system barycenter to the center of the earth, the desired vector arises from the addition of the JPL vector and a vector from the center of the earth to the observatory's location on the earth's surface. The flight time correction is then calculated by taking the resulting vector and dividing by the speed of light.

Once all of the gamma ray event arrival times have been corrected, information about the pulsar can be ascertained. In order to attempt to extract the pulse profile, data about the pulsar's ephemerides must be obtained. The VERITAS collaboration receives monthly ephemerides from the GLAST collaboration which receive data from various radio observatories from around the world. The pulsar data is processed, including performing a discrete Fourier analysis to extract the period and period derivative. These parameters are used to obtain the frequency and frequency derivative. While the frequency information evolves with time, the parameters are accurate enough to only need updating on roughly a monthly basis. At this point a phasogram can be created by folding the data on the frequency information. If the data was obtained over a long period of time, it is necessary to propagate the frequency information throughout the data set. This will likely require the frequency double-derivative information, however this is not always available for all sources.

Once the event data is isolated that made non-zero contributions to the pulsar phaseogram, then the data can be used to construct a two-dimensional sky map containing the pulsar. These events can be used to calculate the significance of the detection, using the method outlined in section 4.4.

5. RESULTS AND DISCUSSION

5.1 Determination of a PWN Target List

In chapter 2 it was discussed that the emission seen from PWNe is powered by the pulsar wind driven into the surrounding medium. For this reason, the nebula luminosity is thought to be directly correlated with the pulsar's spin down power (\dot{E}). However, given that the flux falls with distance to the source, d , as $1/d^2$, the value \dot{E}/d^2 is the primary value we will use to select potential PWNe targets for observation, though preference is given to PWNe that have higher spin down power rather than simply having close proximity. Using this criteria, and restricting the search to sources visible from the northern hemisphere, a target list, (see table 5.1), is compiled from the ATNF pulsar catalogue [22]. From this list the Crab Nebula (with pulsar PSR J0534+2200), the Boomerang Nebula (with pulsar PSR J2229+6114), 3C 58 (with pulsar PSR J0205+6449), and the high spin down pulsar PSR J1930+1852 were selected to be observed by the VERITAS array from fall 2007 - February 2008. Additionally, the pulsar PSR J0631+1036 was observed by the VERITAS array. Even though it does not appear in table 5.1, it does have a high spin down power and only does not make the list due to its relatively far distance.

In order to establish the sensitivity of the array, the Crab nebula data is analyzed. Since definitive detections of these sources, except for the Crab, have never been obtained, the morphology of the sources is not known a priori. For this reason, both a point source and an extended source analysis is carried out for all sources.

Table 5.1
Short list of Northern Hemisphere pulsars, sorted by \dot{E}/d^2 . Data courtesy of ATNF [22].

Pulsar	RA (hms)	Dec (dms)	P (s)	\dot{P} (s s ⁻¹)	\dot{E}/d^2 (ergs kpc ⁻² s ⁻¹)
J0534+2200	34:32.0	22:00:52.06	0.033	4.23×10^{-13}	1.20×10^{38}
J0205+6449	05:37.9	64:49:42.8	0.065	1.94×10^{-13}	2.60×10^{36}
J0633+1746	33:54.2	17:46:12.91	0.237	1.10×10^{-14}	1.30×10^{36}
J1952+3252	52:58.2	32:52:40.53	0.039	5.84×10^{-15}	6.00×10^{35}
J1930+1852	30:30.1	18:52:40.1	0.136	7.51×10^{-13}	4.60×10^{35}
J0659+1414	59:48.1	14:14:21.5	0.384	5.50×10^{-14}	4.60×10^{35}
J2229+6114	29:05.3	61:14:09.3	0.051	7.83×10^{-14}	1.60×10^{35}
J1913+1011	13:20.3	10:11:22.97	0.035	3.37×10^{-15}	1.40×10^{35}
J1740+1000	40:26.0	10:00:06.3	0.154	2.15×10^{-14}	1.30×10^{35}

5.2 The Crab Nebula and Pulsar

The Crab nebula is located approximately 6,500 light-years (2 kpc) from earth in the constellation Taurus, and is roughly 10 light-years (~ 3 pc) across. The nebula, and the associated pulsar, has been one of the most studied objects during the last 100 years. The fact that the Crab Pulsar is the most energetic of all northern hemisphere pulsars, combined with its relatively close proximity, makes the nebula the brightest known PWNe in the northern sky. The Crab Nebula, the standard candle of TeV astronomy, is so bright that the observed fluxes, or flux upper limits, of other sources are commonly represented as fractions of the Crab Nebula. The Crab Nebula is classified as a plerion, a supernova remnant where no remnant shell is detected [29]. Given the relatively young age of the Crab pulsar, it is not completely understood why no radio remnant is detected, though other PWNe, like 3C 58, exhibit similar characteristics [29].

Radio observations reveal a steady flux, with a constant spectral index across the whole nebula. The emission is highly linearly polarized, indicating that the emission mechanism is almost certainly a synchrotron process [29]. The overall flux is in a very slight decline due to the slow expansion of the nebula. Also, small ripples in the nebula have been recently detected in the radio band which correspond to similar features in the optical and X-ray regimes. Observations of the pulsar in all energy regimes show a double peaked emission with a separation of $\sim \frac{1}{2}$ a rotation period.

The nebular emission is less extended at optical energies, and appears as thermal filaments superimposed upon a polarized non-thermal continuum. The region near the pulsar has a low luminosity, probably an indication of where the pulsar wind is un-shocked. This assumption is further confirmed by the fact that just outside this region are a series of bright, non-thermal wisps corresponding to the radio ripples which are found to be variable on month long time scales [61].

The X-ray morphology is characterized by the pulsar outflows, and is clearly dominated by toroidal emission and polar jets [29]. As in the optical regime, the zone near the pulsar is an underluminous region that extends out and terminates in wisps similar to the optical features. The outflow emission is dominated by the torus, which ends far short of the optical and radio nebulae. The spectrum steepens radially in the torus. There are clearly polar jets originating from the neutron star, however the luminosity is only a small fraction of the toroidal emission [61]. There is a nebular component to the X-ray emission which extends all the way up to 25 MeV gamma ray energies, where there is a sharp cut-off presumably from a limit reached by the particle acceleration mechanism [29, 61].

A strong un-pulsed emission is observed starting at roughly 100 GeV that extends all the way up to TeV energies. This emission is thought to arise from inverse Compton scattering off of synchrotron emitting electrons in the nebula. The pulsed component of the emission seen in the radio, optical, and X-ray, appears to cut-off around 10 GeV [29]. A composite image of the Crab Nebula is pictured in Figure 5.1.

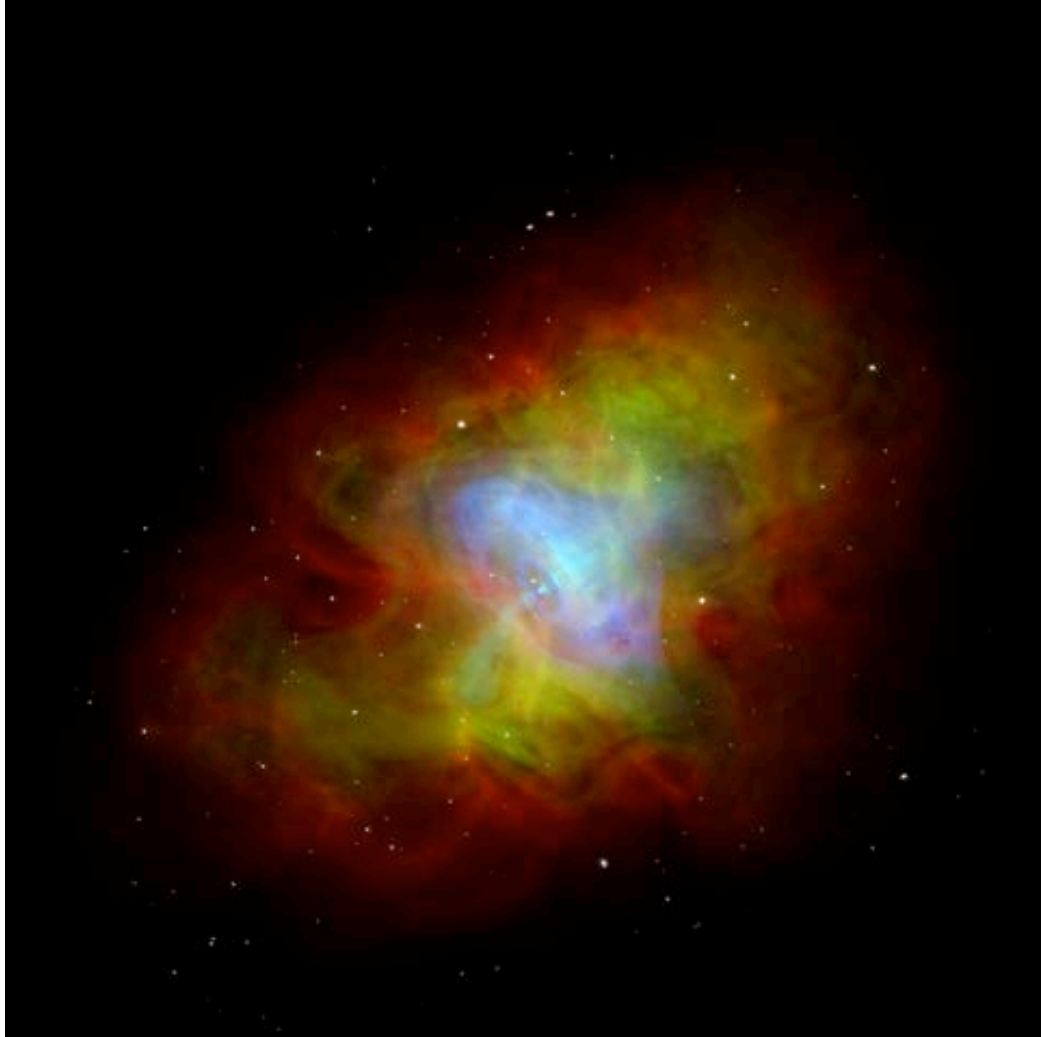


Fig. 5.1. This image is a composite of observations taken in radio (red), optical (green) and X-ray (blue) of the Crab Nebula. The toroidal and polar outflows are evident in the X-ray observations and the synchrotron nebula is clearly visible in the radio and optical observations [62].

5.2.1 The Crab Nebula Data Set

A large amount of Crab Nebula data is taken to calibrate the VERITAS array and refine the data taking and analysis techniques. The data chosen for this work (see Table 5.2) was limited to data taken on clear nights, and for which the array did

not experience hardware problems. Also, for the purpose of consistency, only those runs for which the full 4 telescope array was operational were chosen.

Table 5.2: The log of the data acquired from the fall of 2007 through February 2008 on the Crab Nebula. The VERITAS run number is listed in the first column, while the date is in the format `yyyymmdd`. The 3rd column lists the appropriate laser run. The duration lists the canonical observation time while the livetime lists the amount of time the array was able to accept events during the run. The mode lists the offset size and direction for the Wobble observation. The Sky lists the subjective weather quality determined by the observer.

Run #	Date	Laser #	Duration (minutes)	Livetime (minutes)	Mode	Sky
37039	20071011	37034	20	14.32	0.5W	A
37195	20071014	37177	20	17.74	0.5S	A
37230	20071015	37228	20	14.32	0.5S	A
37266	20071016	37263	20	14.32	0.5W	A
37297	20071017	37296	20	17.65	0.5S	A
37438	20071020	37433	20	17.65	0.5N	A
37945	20071114	37955	20	17.71	0.5N	A
37946	20071114	37955	20	17.66	0.5S	A
37947	20071114	37955	20	17.62	0.5E	A
37948	20071114	37955	20	17.61	0.5W	A
37949	20071114	37955	20	17.60	0.5N	A

Continued on Next Page...

Table 5.2 –Continued

Run #	Date	Laser #	Duration (minutes)	Livetime (minutes)	Mode	Sky
37950	20071114	37955	20	14.32	0.5S	A
38031	20071117	38046	20	14.32	0.5W	A
38033	20071117	38046	20	18.15	0.5N	A
38034	20071117	38046	20	18.11	0.5S	A
38035	20071117	38046	20	18.07	0.5E	A
38061	20071118	38076	20	17.87	0.5N	A
38062	20071118	38076	20	14.32	0.5S	A
38063	20071118	38076	20	17.74	0.5E	A
38064	20071118	38076	20	17.77	0.5W	A
38200	20071204	38186	20	17.58	0.5E	A
Total			420	355.61		

5.2.2 Point-Source Analysis of the Crab Nebula

The Crab nebula has been long established as a point source at TeV energies, not showing evidence of extended emission. For this reason a standard point source analysis was carried out to extract the source signal. The theta squared distribution of the Crab Nebula data, displayed in Figure 5.3(a), indicates an excess of events at the position of the source.

Reconstructing the events on a two dimensional sky map shows the distribution of excess events as they appear on the sky, and again, a clear excess of events is detected, see Figure 5.2(a), at the position of the Crab nebula. The reconstructed

sky map showing the per-bin significance smoothed out over the field of view in Figure 5.2(b) indicates a detection of the source at a confidence of 74.60σ at a rate 9.17 ± 0.18 γ /minute. This corresponds to a sensitivity of $\sim 30.63\sigma/\sqrt{hr}$.

Examination of the distributions of significances plot, Figure 5.3(b), indicates that there is a non-negligible negative excess on the left tail of the distribution. It is normally expected that this portion of the plot would be well formed to a Gaussian curve, while only the right tail of the Gaussian would contain a signal. However, the presence of a negative excess is not uncommon. The presence of a bright star in the field of view, in this case Zeta Tau, can cause several of the camera pixels to be suppressed, ultimately leading to "holes" in the analysis. Recently, it has been determined that operating the array under moderate moonlight, which was done for the PSR J1930+1852 observations, can cause a similar effect. Methods are being developed to compensate for these effects in the analysis, but are not available at this time.

5.2.3 Extended Source Analysis of the Crab Nebula

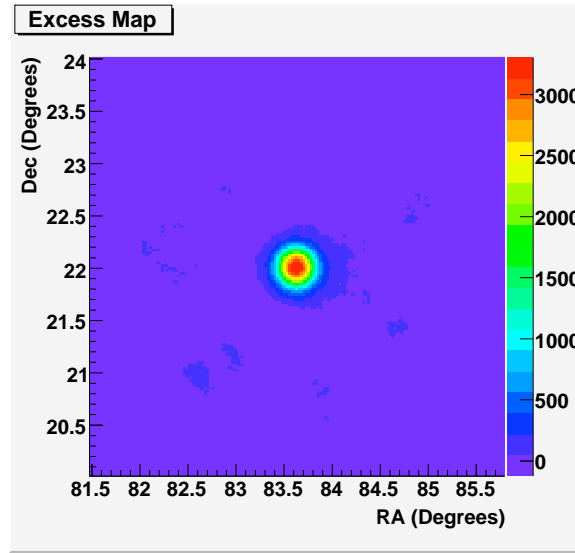
Though the Crab Nebula is known to be a point source, the morphology of the other objects studied in this thesis are not as well understood. In fact many PWNe detected by the H.E.S.S. collaboration are extended [6]. As such an extended source analysis was conducted on the Crab Nebula data in order to demonstrate the utility and sensitivity of the analysis technique on a known source. Since the extent of the sources is currently unknown, a simple set of extended source cuts were chosen to search for slight extensions from the source position. The theta square cut was relaxed slightly from 0.025 square degrees to 0.1 square degrees, so that any photons from an extended nebula would not be excluded. Also, the size cut was increased to 650 digital counts to only focus on the higher energies. This seems reasonable as the PWNe observed by HESS have hard spectra, so setting a higher threshold should not

degrade the sensitivity [6]. The theta squared plot produced from the extended source analysis, Figure 5.5(a), still indicates an excess of events at the source position.

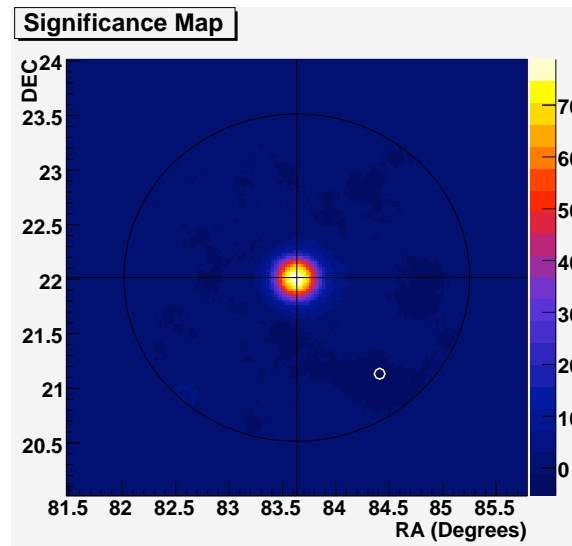
Reconstructing the sky map for the location of the excess events, Figure 5.4(a), still indicates a detection of the source, but the analysis has spread out the events compared to the point source analysis. This is likely due to the combination of the choice of a larger theta squared value coupled with the Gaussian smoothing of the map. Similarly the significance map, Figure 5.4(b), displays a detection of the Crab Nebula at a high significance of 74.63σ , which is nearly identical to the 74.60σ and $30.63\sigma/\sqrt{hr}$ sensitivity obtained for the point source analysis. However, the gamma ray rate is about 30% lower at $6.80 \pm 0.15 \gamma/\text{minute}$, due to the larger size cut.

5.2.4 Energy Spectrum of the Crab Nebula

Since the Crab Nebula is detected with high significance, it is possible for the VEGAS analysis to produce an energy spectrum of the source. Figure 5.6 provides the detected photon flux for energies between about 500 GeV and 10 TeV. The spectrum is clearly well fit to a power-law function with index -2.48 ± 0.07 and a flux above 1 TeV of $(3.5 \pm 0.2) \times 10^{-7} \text{ m}^{-2} \text{ s}^{-1}$. This result is consistent with previous measurements of the Crab Nebula spectrum, and provides a verification of method for this analysis.

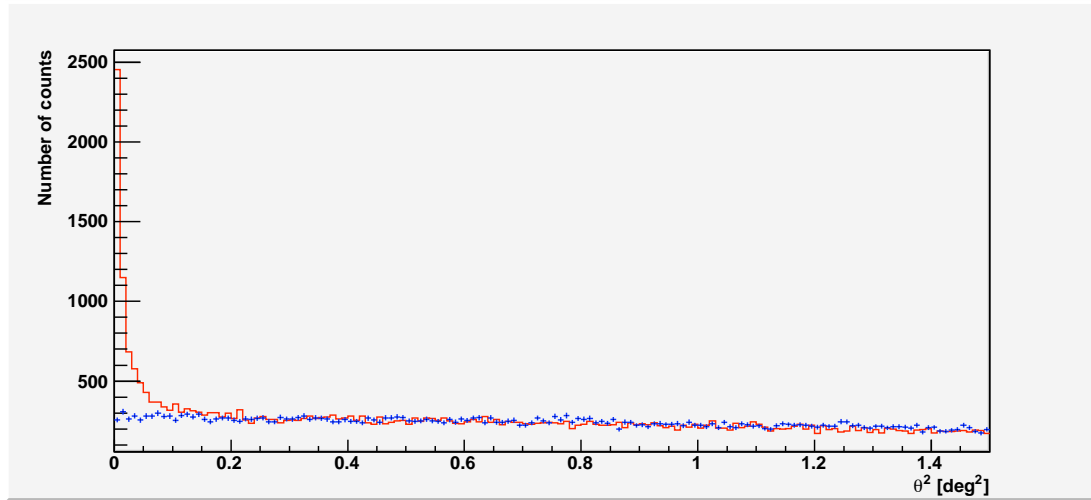


(a)

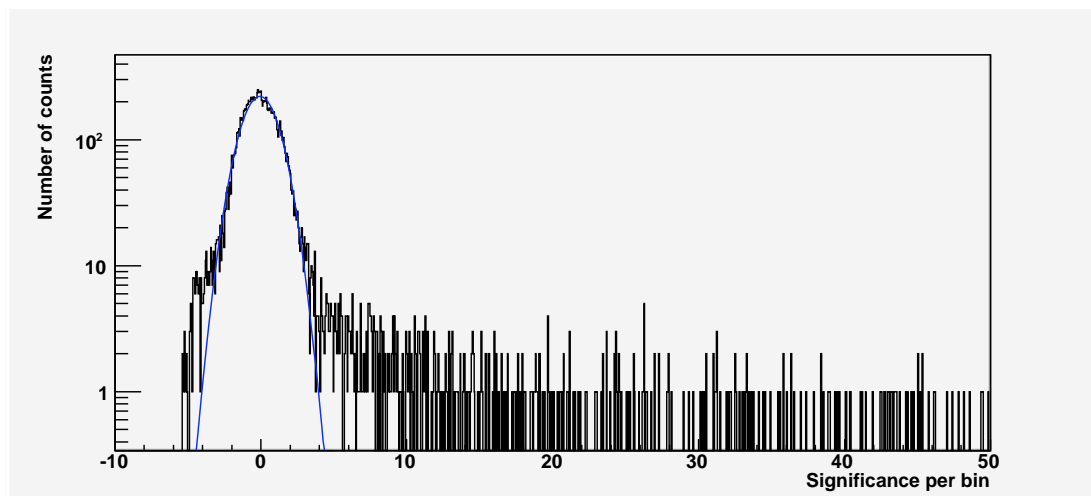


(b)

Fig. 5.2. The sky map of the excess events (a) and significances (b) for the Crab Nebula data listed in Table 5.2. In both maps the ordinate is the right ascension (RA) in degrees while the abscissa is the declination (DEC) in degrees. The color scale indicates the excess in each 0.025° by 0.025° bin. The data were smoothed with a Gaussian smoothing algorithm. The white circle in (b) marks the position of a known star, Zeta Tau, that is bright enough that a significant number of pixels are turned off in the analysis. The Crab Nebula is clearly detected at the canonical source position, indicated by the intersection of the two black lines.

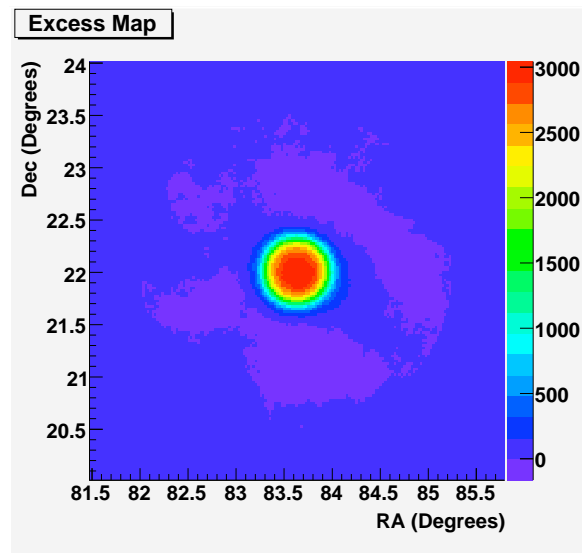


(a)

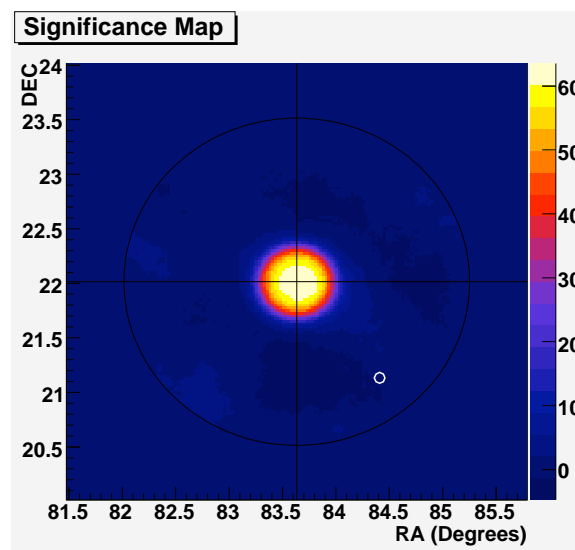


(b)

Fig. 5.3. The theta squared plot of the Crab Nebula data (a). The red histogram is the on source data and the blue histogram is the off source data. A source appears as an excess above the background at values of $\theta^2 \leq 0.025 \text{ deg}^2$. The Crab nebula is clearly detected. The significance distribution for the Crab Nebula data set (b). An excess of significances is clearly observed in the upper tail of the distribution. The blue curve is a gaussian centered at zero, with a width of $\sigma = 1$, that represents the expected distribution of background events.

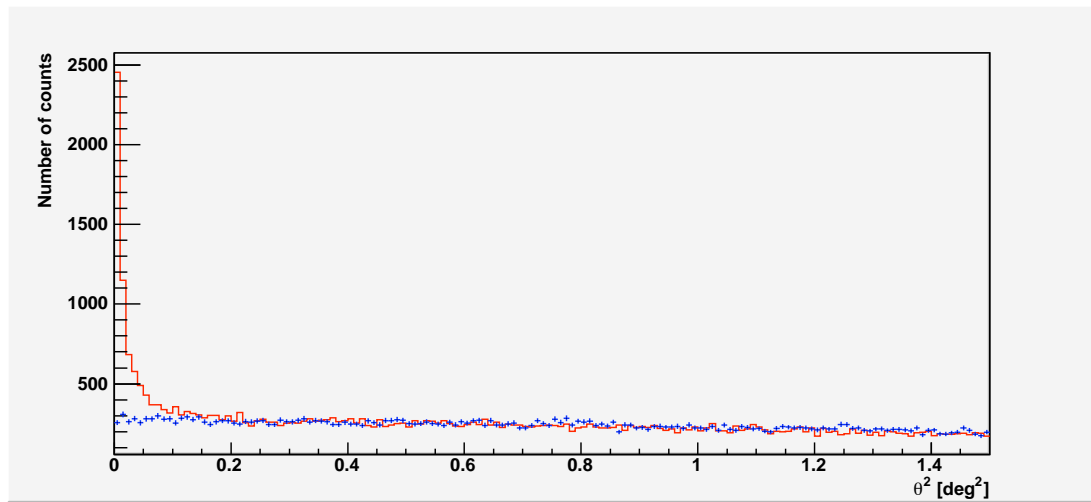


(a)

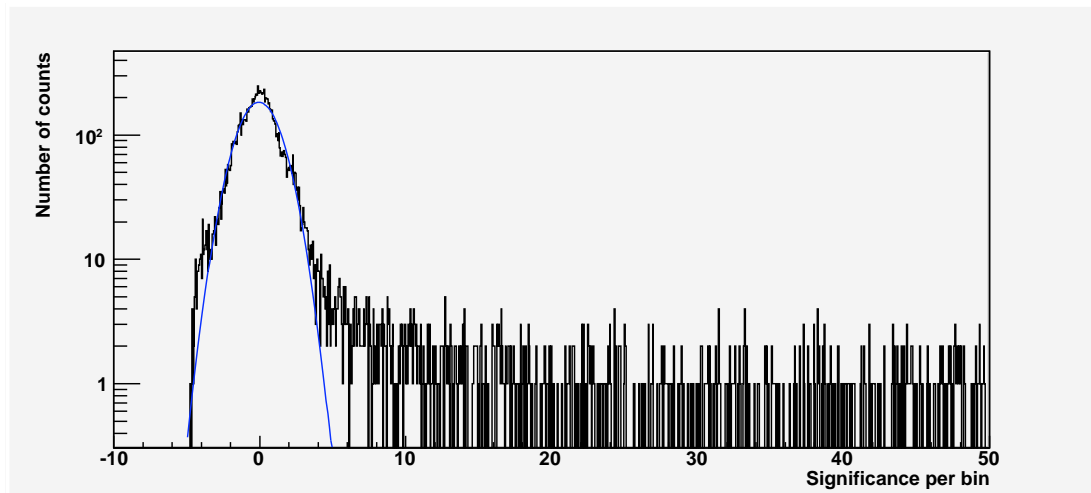


(b)

Fig. 5.4. Same as Figure 5.2, except for the extended source analysis.



(a)



(b)

Fig. 5.5. Same as Figure 5.3 except for the extended source analysis.

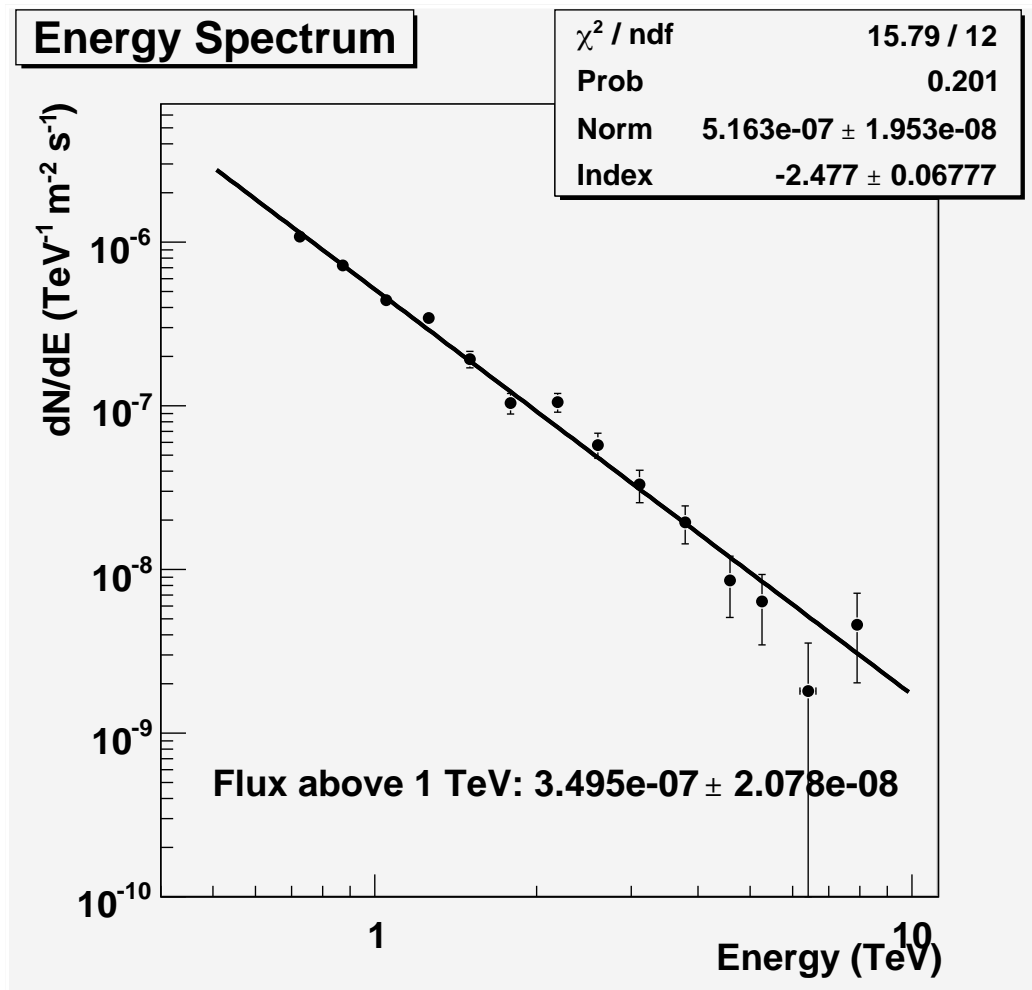


Fig. 5.6. Spectrum of the Crab Nebula for energies above 500 GeV.

5.3 The Boomerang Nebula G106.6+2.9 and Pulsar PSR J2229+6114

The Boomerang Nebula is an extended radio, optical, X-ray and gamma-ray feature associated with the supernova remnant G106.3+2.7 and pulsar PSR J2229+6114. Measurements of the X-ray absorption column density toward the Boomerang Nebula yields a distance estimate of ~ 3 kpc [63], however subsequent radial velocity measurements of the atomic hydrogen and molecular material indicate a distance closer to 0.8 kpc [64]. The supernova remnant G106.3+2.7 is clearly visible within the wind powered nebula, differentiating it from Crab-like sources [65]. The nebula is named for the 3 arcmin shell-like boomerang structure resolved at the northeastern tip of the SNR. Spatially coincident measurements have been made in radio, optical, X-ray and low energy gamma-ray. Low radio luminosity has been reported, which is anomalous given the high spin-down energy of the pulsar. The pulsar PSR J2229+6114 has been detected in both radio and X-rays with a spin-down energy of 2.2×10^{37} ergs s^{-1} , which places it just below the Crab and PSR J0205+6449 pulsars.

The period of the pulsar has been measured to be approximately 51.6 milliseconds, with a period derivative of 7.287×10^{-14} s s^{-1} . These values indicate a characteristic age, $\tau = \frac{P}{2\dot{P}}$, of 10,460 years. The pulsar has a power-law spectrum of photon index of $\Gamma = 1.51 \pm 0.14$ in the X-ray band, and, though the nebula is clearly visible in the optical band, see Figure 5.7, has no obvious optical counterpart [63,64].

5.3.1 Boomerang Nebula Data

Observations of the Boomerang PWN were acquired during the fall of 2007 using the full 4 telescope VERITAS array. A total of 13 hours of quality data was acquired, and is listed in Table 5.3.



Fig. 5.7. Hubble Space Telescope image of the "Boomerang" nebula, G106.6+2.9 [65]. Though there has been no obvious optical detection of the pulsar, the nebular emission is clearly visible to optical telescopes.

Table 5.3: The log of the data acquired during the fall of 2007 on the Boomerang Nebula. The layout of the table is the same as Table 5.2.

Run #	Date	Laser #	Duration (minutes)	Livetime (minutes)	Mode	Sky
36543	20070918	36533	20	17.68	0.5E	B+
36544	20070918	36533	20	17.72	0.5W	B+

Continued on Next Page...

Table 5.3 –Continued

Run #	Date	Laser #	Duration (minutes)	Livetime (minutes)	Mode	Sky
36588	20070919	36601	20	17.89	0.5N	B
36589	20070919	36601	20	17.89	0.5S	B
36590	20070919	36601	20	17.74	0.5E	B
36591	20070919	36601	20	17.96	0.5W	B-
36890	20071008	36953	20	17.82	0.5E	B+
36891	20071008	36953	20	17.86	0.5W	B+
36893	20071008	36953	20	17.87	0.5N	B+
36944	20071009	36953	20	17.91	0.5S	B+
36945	20071009	36953	20	17.95	0.5N	B+
37020	20071011	37034	20	17.78	0.5S	A
37023	20071011	37034	20	17.81	0.5W	A
37111	20071013	37148	20	17.91	0.5E	A
37113	20071013	37148	20	17.88	0.5W	A
37166	20071014	37177	20	17.87	0.5E	A
37167	20071014	37177	20	17.92	0.5N	A
37168	20071014	37177	20	17.95	0.5S	A
37211	20071015	37228	20	17.89	0.5E	A
37212	20071015	37228	20	17.93	0.5W	A
37213	20071015	37228	20	17.97	0.5N	A
37242	20071016	37263	20	17.75	0.5S	A
37244	20071016	37263	20	17.94	0.5S	A
37279	20071017	37296	20	17.70	0.5W	A
37502	20071101	37510	20	17.83	0.5W	A
37503	20071101	37510	20	17.83	0.5E	A

Continued on Next Page...

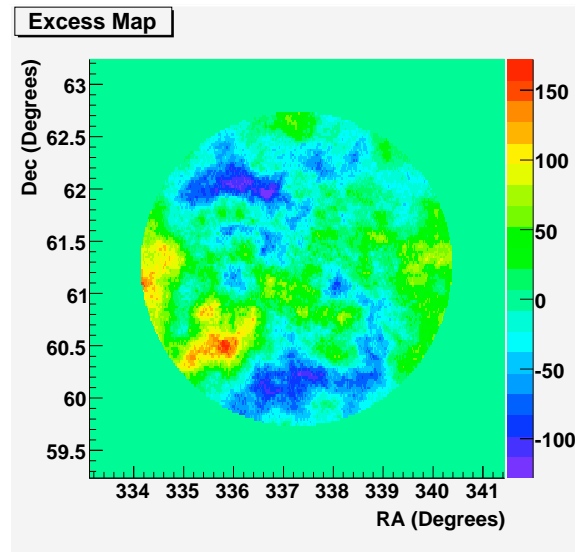
Table 5.3 –Continued

Run #	Date	Laser #	Duration (minutes)	Livetime (minutes)	Mode	Sky
37519	20071102	37530	20	17.83	0.5N	A
37520	20071102	37530	20	17.83	0.5S	A
37546	20071103	37557	20	16.95	0.5N	A
37548	20071103	37557	20	17.78	0.5S	A
37610	20071105	37623	20	17.92	0.5N	A
37611	20071105	37623	20	17.91	0.5S	A
37756	20071109	37780	20	17.94	0.5E	A
37757	20071109	37780	20	18.00	0.5W	A
37821	20071111	37845	20	17.77	0.5N	A
37822	20071111	37845	20	17.77	0.5S	A
Total			720	641.95		

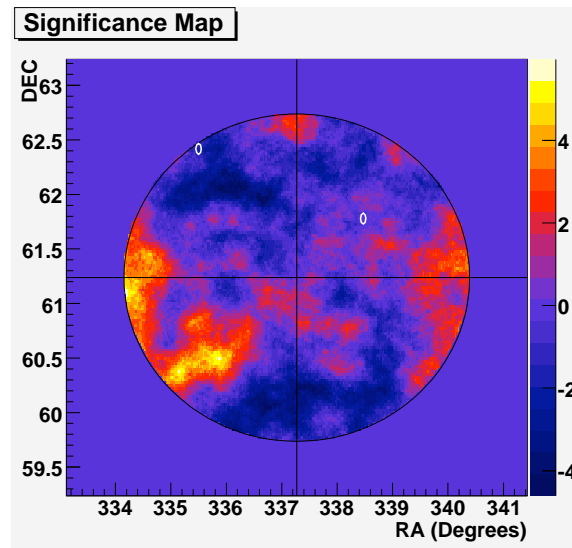
5.3.2 Point-Source Analysis of the Boomerang Nebula

All sources are initially analyzed as point sources. The analysis was carried out using the methods outlined in Chapter 4 of this thesis. Standard cuts, see Table 4.2, were applied so that a direct comparison with the Crab nebula can be made. The theta squared distribution, Figure 5.9(a), displays no excess of events at the apparent source position.

The excess and significance maps, Figures 5.8(a) and 5.8(b), are also consistent with a null detection. The distribution of significances is displayed in Figure 5.9(b) and is consistent with what would be expected from a random distribution in the



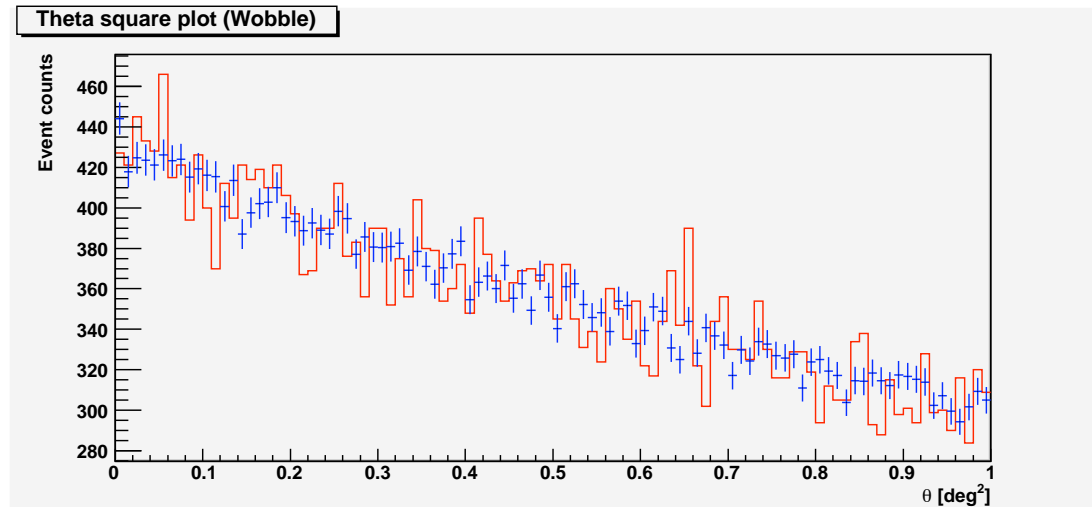
(a)



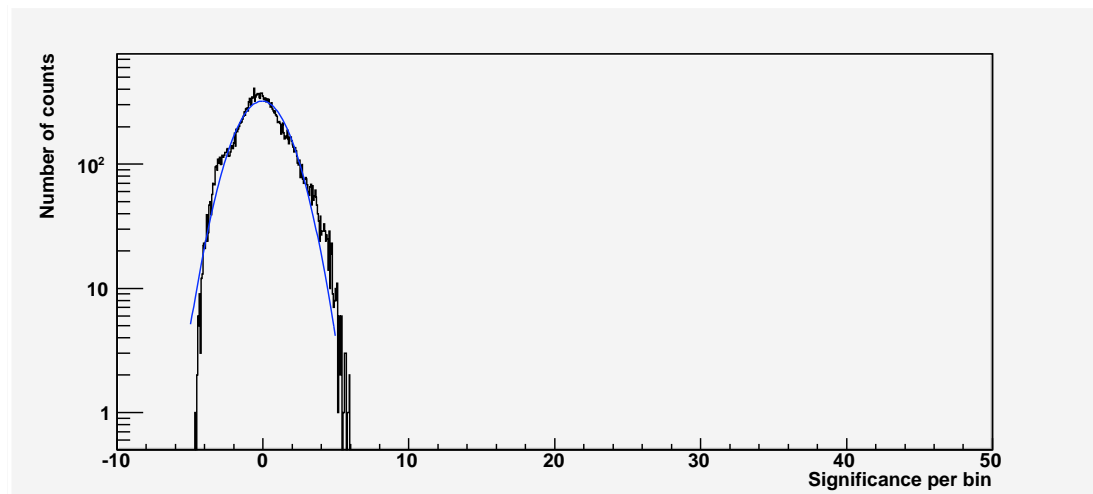
(b)

Fig. 5.8. Same as Figure 5.2, except for the Boomerang Nebula.

VEGAS analysis. At the source location the significance and rate are consistent with statistical fluctuations of the background.



(a)



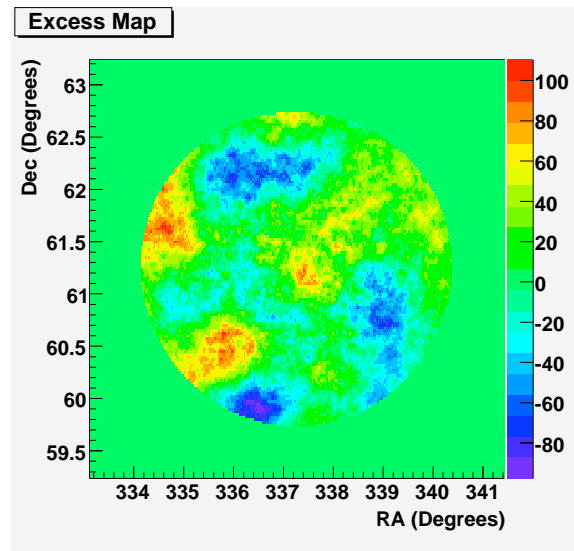
(b)

Fig. 5.9. Same as Figure 5.3, except for the Boomerang Nebula.

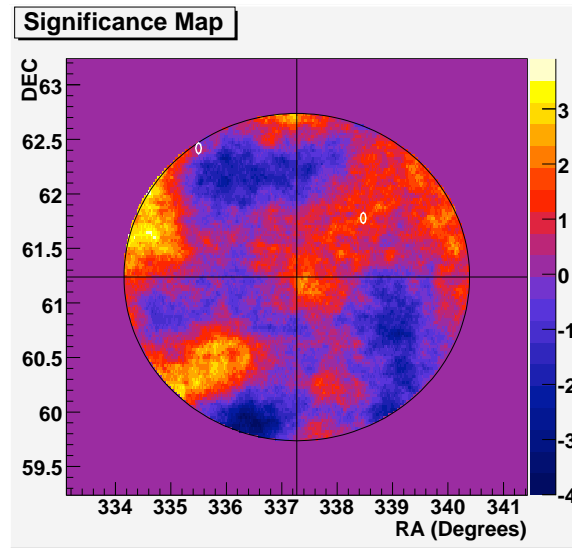
5.3.3 Extended Source Analysis of the Boomerang Nebula

Since some PWN are observed to be extended objects in TeV gamma rays, it makes sense to apply a different set of cuts looking for a signal from an extended source. An extended source analysis was performed like the analysis carried out on

the Crab Nebula. The theta squared distribution for the extended source analysis, Figure 5.11(a), is consistent with a null result for the detection of the source.

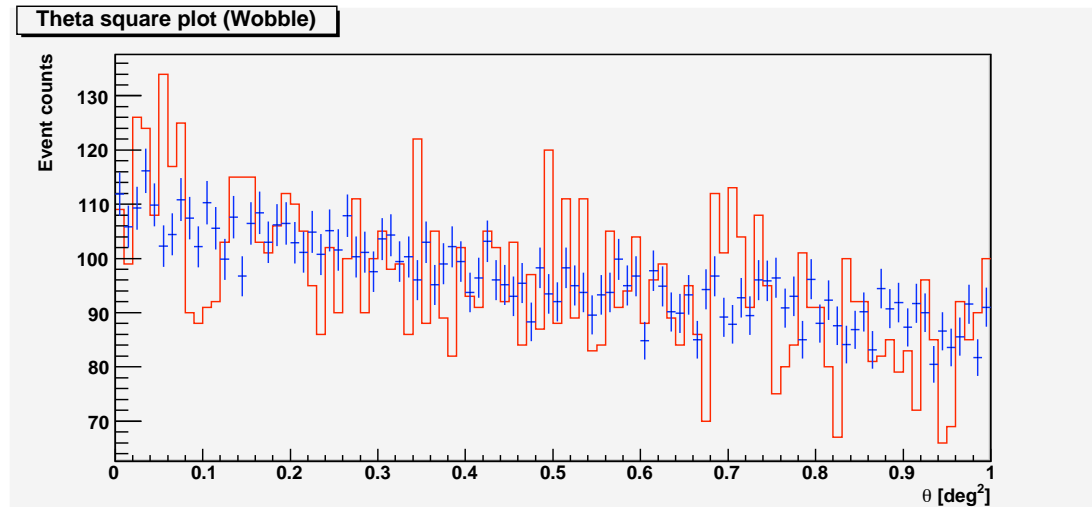


(a)

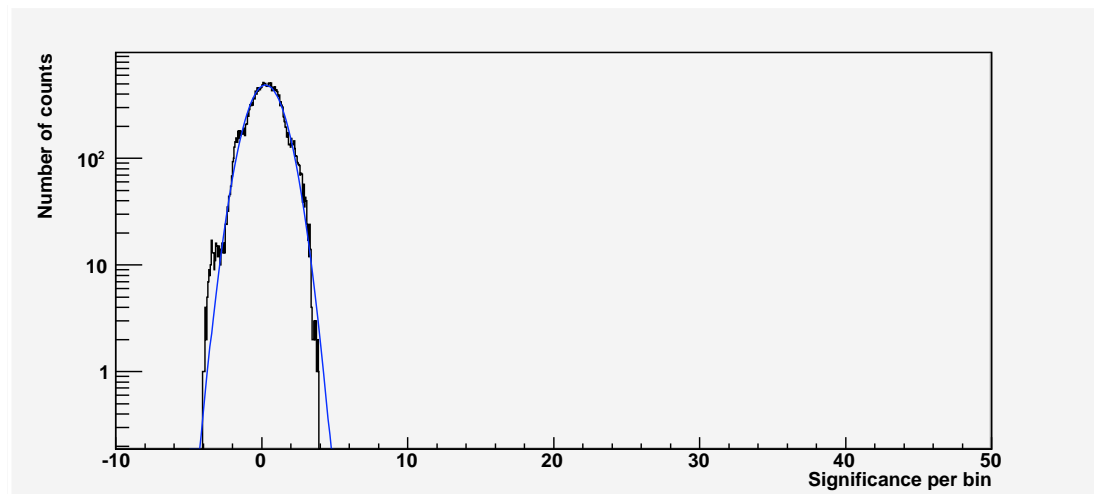


(b)

Fig. 5.10. Same as Figure 5.7, except for the extended source analysis.



(a)



(b)

Fig. 5.11. Same as Figure 5.8, except for the extended source analysis. There exists a slight negative excess on the left tail of the excess significances plot (b). The presence of bright stars in the field of view has been shown to cause this effect in some cases.

The excess and significance maps, Figures 5.10(a) and 5.10(b), produced from the extended source analysis, also do not indicate a detection at the source location. The significance and rate observed are consistent with a null detection.

5.3.4 Discussion of the Boomerang Nebula Results

The choice to observe the boomerang nebula for only 15 hours was made under the assumption that most of the detections of PWNe, predominately by H.E.S.S., indicate a flux that is in excess of 5% of the Crab [6]. A flux upper limit of 1.53% of the Crab flux was calculated using the method of O. Helene [57]. This calculation assumes a point-like source, which may not be reflective of the true nature of the source.

5.4 Pulsar Wind Nebula 3C 58

The source 3C 58, pictured in Figure 5.12, is a prime target to detect very high energy gamma ray emission. This pulsar wind nebula was the second plerion discovered after the Crab Nebula. It is thought to be the result of the supernova explosion SN 1181. The nebula is located about 3.2 kpc away in the galactic plane within the constellation Cassiopeia [66]. The synchrotron nebula is powered by a pulsar that, until recently, had been unseen. The Chandra X-ray observatory resolved the pulsed emission and determined a period of about 65.67 milliseconds and a period derivative of $1.935 \times 10^{-13} \text{ s s}^{-1}$, giving the pulsar a characteristic age of roughly 5400 years. However, this value is inconsistent with the presumably associated supernova explosion.

Although the pulsar, PSR J0205+6449, has a high spin-down energy, second only to the Crab pulsar, of $2.7 \times 10^{37} \text{ ergs s}^{-1}$ the X-ray luminosity of 3C 58 is a factor of 2000 less than the Crab Nebula. The order of magnitude difference in spin-down power may explain at least part of the difference in the nebula luminosity. Other contributing factors may be the different morphology of the nebula. Although 3C 58 is younger than the Crab, the nebula is considerably larger. Also of note is the fact that the optical and radio emission have noticeably slower expansion velocities than that of the Crab [67]. The radio luminosity is about a factor of 10 less than the Crab, but has a steep spectral break at $\approx 50 \text{ GHz}$. The radio luminosity is increasing, perhaps suggesting that the unseen supernova remnant reverse shock may be interacting with the nebula [29].

5.4.1 Data taken on 3C 58

During the fall of 2007 an initial 13 hours of quality data was acquired by the VERITAS array. Because 3C 58 is considered a high priority target for VERITAS, given the likelihood of making a positive detection, data was only taken on clear

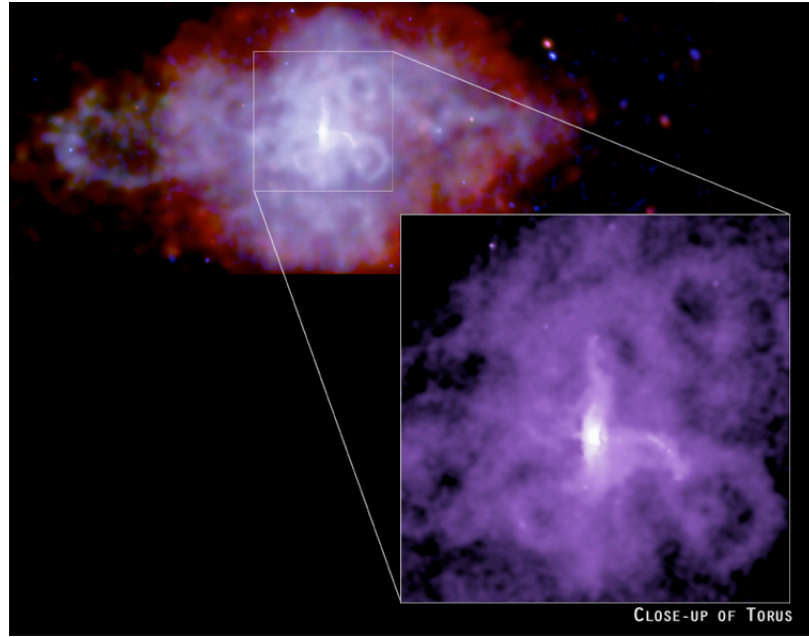


Fig. 5.12. Chandra Image of the 3C 58 nebula around PSR J0205+6449. The inset image is a close-up image of the toroidal and polar outflows from the pulsar [68].

weather nights. Additionally only data which exhibited no hardware problems were chosen for this data set, outlined in table 5.4.

Table 5.4: The log of the data acquired during the fall of 2007 on 3C 58. The layout of the table is the same as Table 5.2.

Run #	Date	Laser #	Duration (minutes)	Livetime (minutes)	Mode	Sky
36552	20070918	36533	20	17.77	0.5N	B+
36598	20070919	36601	20	17.81	0.5N	B

Continued on Next Page...

Table 5.4 –Continued

Run #	Date	Laser #	Duration (minutes)	Livetime (minutes)	Mode	Sky
36599	20070919	36601	20	17.85	0.5S	B
36853	20071007	36858	20	18.09	0.5E	B
36855	20071007	36858	20	18.03	0.5S	B
36899	20071008	36953	20	17.87	0.5W	B+
36900	20071008	36953	20	17.87	0.5S	B+
37084	20071012	37090	20	17.80	0.5N	A
37085	20071012	37090	20	17.87	0.5S	A
37119	20071013	37148	20	17.87	0.5N	A
37120	20071013	37148	20	17.81	0.5E	A
37121	20071013	37148	20	17.94	0.5W	A
37122	20071013	37148	20	17.94	0.5N	A
37173	20071014	37177	20	17.85	0.5N	A
37174	20071014	37177	20	17.86	0.5S	A
37175	20071014	37177	20	17.91	0.5W	A
37176	20071014	37177	20	17.82	0.5E	A
37218	20071015	37228	20	17.89	0.5N	A
37219	20071015	37228	20	17.90	0.5S	A
37220	20071015	37228	20	17.93	0.5W	A
37221	20071015	37228	20	17.79	0.5E	A
37248	20071016	37263	20	17.71	0.5E	A
37250	20071016	37263	20	17.80	0.5S	A
37251	20071016	37263	20	17.79	0.5N	A
37288	20071017	37296	20	17.68	0.5N	A
37289	20071017	37296	20	17.93	0.5S	A

Continued on Next Page...

Table 5.4 –Continued

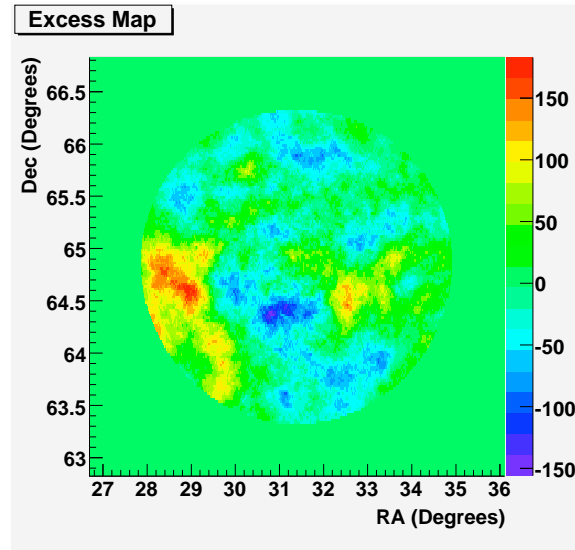
Run #	Date	Laser #	Duration (minutes)	Livetime (minutes)	Mode	Sky
37290	20071017	37296	20	17.93	0.5E	A
37291	20071017	37296	20	17.96	0.5W	A
37407	20071019	37415	20	17.80	0.5W	A
37408	20071019	37415	20	17.81	0.5E	A
37526	20071102	37530	20	17.88	0.5N	B
37559	20071103	37557	20	17.80	0.5E	A
37560	20071103	37557	20	17.90	0.5W	A
Total			660	589.44		

5.4.2 Point-Source Analysis for 3C 58

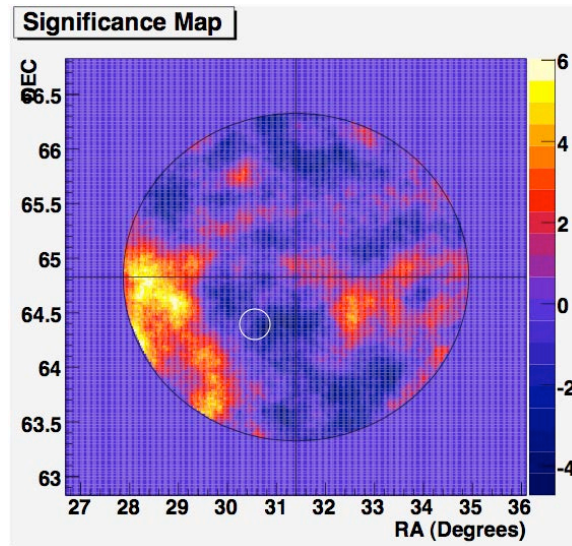
As outlined in Chapter 4 of this thesis, a standard point-source analysis was applied to the data gathered by the VERITAS array. Given the point source nature of the Crab nebula, of which this source is closely associated, this type of analysis is the most obvious.

With a high spin down power, 3C 58 is a promising target for gamma ray emission. However, the initial data set does not show a clear indication of a detection. The theta squared plot for the point source analysis, Figure 5.14(a), does not indicate an excess of events at the source position.

The two dimensional sky maps, Figures 5.13(a) and 5.13(b), produced by the analysis do not indicate an excess of events or any significances above the three sigma level at the the putative source position. The significance and rate at the

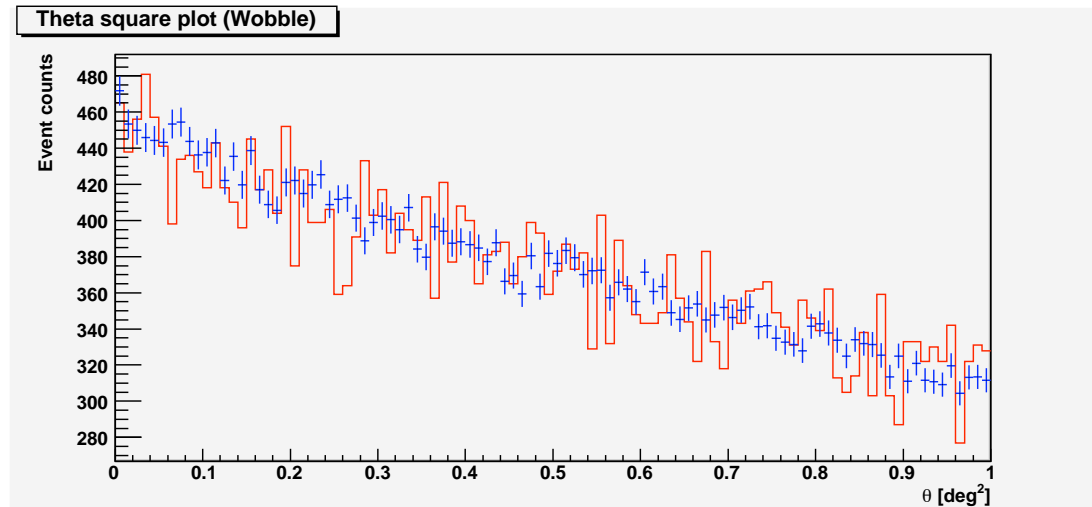


(a)

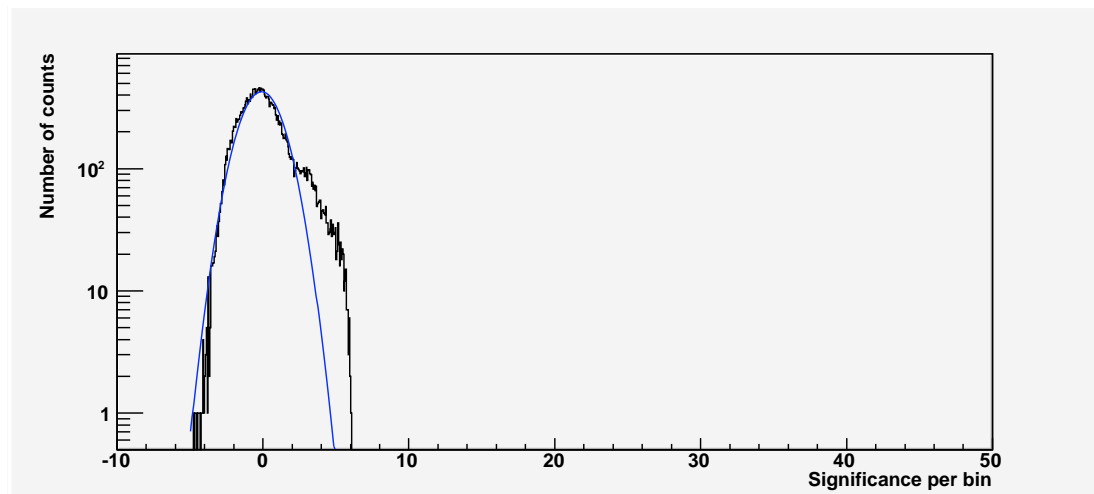


(b)

Fig. 5.13. Same as Figure 5.2, except for 3C 58. The white circle in the significance map (b), indicates the position of a bright star in the field of view. There is clearly an excess about 2.5 degrees west of the putative source location. This position is not coincident with any known sources of TeV gamma rays. Further study is warranted to establish if this feature is indeed a real source.



(a)



(b)

Fig. 5.14. Same as Figure 5.3, except for 3C 58. There is an excess of significances on the right tail of the distribution. This excess corresponds to the feature observed in the 3C 58 sky maps (see Figure 5.12).

point source location is consistent with a null detection, though there appears to be a nearly 6σ extended feature west of the source location. This feature is reflected in the distribution of significances, shown in Figure 5.14(b). Further study of this region is

warranted to determine if the extended feature is indeed a source of very high energy gamma rays or a background fluctuation.

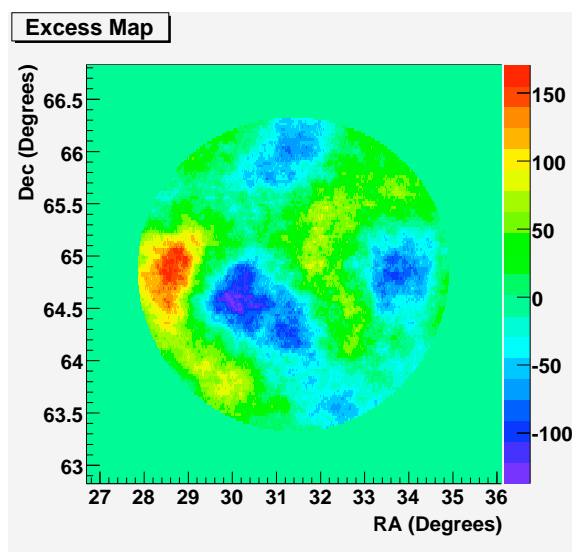
5.4.3 Extended Source Analysis for 3C 58

Given the extended nature of the PWNe, an extended source analysis is carried out to attempt to extract a signal from the surrounding region. However, searching for an extended source still does not yield a detection of the source. The theta squared plot, Figure 5.16(a), does not indicate any excess of events near the putative source position.

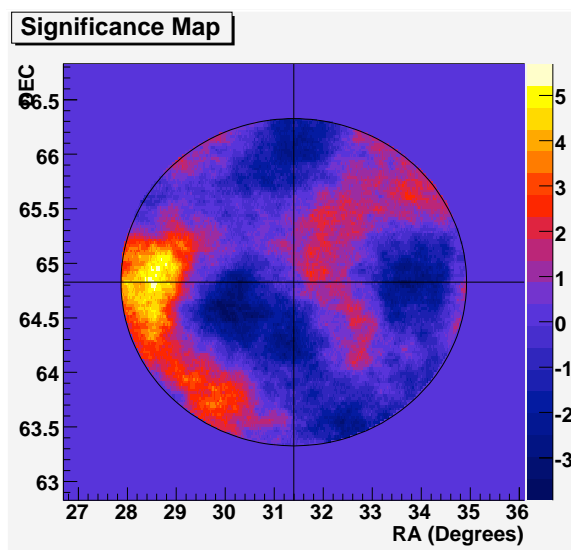
The excess and significance maps for the extended source analysis, Figures 5.15(a) and 5.15(b), indicate that there is no significant source or source extension at the source position, with the observed significance and rate again consistent with a null detection. However, the sky maps display the same extended feature west of the putative source position, which is confirmed by the excess significances distribution (Figure 5.16(b)).

5.4.4 Discussion of the 3C 58 Results

Although there is no detection of 3C 58, a flux upper limit of 1.58% of the Crab flux is calculated using the Helene upper limit method [57]. This is the tightest upper limit placed on this source to date. However, of perhaps greater interest is the appearance of a possible extended source west of 3C 58. There is no obvious counterpart to this feature. But, future observations around this area should resolve this feature.

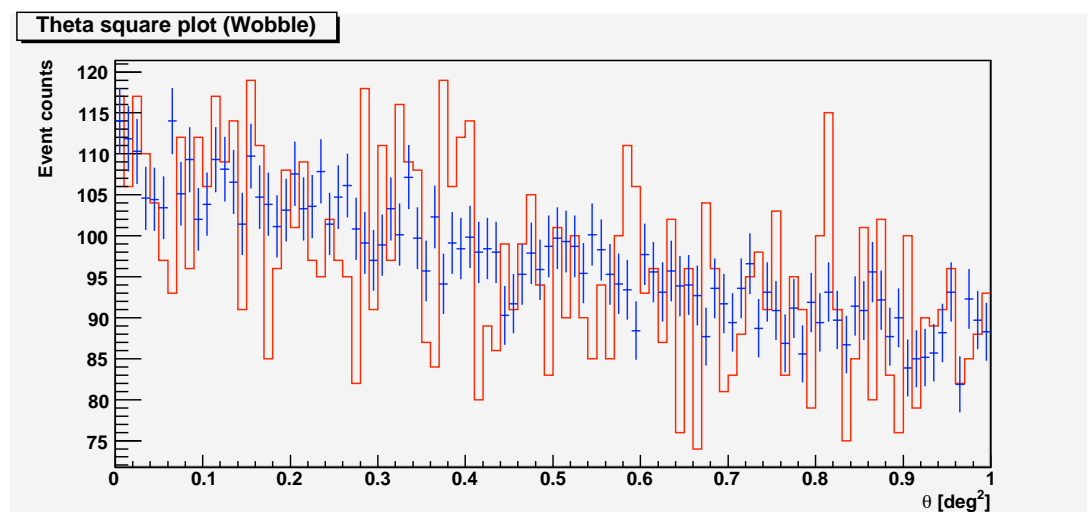


(a)

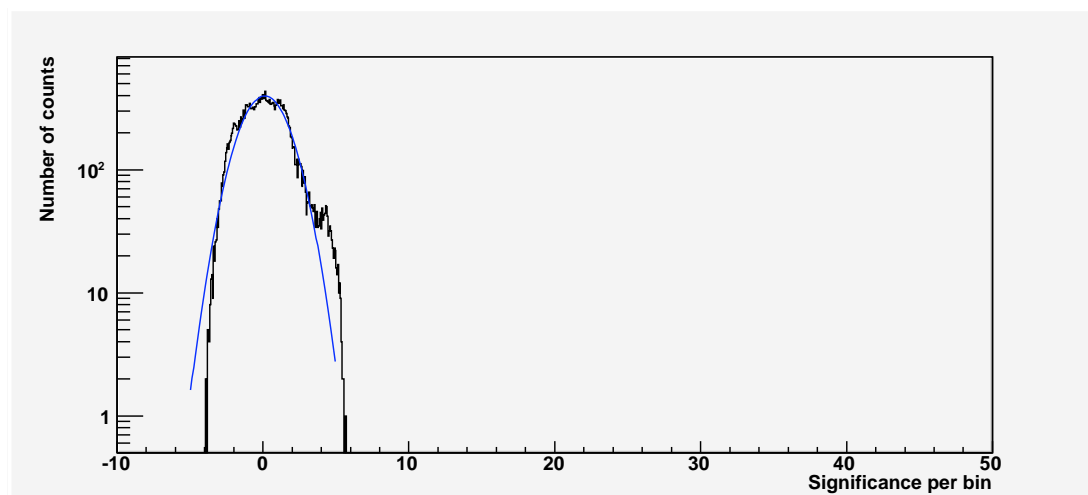


(b)

Fig. 5.15. Same as Figure 5.13, except for the extended source analysis. The same extended feature is present in the sky maps that was indicated in the point source analysis.



(a)



(b)

Fig. 5.16. Same as Figure 5.14, except for the extended source analysis. The same extended feature is present in the excess significances plot that was indicated in the point source analysis.

5.5 PSR J0631+1036

Though PSR J0631+1036 is the oldest pulsar considered in this study at roughly 43,000 years, it is still considered young by pulsar evolution standards. With a spin period of 288 milliseconds this pulsar is also the slowest rotator. The distance to the object is estimated to be 6.5 kpc based on an observed dispersion measure of 125 pc cm^{-3} . However, it is noted that the star is located in the dark cloud LDN 1605, which could explain the high column density. Taking this into account, it has been estimated that the distance is more on the order of 1 kpc. The spin down power is calculated to be $1.7 \times 10^{35} \text{ ergs s}^{-1}$, which is three orders of magnitude less than the Crab [69].

X-ray photons were detected by the Einstein X-ray experiment. The error circle for the source was quite large, and therefore it was difficult to pin-point the pulsar's position. Further observations of the region by radio telescopes determined that the pulsar actually lay outside of the 90% Einstein X-ray error circle. Analysis of X-ray data taken by ASCA claimed a coincidental detection of the radio source with the same 288 millisecond period and that the source exhibited the same properties as older low energy gamma ray pulsars like Geminga. Recently, however, the XMM satellite did an extensive search of the region and found no evidence of X-ray emission from within or near the Einstein error circle. Ultimately, there is a great deal of uncertainty associated with this source, which means that any potential detection of the pulsar of an associated PWN in very high energy gamma rays would be an important discovery [69].

5.5.1 Data taken on PSR J0631+1036

Recently the VERITAS array undertook observations of the nebula surrounding the pulsar PSR J0631+1036. Table 5.5 is the log of the data taken during the fall of 2007 under clear weather conditions where no hardware problems were indicated. The assumption made is that the gamma ray photon flux would be above the 5%

Crab level based on the detections of PWNe by H.E.S.S.. For this reason only 10 hours of quality data were requested in order to detect at least a 5% Crab flux. A little more than 11 hours of data have been acquired to date.

Table 5.5: The log of the data acquired during the fall of 2007 on PSR J0631+1036. The layout of the table is the same as Table 5.2.

Run #	Date	Laser #	Duration (minutes)	Livetime (minutes)	Mode	Sky
38540	20071231	38539	20	17.90	0.5N	A
38541	20071231	38539	20	17.85	0.5S	A
38542	20071231	38539	20	17.80	0.5E	A
38543	20071231	38539	20	17.76	0.5W	A
38544	20071231	38539	20	17.73	0.5N	A
38545	20071231	38539	20	17.70	0.5S	A
38546	20071231	38539	20	17.71	0.5E	A
38563	20080101	38562	20	17.90	0.5W	A
38564	20080101	38562	20	17.86	0.5N	A
38565	20080101	38562	20	17.81	0.5S	A
38566	20080101	38562	20	17.75	0.5E	A
38567	20080101	38562	20	17.71	0.5W	A
38568	20080101	38562	20	17.71	0.5N	A
38569	20080101	38562	20	17.73	0.5S	A
38624	20080105	38635	20	18.02	0.5E	B-
38625	20080105	38635	20	17.96	0.5W	B-
38626	20080105	38635	20	17.93	0.5N	B-

Continued on Next Page...

Table 5.5 –Continued

Run #	Date	Laser #	Duration (minutes)	Livetime (minutes)	Mode	Sky
38690	20080110	38685	20	17.85	0.5E	A
38691	20080110	38685	20	17.76	0.5W	A
38692	20080110	38685	20	17.74	0.5N	A
38693	20080110	38685	20	17.81	0.5S	A
38694	20080110	38685	20	17.86	0.5E	A
38695	20080110	38685	20	17.92	0.5W	A
38837	20080114	38828	20	17.88	0.5N	B-
38838	20080114	38828	20	17.92	0.5E	B
39142	20080207	39149	20	17.80	0.5S	A
39143	20080207	39149	20	17.75	0.5E	A
39144	20080207	39149	20	17.72	0.5W	A
39145	20080207	39149	20	17.75	0.5N	A
39174	20080208	39195	20	17.79	0.5S	A
39176	20080208	39195	20	17.73	0.5E	A
39177	20080208	39195	20	17.70	0.5W	A
39179	20080208	39195	20	16.42	0.5S	A
39180	20080208	39195	20	17.73	0.5E	A
Total			680	603.95		

5.5.2 Point-Source Analysis of PSR J0631+1036

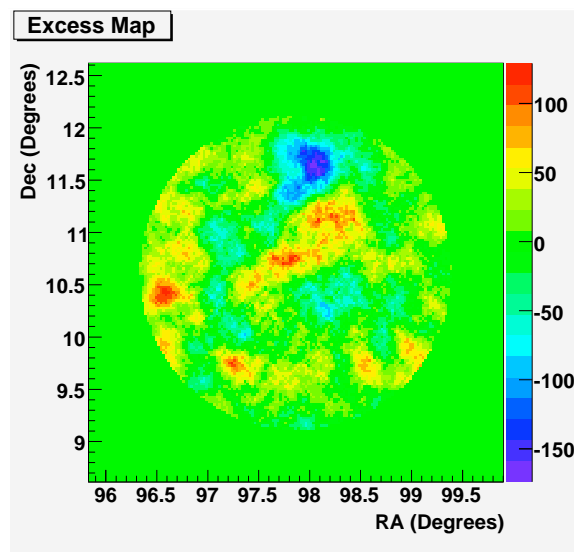
The standard point source analysis does not indicate a strong gamma ray source at the pulsar's location. The theta square plot, Figure 5.18(a), does not show an excess of events from the pulsar position. The sky maps contain several low significance regions, though none rise above the 5 sigma threshold. Ultimately, the significance found at the source position is consistent with a null detection.

5.5.3 Extended Source Analysis of PSR J0631+1036

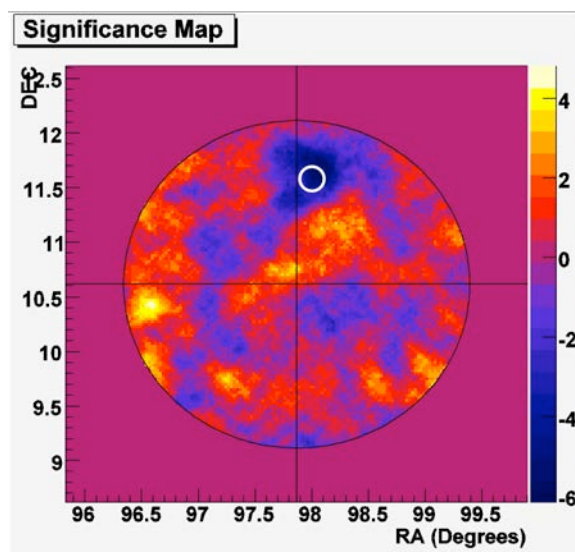
An extended source analysis was performed on PSR J0631+1036. However, the theta square plot, Figure 5.20(a), still has no indication of a large event excess. The sky maps, Figures 5.19(a) and 5.19(b), are consistent with a non-detection from the region.

5.5.4 Discussion of the PSR J0631+1036 Results

Results of the analysis yield no detection of PSR J0631+1031. An upper limit of roughly 2.1% of the Crab is the tightest limit placed on this source to date.

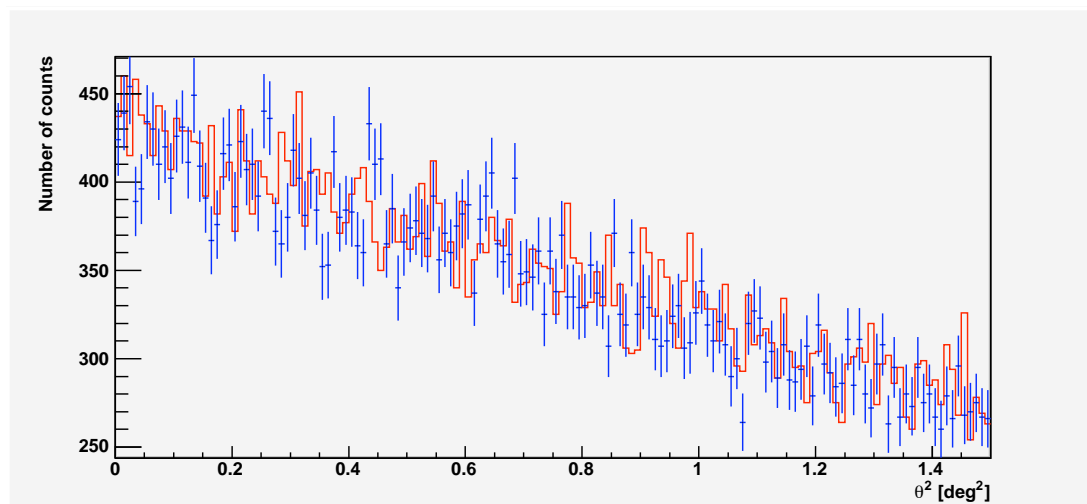


(a)

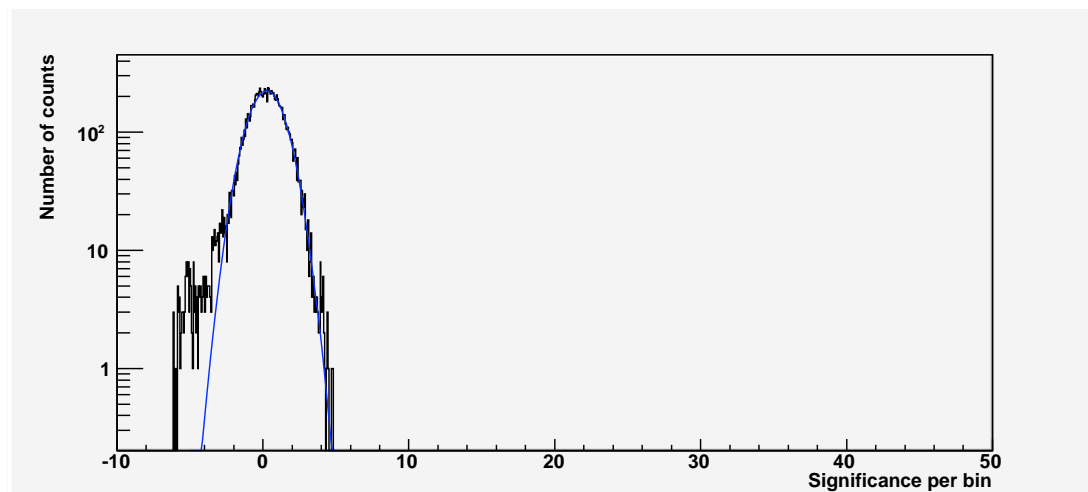


(b)

Fig. 5.17. Same as Figure 5.2, except for PSR J0631+1031. The white circle in the map indicates the position of a bright star in the field of view.

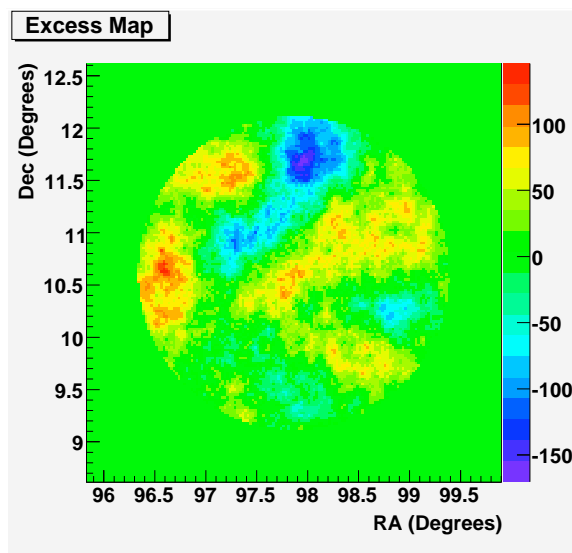


(a)

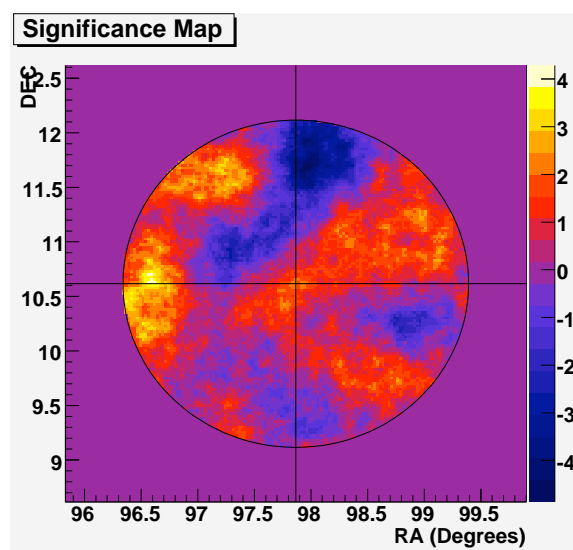


(b)

Fig. 5.18. Same as Figure 5.3, except for PSR J0631+1036. There is clearly an excess of negative significances on the left tail of the distribution in Figure 5.18(b). The sky maps in Figure 5.5.2 indicate a region of negative significance north of the putative source position. A bright star in this location is contributing to this negative excess.

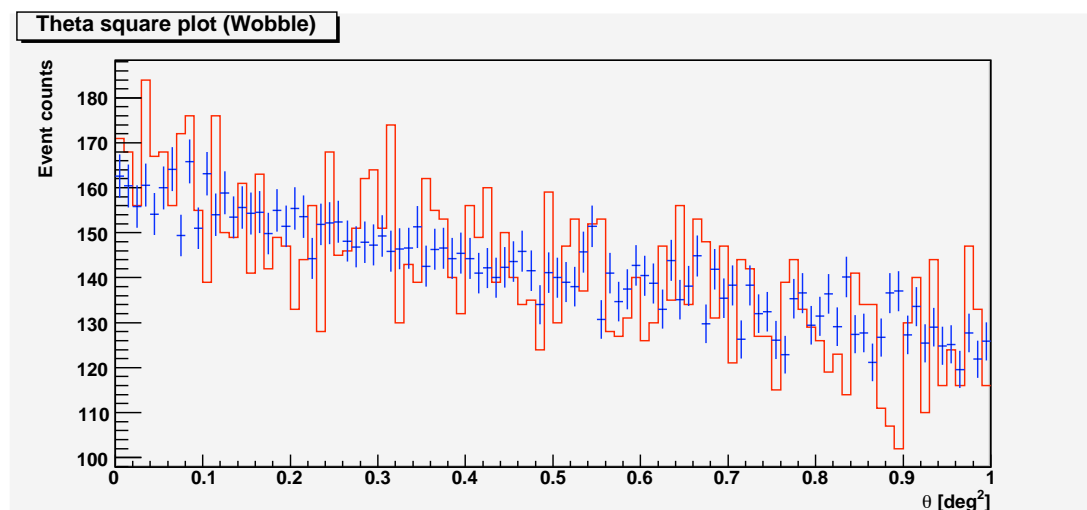


(a)

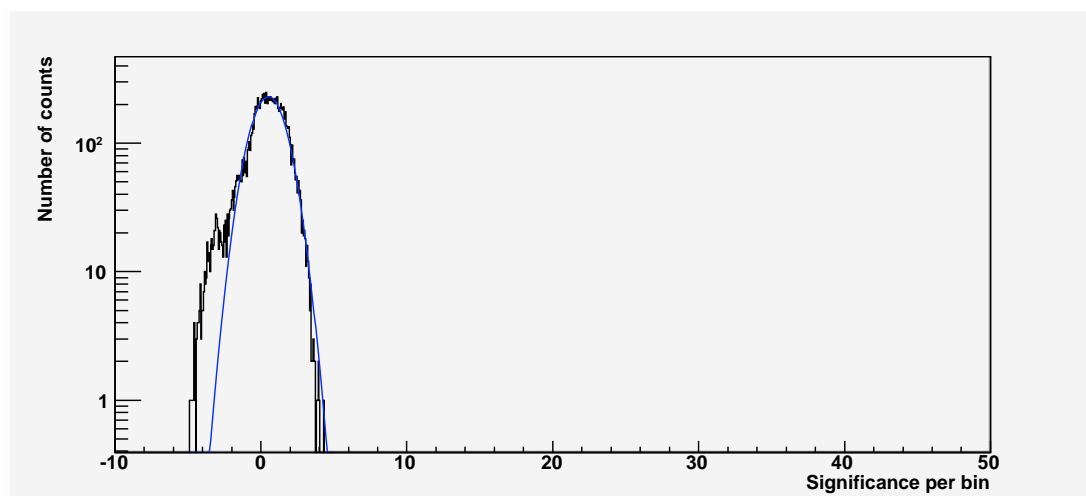


(b)

Fig. 5.19. Same as Figure 5.5.2, except for the extended source analysis.



(a)



(b)

Fig. 5.20. Same as Figure 5.5.2, except for the extended source analysis. The same negative excess is present in Figure 5.20(b), as in the point source analysis. Again, this is likely due to the presence of a bright star in the field of view.

5.6 PSR J1930+1852

In 2002 the Arecibo radio telescope discovered a 136 millisecond pulsar in the supernova remnant G54.1+0.3 with a dispersion measure of 308 pc cm^{-3} . Radio observations indicate a very low flux density of $60 \mu\text{Jy}$ in the 1180 MHz band. Considering a relatively close distance of 5 kpc, that makes PSR J1930+1852 the least luminous of the young Crab-like pulsars [70]. With a constant spin down rate of $7.5112 \times 10^{-13} \text{ s s}^{-1}$ a characteristic age of 2900 years is calculated. Observations of this young pulsar by both the ASCA and Chandra X-ray telescopes confirmed the X-ray pulsations reported in the radio band. The pulsed spectrum of the star is fit with a photon index of $\Gamma = 1.2 \pm 0.2$, which is a slightly harder spectrum than what is reported for the nebular emission. With a spin down power of $1.2 \times 10^{37} \text{ ergs s}^{-1}$, PSR J1930+1852 is the eight most energetic pulsar known [71].

Given the strength of the pulsar wind, PSR J1930+1852 is a prime candidate for creating high energy emission in the interstellar medium. However, unlike the Crab, the remnant is still resolved in the broadband emission profile of the region. The fact that the remnant has yet to dissipate may indicate that the surrounding region is a low density region, and the material has yet to be swept away [70, 71].

5.6.1 Data Taken on PSR J1930+1852

PSR J1930+1852 is one of the highest spin down power pulsars known in the northern sky. However, there has been little study of this source, and its associated nebula, in high energy gamma rays. As such, 10 hours of time was allotted to study the source, but it was given a lower priority than some other sources, like the Boomerang Nebula. The result was that less than 5 hours of quality, good weather data was collected on the source during the fall of 2007. Additionally, PSR J1930+1852 was observed under moderate moonlight. This fact may have a slight effect on the standard analysis of the data, in that "holes" can be created in the analysis where the current in the pixels was high due to the increased background light from the Moon,

leading to event deficits in the data reconstruction. Consequently, a plot of the significance distribution may contain a slight excess. This effect is not well understood at this time, though attempts to model it are being carried out. Additionally, the presence of the moonlight background will interfere with any effort to reconstruct the energy spectrum if a signal was identified, as the extra light will make the events appear to have a larger size. Listed in table 5.6 are the data that have been collected thus far.

Table 5.6: The log of the data acquired during the fall of 2007 on PSR J1930+1852. The layout of the table is the same as Table 5.2.

Run #	Date	Laser #	Duration (minutes)	Livetime (minutes)	Mode	Sky
36575	20070919	36601	20	18.81	0.5N	B
36576	20070919	36601	20	18.84	0.5S	B
36577	20070919	36601	20	11.33	0.5E	B
36578	20070919	36601	20	18.76	0.5W	B
36579	20070919	36601	20	18.95	0.5E	B
36614	20070920	36601	20	18.68	0.5S	B
36615	20070920	36601	20	18.81	0.5N	B
36617	20070920	36601	20	18.91	0.5W	B
37233	20071016	37263	20	18.80	0.5N	A
37234	20071016	37263	20	18.71	0.5S	A
37235	20071016	37263	20	18.95	0.5W	A
37271	20071017	37296	20	18.78	0.5E	A
37272	20071017	37296	20	18.81	0.5W	A

Continued on Next Page...

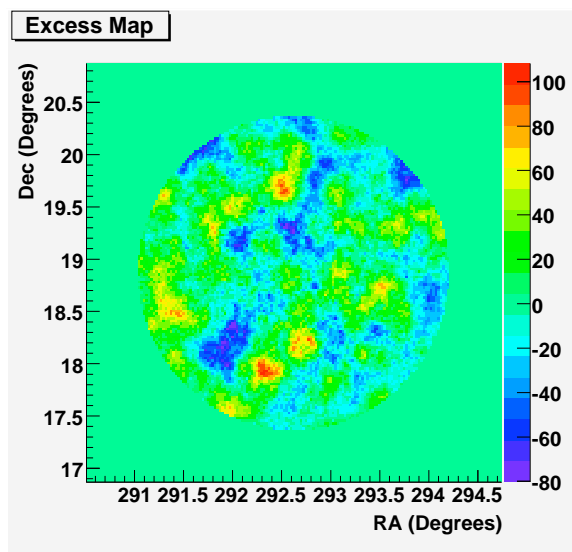
Table 5.6 –Continued

Run #	Date	Laser #	Duration (minutes)	Livetime (minutes)	Mode	Sky
37305	20071018	37371	20	18.89	0.5E	A
Total			280	256.0		

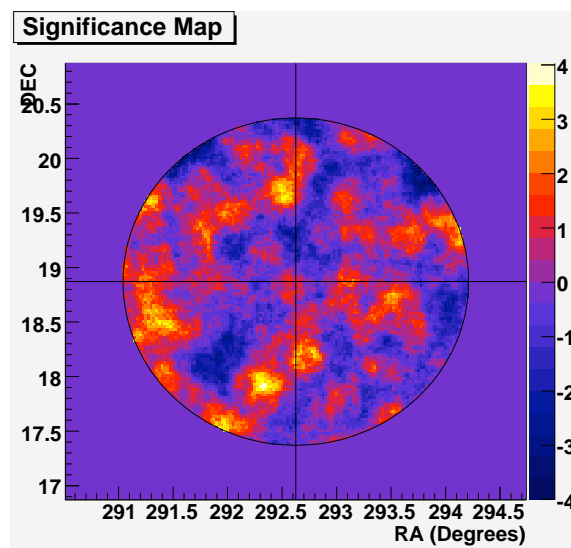
5.6.2 Point-Source Analysis of PSR J1930+1852

Since some of the brightest sources known in TeV gamma rays are PWNe, it is not unreasonable to search for a signal from a PWN source with only a few hours of data. Naturally, the more data that are collected, the more likely it is that a weak signal can be extracted. Analysis of the small data set taken thus far on the PWN associated with the pulsar PSR J1930+1852 and the remnant G54.1+0.3, does not yield a significant detection. The theta squared distribution performed for the standard point-source analysis, Figure 5.22(a), does not indicate an excess of events at the source position.

Similarly, reconstructing the two dimensional sky maps, shown in Figures 5.21(a) and 5.21(b), also do not give a hint of a possible detection. The lack of a detection in this case does not necessarily exclude this source as a possible gamma ray emitter. Given that only 4 hours of data were acquired, it is not possible to obtain a very deep exposure of the region. The significance and rate obtained for the putative source position is consistent with a null detection.



(a)

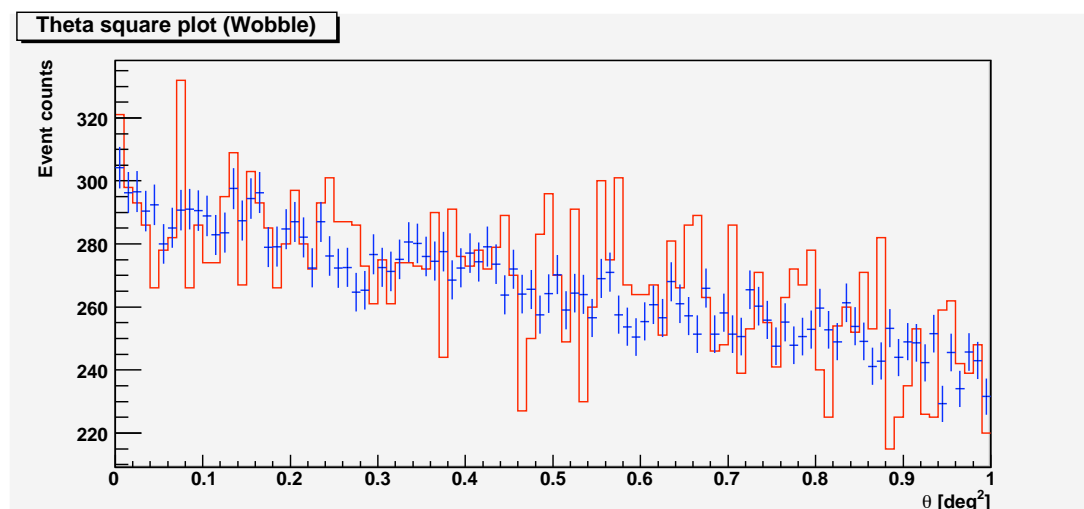


(b)

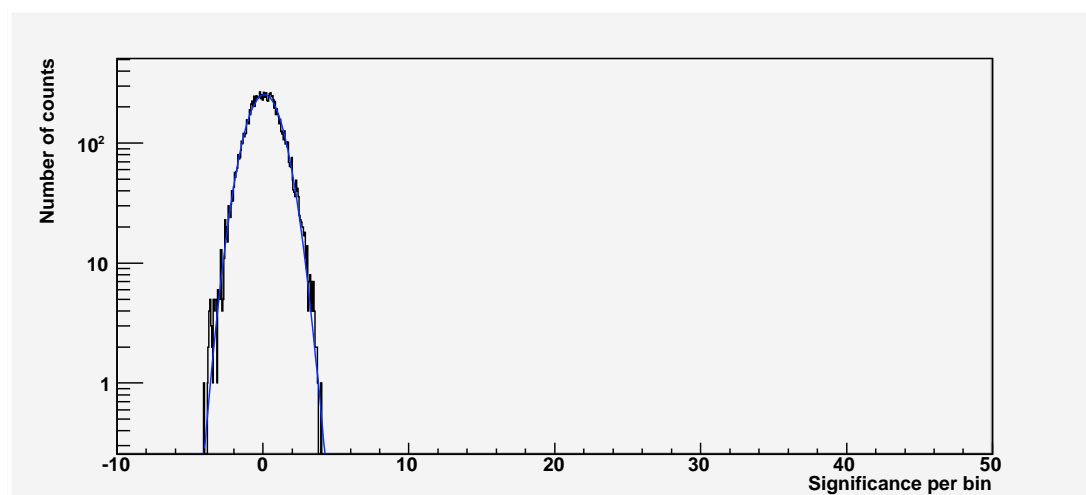
Fig. 5.21. Same as Figure 5.2, except for PSR J1930+1852.

5.6.3 Extended Source Analysis of PSR J1930+1852

As was shown with the Crab nebula, applying an extended source analysis can degrade the gamma-ray detection rate. Since there were only a small amount of data collected on this source, and no detection was evident in the point-source analysis, the



(a)

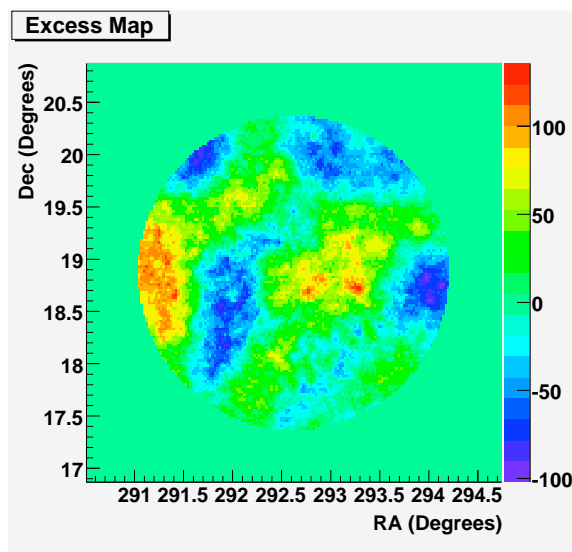


(b)

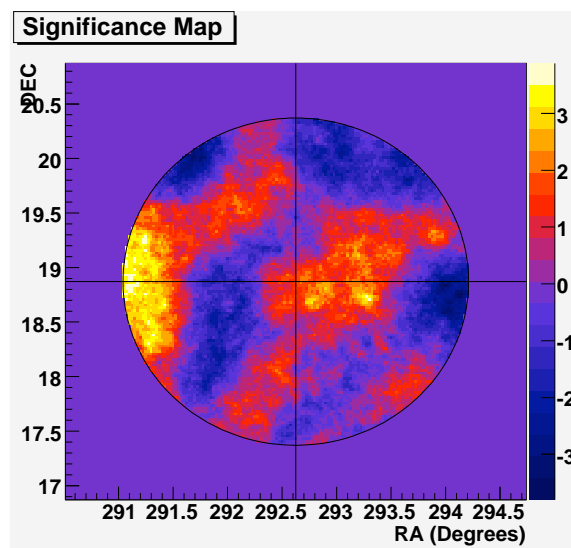
Fig. 5.22. Same as Figure 5.3, except for PSR J1930+1852.

extended source analysis is not likely to provide fruitful results. However, there is still information to be gained about the possible morphology of the region by doing such an analysis, even with limited data. The theta squared distribution for the source, Figure 5.24(a), still does no better in resolving an excess near the source position.

The excess and significance maps resulting from the extended source analysis, see Figures 5.23(a) and 5.23(b), appear differ greatly from the point-source analysis maps.



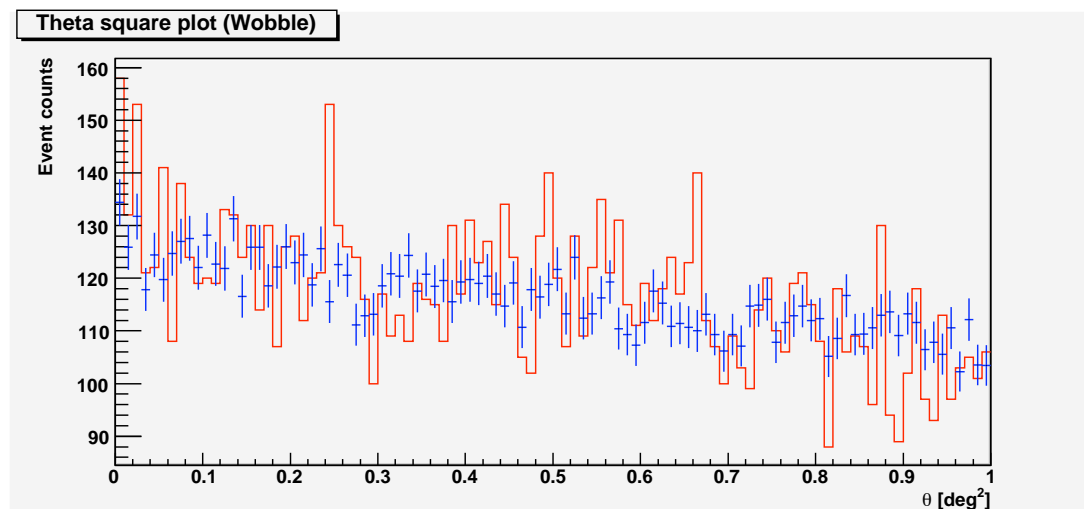
(a)



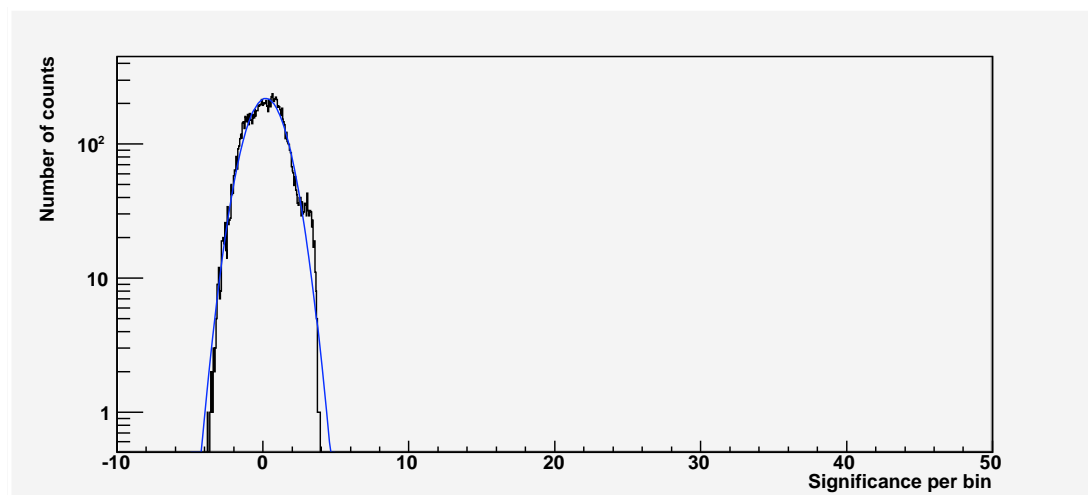
(b)

Fig. 5.23. Same as Figure 5.18, except the extended source analysis.

However examination of Figure 5.24(b) indicates that the significance distribution is well formed to a Gaussian. Again, given the low amount of data, coupled with the fact that none of the significance bins exceeds the 3σ threshold, it is likely that the features present in the maps are purely due to statistical fluctuations. With the current data



(a)



(b)

Fig. 5.24. Same as Figure 5.19, except the extended source analysis.

set, the significance and rate at the putative source position are consistent with a null detection.

5.6.4 Discussion of PSR J1930+1852 Results

In spite of only a small amount of data acquired on PSR J1930+1852 it is possible to place a limit of 3.7% of the Crab flux on the source emission. And given the high spin-down power of PSR J1930+1852, further study has been approved with more data slated to be acquired later in 2008.

6. CONCLUSION

In order to improve upon our current understanding of pulsar wind nebulae, deep observations of these objects must be made across the electromagnetic spectrum. Having a broad spectral range of data will allow for new and more complete theoretical models to be developed to explain the detected emission. Currently, the major northern hemisphere experiments have yet to claim significant detections of these objects, with the exception of the Crab nebula. The upper limits determined for these objects do, however, have important scientific consequences.

Firstly, these upper limits are the tightest values determined to date, surpassing the 2-3% Crab Flux upper limits found in recent surveys of the 3C 58 and Boomerang Nebula regions by other instruments. Even more compelling, is that these limits have consequences for the Bednarek and Bartosik model discussed in chapter 2. According to that model, the expected gamma ray spectrum from the 3C 58 Nebula should have a flux of about 2% of the Crab Nebula flux [47]. The implication from the 1.6% Crab Nebula flux reported here indicates that this model may be flawed, or that there is some aspect of the Nebula that is not well understood. The same thing is true for the Boomerang Nebula. The determined flux upper limit of 1.5% Crab Nebula flux is well below the 9-10% flux predicted by the Bednarek and Bartosik Model [47]. Given that there is a disparity between the predicted and measured fluxes for both of these objects it may be tempting to reconcile this as proof of a failure of the model, however this is not necessarily the case. H.E.S.S. recently reported detection of at least 8 PWNe, most of them falling in the 5-10% Crab Nebula flux regime [72]. So, it is difficult to get a handle on the lack of high energy emission from these sources, given the depth of these observations. Ultimately, more data is required to better understand these regions.

VERITAS was only recently deployed, and as with any new experiment, is still being tuned, refined and improved. As the array becomes more stable, and planned upgrades are put in place, it is possible that its sensitivity may improve considerably. Also, there is still much work being done in refining the analysis techniques. New methods for analyzing the data are being presented as we gain a better understanding of the data. Specifically, work is still being done to understand the extended source analysis techniques that will allow for resolution of extended emission regions, without sacrificing sensitivity. This, coupled with the development of methods to increase our sensitivity at lower energies, will allow for the extraction of weaker signals.

There is still much work to be done, and the results presented here, summarized in Table 6.1, are only the beginning. More data are needed, and more detailed analyses are required. But as the VERITAS instrument emerges from her infancy, these things will come, and a clearer understanding of PWNe and other sources will be realized.

Table 6.1
Summary of the point-source analysis results for the PWN data taken by the VERITAS array since September of 2007.

Object	Point Source Significance (σ)	Point Source Rate ($\gamma/\text{min.}$)	Integral Flux Upperlimit (% Crab Flux)
Crab	74.6	9.2 ± 0.2	N/A
Boomerang Nebula	-0.17	-0.01 ± 0.06	$\leq 1.5\%$
3C 58	-0.28	-0.02 ± 0.06	$\leq 1.6\%$
PSR J0631+1036	0.91	0.05 ± 0.06	$\leq 2.1\%$
PSR J1930+1852	0.57	0.06 ± 0.11	$\leq 3.7\%$

LIST OF REFERENCES

LIST OF REFERENCES

- [1] Galbraith, W. and Jelley, J. V., “Light pulses in the night sky associated with cosmic rays,” *Nature*, vol. 171, pp. 349–350, 1953.
- [2] Weekes, T. C., Cawley M. F. Fegan D. J. Gibbs K. G. Hillas A. M. Kowk P. W. Lamb R. C. Lewis D. A. Macomb D. Porter N. A. Reynolds P. T. and Vacanti G., “Observations of TeV Gamma rays from the Crab Nebula using the atmospheric Cherenkov imaging technique,” *The Astrophysical Journal*, vol. 342, 1989.
- [3] Akhperjanian, A., Kankanian R. Sahakian V. Heusler A. Wiedner C. A. and Wirth H., “The optical layout of the HEGRA Cherenkov telescopes,” *Experimental Astronomy*, vol. 8, pp. 135–152, 1998.
- [4] Mori, M. for the CANGAROO Team, “Recent results from CANGAROO,” in *Proceedings of the 28th ICRC*, vol. 5, pp. 2863–2866, 2003.
- [5] Aharonian, F. for the H.E.S.S. Collaboration, “H.E.S.S. – The High Energy Stereoscopic System,” in *Bulletin of the American Astronomical Society*, vol. 32, p. 1261, 2000.
- [6] Lemièrè, A. for the H.E.S.S. Collaboration, “New VHE emitting middle-aged pulsar wind nebula candidates in the extended H.E.S.S. Galactic plane survey data,” in *30th International Cosmic Ray Conference*, 2007.
- [7] Aharonian, F. and et. al., “Discovery of Very High Energy Gamma rays associated with an X-Ray Binary,” *Science*, vol. 309, no. 5735, pp. 746–749, 2005.
- [8] Acciari, V. A. et al., “VERITAS observations of the Gamma-ray Binary LS I +61 303,” *The Astrophysical Journal*, vol. 679, p. 1427, 2008.
- [9] Albert, J. et. al., “Variable Very-High-Energy Gamma-ray emission from the microquasar LS I +61 303,” *Science*, vol. 312, no. 5781, pp. 1771–1773, 2006.
- [10] Aharonian, F. et. al., “Very High Energy Gamma rays from the direction of Sagittarius A*,” *Astronomy and Astrophysics*, vol. 425, pp. L13–L17, 2004.
- [11] Kosack, K. et. al., “TeV Gamma-ray observations of the Galactic Center,” *The Astrophysical Journal Letters*, vol. 608, no. 2, pp. L97–L100, 2004.
- [12] van Eldik, C., Bolz O. Braun I. Hermann G. Hinton J. and Hofmann W., “Localising the H.E.S.S. Galactic Centre point source,” in *30th International Cosmic Ray Conference*, 2007.
- [13] Funk, S. for the H.E.S.S. Collaboration, “Status of identification of VHE Gamma - ray sources.” To Appear in *Astrophysics and Space Science*.

- [14] Finley, J. P. for the VERITAS Collaboration, “Observations of the unidentified Gamma-ray source TEV 2032+413 with the Whipple 10 meter telescope,” in *Bulletin of the American Astronomical Society*, vol. 35, p. 1216, 2003.
- [15] de Gouveia dal Pino, Elisabete M., “Astrophysical Jets and Outflows,” *Advances in Space Research*, vol. 35, no. 5, pp. 908–924, 2005.
- [16] Punch, M. et. al., “Detection of TeV photons from the active galaxy Markarian 421,” *Nature*, vol. 358, no. 6386, pp. 477,478, 1992.
- [17] Acciari, V. A. et al., “Observation of Gamma-ray emission from the galaxy M87 above 250 GeV with VERITAS,” *The Astrophysical Journal*, vol. 679, p. 397, 2008.
- [18] Piran, Tsvi, “The physics of Gamma-ray bursts,” *Reviews of Modern Physics*, vol. 76, no. 4, pp. 1143–1210, 2005.
- [19] Gedalin, M., Balikhin M. A. and Eichler D., “Efficient electron heating in relativistic shocks and Gamma-Ray-Burst afterglow,” *Physical Review E*, vol. 77, no. 2, 2008.
- [20] Longair, Malcolm S., *High Energy Astrophysics*, vol. 1. Cambridge University Press, 2 ed., 1994.
- [21] Rybicki, George B. and Lightman, Alan P., *Radiative Processes in Astrophysics*. John Wiley and Sons, 1979.
- [22] <http://www.atnf.csiro.au/>.
- [23] Zhang, C. M., Yin H. X. Y. Kojima Chang H. K. Xu R. X. Li X. D. Zhang B. and Kiziltan B., “Measuring neutron star mass and radius with three mass-radius relations,” *Monthly Notices of the Royal Astronomical Society*, vol. 374, no. 1, pp. 232–236, 2007.
- [24] Lattimer, J. M. and Prakash, M., “Neutron star structure and the equation of state,” *The Astrophysical Journal*, vol. 550, no. 1, pp. 426–442, 2001.
- [25] Gurevich, A. V. and Istomin, Ya. N., “The energy loss of a rotating magnetized neutron star,” *Monthly Notices of the Royal Astronomical Society*, vol. 377, no. 4, pp. 1663–1667, 2007.
- [26] Goldreich, Peter and Julian, William H., “Pulsar electrodynamics,” *The Astrophysical Journal*, vol. 157, pp. 869–880, August 1969.
- [27] Rudak, B. and Ritter, H., “The line of death, the line of birth,” *Monthly Notices of the Royal Astronomical Society*, vol. 267, pp. 513–517, 1994.
- [28] Ruderman, M. A. and Sutherland, P. G., “Theory of pulsars: Polar gaps, sparks, and coherent microwave radiation,” *The Astrophysical Journal*, vol. 196, pp. 51–72, 1975.
- [29] Kaspi, V. M., Roberts M. S. E. and Harding A. K., *Compact Stellar X-ray Sources*, ch. Isolated Neutron Stars. Cambridge Astrophysics Series, No. 39, Cambridge University Press, 2006.

- [30] Daugherty, J. K. and Harding, A. K., “Gamma ray pulsars: Emission from extended polar cap cascades,” *Astrophysical Journal*, vol. 458, p. 278, 1996.
- [31] Harding, Alice K. and Muslimov, Alexander G., “Particle acceleration zones above pulsar polar caps: Electron and positron pair formation fronts,” *The Astrophysical Journal*, vol. 508, pp. 328–346, November 1998.
- [32] Harding, Alice K., Usov Vladimir V. and Muslimov Alexander G., “High-Energy emission from millisecond pulsars,” *The Astrophysical Journal*, vol. 622, pp. 531–543, March 2005.
- [33] Muslimov, Alexander G. and Harding, Alice K., “Particle acceleration in pair-starved pulsars,” *The Astrophysical Journal*, vol. 617, pp. 471–479, December 2004.
- [34] Cheng, K. S., Ho C. and Ruderman M., “Energetic radiation from rapidly spinning pulsars. 1. Outer magnetosphere gaps,” *The Astrophysical Journal*, vol. 300, pp. 500–521, January 1986.
- [35] Chiang, James and Romani, Roger W., “An outer gap model of high-energy emission from rotation-powered pulsars,” *The Astrophysical Journal*, vol. 436, pp. 754–761, December 1994.
- [36] Cheng, K. S., Ho C. and Ruderman M., “Energetic radiation from rapidly spinning pulsars. ii. Vela and Crab,” *The Astrophysical Journal*, vol. 300, pp. 522–539, January 1986.
- [37] Zhang, L. and Cheng, K. S., “High-Energy radiation from rapidly spinning pulsars with thick outer gaps,” *The Astrophysical Journal*, vol. 487, p. 370, 1997.
- [38] Cheng, K. S., Ruderman M. A. and Zhang L., “A three-dimensional outer magnetospheric gap model for Gamma-ray pulsars: Geometry, pair production, emission morphologies, and phase-resolved spectra,” *The Astrophysical Journal*, vol. 537, no. 2, pp. 964–976, 2000.
- [39] Hirotani, K., Harding A. K. and Shibata S., “Electrodynamics of an outer gap accelerator: Formation of a soft power-law spectrum between 100 MeV and 3 GeV,” *The Astrophysical Journal*, vol. 591, p. 334, 2003.
- [40] Hirotani, K. and Shibata, S., “One-dimensional electric field structure of an outer gap accelerator - iii. Location of the gap and the Gamma-ray spectrum,” *Monthly Notices of the Royal Astronomical Society*, vol. 325, no. 3, pp. 1228–1240, 2001.
- [41] Gotthelf, E. V., “A spin-down power threshold for pulsar wind nebula generation?,” in *Young Neutron Stars and Their Environments*, IAU Symposium no. 218, 2003.
- [42] Kennel, C. F. and Corontini, F. V., “Confinement of the Crab pulsar’s wind by its supernova remnant,” *Astrophysical Journal*, vol. 283, pp. 694–709, 1984.
- [43] Credit: NASA, ESA, J. Hester and A. Loll (Arizona State University).
- [44] Chevalier, R. A., “A model for the X-Ray luminosity of pulsar nebulae,” *The Astrophysical Journal Letters*, vol. 539, no. 1, 2000.

- [45] Pravdo, S. H. and Serlemitsos, P., “X-Ray spectra of the Crab pulsar and Nebula,” *The Astrophysical Journal*, vol. 246, pp. 484–488, 1981.
- [46] Kennel, C. F. and Corontini, F. V., “Magnetohydrodynamic model of Crab Nebula radiation,” *The Astrophysical Journal*, vol. 283, pp. 710–730, 1984.
- [47] Bednarek, W. and Bartosik, M., “Gamma rays from the pulsar wind nebulae,” *Astronomy & Astrophysics*, vol. 405, pp. 689–702, 2003.
- [48] Stanev, T., *High Energy Cosmic Rays*. Praxis Publishing Ltd., 2nd ed. ed., 2004.
- [49] Nagai, T., McKay R. Sledge G. and Petry D. for the VERITAS Collaboration, “Focal Plane Instrumentation of VERITAS,” in *30th International Cosmic Ray Conference*, 2007.
- [50] Weinstein, A. for the VERITAS Collaboration, “The VERITAS trigger system,” in *30th International Cosmic Ray Conference*, 2007.
- [51] Holder, Jamie and the VERITAS collaboration, “The First VERITAS Telescope.” Submitted to Elsevier Science, February 2006.
- [52] Hays, E. for the VERITAS Collaboration, “VERITAS data acquisition,” in *30th International Cosmic Ray Conference*, 2007.
- [53] Hanna, David for the VERITAS Collaboration, “Calibration Techniques for VERITAS,” in *30th International Cosmic Ray Conference*, 2007.
- [54] Ritz, S., “High energy Gamma-ray astrophysics,” in *PIC2003*, 2003.
- [55] Daniel, M. K. for the VERITAS Collaboration, “The VERITAS standard data analysis,” in *30th International Cosmic Ray Conference*, 2007.
- [56] Cogan, P. for the VERITAS Collaboration, “VEGAS, the VERITAS Gamma-ray Analysis Suite,” in *30th International Cosmic Ray Conference*, 2007.
- [57] Helene, O., “Upper limit of peak area,” *Nuclear Instruments and Methods*, vol. 212, pp. 319–322, 1983.
- [58] Li, Ti-pei and Ma, Yu-qian, “Analysis methods for results in Gamma-ray astronomy,” *The Astrophysical Journal*, vol. 272, pp. 317–324, September 1983.
- [59] Barnard, G. A., “Studies in the history of probability and statistics: Ix. Thomas Bayes’ essay towards solving a problem in the doctrine of chances,” *Biometrika*, 1958.
- [60] <http://www.scitech.ac.uk/>.
- [61] Zhang, L., Chen S. B. and Fang J., “Nonthermal radiation from pulsar wind nebulae,” *The Astrophysical Journal*, vol. 676, no. 2, pp. 1210–1217, 2008.
- [62] Credit: NASA, ESA, CXC JPL-Caltech J. Hester and A. Loll (Arizona State University) R. Gehrz (University of Minn.) and STScI.
- [63] Halpern, J. P., Camilo F. Gotthelf E. V. Helfand D. J. Kramer M. Lyne A. G. Leighly K. M. and Eracleous M., “PSR J2229+6114: Discovery of an energetic young pulsar in the error box of the EGRET source 3EG J2227+6122,” *The Astrophysical Journal Letters*, vol. 552, pp. L125–L128, 2001.

- [64] Kothes, R., Reigh W. and Uyaniker B., “The Boomerang PWN G106.6+2.9 and the magnetic field structure in pulsar wind nebulae,” *The Astrophysical Journal*, vol. 638, pp. 225–233, 2006.
- [65] Credit: NASA, ESA and The Hubble Heritage Team (STScI/AURA), <http://hubblesite.org/newscenter/archive/releases/2005/25/image/a/>.
- [66] Roberts, D. A., Goss W. M. Kalberla P. M. W. Herbstmeier U. Schwarz U. J., “High resolution HI observations of 3C58,” *Astronomy & Astrophysics*, vol. 274, no. 2, p. 427, 1993.
- [67] Slane, P., Helfand D. J. Swaluw E. van der Murray S. S., “New constraints on the structure and evolution of the pulsar wind nebula 3C 58,” *The Astrophysical Journal*, vol. 616, pp. 403–413, 2004.
- [68] NASA/CXC/SAO/P.Slane.et.al.
- [69] Kennea, J., Cordova F. Chatterjee S. Cordes J. Ho C. Much R. Oosterbroek T. and Parmar A., “XMM-Newton sets the record straight: No X-Ray emission detected from PSR J0631+1036,” *Astrophysical Journal*, 2002.
- [70] Camilom, F., Lorimer D. R. Dhat N. D. R. Gotthelf E. V. Halpern J. P. Wang Q. D. Lu F. J. and Mirabal N., “Discovery of a 136 millisecond Radio and X-Ray pulsar in supernova remnant G54.1+0.3,” *The Astrophysical Journal Letters*, vol. 574, pp. L71–L74, 2002.
- [71] Lu, F., Wang Daniel Q. Gotthelf E. V. and Qu Jinlu, “X-Ray timing observations of PSR J1930+1852 in the Crab-like SNR G54.1+0.3,” *The Astrophysical Journal*, vol. 663, pp. 315–319, 2007.
- [72] Aharonian, F. et. al., “The H.E.S.S. survey of the inner galaxy in very high energy gamma rays,” *The Astrophysical Journal*, vol. 636, pp. 777–797, 2006.

VITA

VITA

John Millis was born in Augsburg, Germany on November 13th, 1980 to his adoptive parents, Flip and Karen Millis. In 1999 John graduated from Homestead High School in Fort Wayne, Indiana. He then spent the next nine years at Purdue University in West Lafayette, Indiana where he received his Bachelors degree in physics in 2003 and later his PhD in 2008.

John and his wife Melissa were married on May 29th, 2004. And upon the completion of his studies at Purdue, they relocated to central Indiana where John accepted a faculty appointment at Anderson University in Anderson, Indiana.